




5-2021

3D Printing of Hybrid Architectures via Core-Shell Material Extrusion Additive Manufacturing

Robert Cody Pack

University of Tennessee, Knoxville, rpack2@vols.utk.edu

Follow this and additional works at: https://trace.tennessee.edu/utk_graddiss

 Part of the [Manufacturing Commons](#), [Polymer and Organic Materials Commons](#), and the [Structural Materials Commons](#)

Recommended Citation

Pack, Robert Cody, "3D Printing of Hybrid Architectures via Core-Shell Material Extrusion Additive Manufacturing. " PhD diss., University of Tennessee, 2021.
https://trace.tennessee.edu/utk_graddiss/6712

This Dissertation is brought to you for free and open access by the Graduate School at TRACE: Tennessee Research and Creative Exchange. It has been accepted for inclusion in Doctoral Dissertations by an authorized administrator of TRACE: Tennessee Research and Creative Exchange. For more information, please contact trace@utk.edu.

To the Graduate Council:

I am submitting herewith a dissertation written by Robert Cody Pack entitled "3D Printing of Hybrid Architectures via Core-Shell Material Extrusion Additive Manufacturing." I have examined the final electronic copy of this dissertation for form and content and recommend that it be accepted in partial fulfillment of the requirements for the degree of Doctor of Philosophy, with a major in Materials Science and Engineering.

Brett G. Compton, Major Professor

We have read this dissertation and recommend its acceptance:

Claudia J. Rawn, Chad E Duty, Yanfei F. Gao

Accepted for the Council:

Dixie L. Thompson

Vice Provost and Dean of the Graduate School

(Original signatures are on file with official student records.)

3D Printing of Hybrid Architectures via Core-Shell Material Extrusion
Additive Manufacturing

A Dissertation Presented for the
Doctor of Philosophy
Degree
The University of Tennessee, Knoxville

Robert Cody Pack

May 2021

Copyright © 2021 by Robert Cody Pack

All rights reserved.

DEDICATION

I dedicate this dissertation to my wife, Lauren Pack, and my parents, Robert and Tami Pack, for the large amount of love and support they have given me throughout my life.

ACKNOWLEDGEMENTS

This dissertation research was supported by the Center for Materials Processing (CMP), a Tennessee Higher Education Commission (THEC) at the University of Tennessee-Knoxville, and by Honeywell Federal Manufacturing and Technologies through contract DE-NA0002839, administered by Dr. Eric Eastwood, Dr. Jamie Messman, and Mr. Steve Patterson.

I would like to thank and acknowledge the following:

My wife, Lauren Pack, who has been there for me, offering endless love, support, and motivation, through all the ups and downs. I am thankful for all the sacrifices she has made, standing by my side throughout my graduate studies and all of life's obstacles. I am looking forward to the next chapter and the wonderful life we continue to build together.

My parents, Robert and Tami Pack, for all the guidance, care, and opportunities they have provided me in my life. I would not be where I am today if they had not constantly pushed me to work hard, chase goals, and be the best person that I possibly can be. I will be forever thankful for all the sacrifices they made and continue to make for myself and my brothers, to provide us with abundant opportunities that allow us to chase our dreams. I would also like to thank my brothers, Carter and Carson, for providing great companionship and memories over the years. Additionally, I would like to thank the rest of my family, my grandparents, Juddy and Othella Cody, and Gene and Rita Pack, my aunts and uncles, Clint and Heather Cody, and Gary and Gena Terry, my cousins,

Caitlin and Ella Cody, and Grayson and Garrison Terry, and my in-laws, Terry and Lesa Copeland, and Lanford and Thelma Duncan for their love and support.

My friends and fellow lab mates that accompanied me throughout this journey who provided assistance in numerous areas, an avenue for collaboration on different projects and ideas, and an academic family that I could turn to. I would like to thank all members of Dr. Compton's group, especially Nadim Hmeidat, Stian Romberg, and Wille Kemp for their assistance and support.

Dr. Roy Wilcox for introducing me to the world of research and lab work in my undergraduate studies and encouraging me to attend graduate school.

Rick Lowden for providing me with my first opportunity to work in a professional research environment and introducing me to materials science, sparking my desire to continue work in materials research. I am thankful for your guidance, motivation, and support in the year leading up to and my initial years in graduate school. Without it, I would not have been able to continue my education and pursue graduate school.

My committee members, Dr. Claudia Rawn, Dr. Chad Duty, and Dr. Yanfei Gao for their valuable insight and suggestions. I would especially like to thank Dr. Claudia Rawn, for being my advisor throughout my Masters degree and encouraging me to continue on with my doctorate work.

Last but not least, I would like to thank my advisor, Dr. Brett Compton for his careful guidance, continuous support, and patience throughout the years of my doctoral work. I am grateful to have had a mentorship that provided a strong support system, numerous opportunities, and large degree of freedom which allowed me to become more

independent and greatly improve professionally. Without him, my doctoral journey would not have been possible, nor would I have developed into the researcher that I am.

Finally, my Lord and savior Jesus Christ, for all his blessings, love, and guidance, providing me with the life I have, surrounded by a great family and friends, allowing me to be the man I am today.

Also, to all those I have unintentionally left out that have helped me along the way, I thank you.

ABSTRACT

Biological materials often employ hybrid architectures, such as the core-shell motif present in porcupine quills and plant stems, to achieve unique properties and performance. Drawing inspiration from these natural materials, a new method to fabricate lightweight and stiff core-shell architected filaments is reported. Specifically, a core-shell printhead conducive to printing highly loaded fiber-filled inks, as well as a new low-density syntactic foam ink, are utilized to 3D-print core-shell architectures consisting of a syntactic epoxy foam core surrounded by a stiff carbon fiber-reinforced epoxy composite shell. Effective printing of test specimens and structures with controlled geometry, composition, and architecture is demonstrated with printed core-shell samples exhibiting up to a 25 percent increase in specific stiffness over constituent materials.

A detrimental increase in foam density was observed during initial core-shell printing due to failure of glass microballoons (GMBs) during extrusion. To solve this, the second part of the dissertation investigates the relationships between GMB loading, extrusion pressure, nozzle diameter, and flowrate on printed density. These parameters are investigated to gain understanding of the conditions leading to GMB failure, informing selection of process parameters to minimize it. A new syntactic foam ink is formulated with GMBs that exhibit a lower average diameter and higher crush strength, ultimately enabling printing without prominent GMB failure and the ability to achieve near theoretical printed density. The new foam samples are stronger and stiffer than conventional syntactic foams and current DIW-printed foams. Further implementation of the new foam in the C-S architecture enabled a 5 percent increase in specific stiffness over previous values.

In the last section, work is done to further expand the capability of C-S printing by demonstrating multimaterial 3D printing using the core-shell nozzle. This approach enables “on-the-fly” switching between materials during fabrication, without the need for two nozzles. Material transition behavior is analyzed, multimaterial components are successfully printed, and flexural testing is conducted. Overall, the new approach enables material switching with a continuous print path, providing greater design flexibility and compositional control, opening new routes to DIW print multimaterial architectures.

TABLE OF CONTENTS

1. Introduction.....	1
1.1 Motivation.....	2
1.2 Direct Ink Write (DIW) Additive Manufacturing of Polymer Composites.....	4
1.3 Direct Ink Write (DIW) Thermoset Feedstock Materials.....	5
1.4 Core-shell Fabrication and DIW Printing.....	6
1.5 Research Outline.....	8
2. Carbon Fiber and Syntactic Foam Hybrid Materials via Core-Shell Material Extrusion Additive Manufacturing.....	10
2.1 Abstract.....	11
2.2 Introduction.....	12
2.3 Experimental Methods.....	15
2.3.1 Epoxy-based Ink Formulation.....	15
2.3.2 Core-shell Nozzle.....	17
2.3.3 Ink Rheology.....	17
2.3.4 Direct Ink Write Printing.....	19
2.3.5 Printed Sample Characterization.....	19
2.4 Results and Discussion.....	21
2.4.1 Ink Formulation.....	21
2.4.2 Core-shell Printhead Development and Printing.....	22
2.4.3 Rheological Characterization.....	22
2.4.4 Initial Foam Mechanical Properties.....	25
2.4.5 Characterization of Printed Core-shell Structure.....	25

2.4.6 Flexural Testing of Core-shell Samples.....	30
2.4.7 Selection of Material Index and Comparison	36
2.4.8 Core Eccentricity Measurements and Model Analysis.....	38
2.5 Conclusion	41
3. 3D Printing of Glass Microballoon Syntactic Foams via Material Extrusion Additive Manufacturing.....	42
3.1 Abstract.....	43
3.2 Introduction.....	44
3.3 Materials and Methods.....	47
3.3.1 Epoxy-based Syntactic Foam Ink and Glass Microballoons	47
3.3.2 Parallel Plate Rheology.....	49
3.3.3 Direct Ink Write Platform, Extrusion Pressure Measurements, and Sample Printing.....	49
3.3.4 Characterization	52
3.4 Results and Discussion	53
3.4.1 Direct Ink Write and Syntactic Foam Processing- Constraints and Considerations.....	53
3.4.2 Parallel Plate Rheology.....	54
3.4.3 Foam Sample Printing.....	58
3.4.4 Extrusion Pressure Measurements	58
3.4.5 Density Characterization.....	65
3.4.6 S32HS Mechanical Performance	70
3.4.7 Application of S32HS-58 Foam to Core-shell Architecture.....	77

3.5 Conclusions.....	80
4. Multimaterial Hybrid Additive Manufacturing Enabled by Core-shell Nozzle	82
4.1 Abstract.....	83
4.2 Introduction.....	83
4.3 Materials and Methods.....	85
4.3.1 Silicone and Epoxy-based Inks	85
4.3.2 Core-shell Multimaterial Printing.....	86
4.3.3 Characterization	87
4.4 Results and Discussion.	87
4.4.1 Nozzle Characterization and Transition Length Prediction.....	87
4.4.2 Transition Length Measurements, Gradient Characterization, and Printing ...	90
4.4.3 Multimaterial Printing with Carbon Fiber and Syntactic Foam Inks.....	95
4.4.4 Mechanical Improvement and Design Analysis of Graded Transition.....	99
4.5 Conclusions.....	102
5. Future Work	104
6. Conclusion	107
References.....	110
Appendix.....	123
Eccentric Sandwich Composite Model.....	124
Ideal Flexural Modulus	124
Correction for Eccentricity	129
Pressure-driven Flow Model for Foam Inks	133
Vita.....	134

LIST OF TABLES

Table 2.1 Core and shell ink constituents	18
Table 2.2. Core flowrate, mechanical properties, density, and average normalized eccentricity for printed samples	33
Table 3.1. Glass microballoon properties	48
Table 3.2. Rheological properties of foam inks	57
Table 3.3. Mechanical properties of S32HS foams.....	71
Table 3.4. Flexural properties of core-shell samples with S32HS foam.....	78
Table 4.1. Experimentally measured values for characteristic transitional lengths	91
Table A3.1. Pressure-driven flow model predictions versus experimental SSP values ...	133

LIST OF FIGURES

Figure 2.1. North American porcupine quill cross-sections	13
Figure 2.2. Schematic cross-sectional view of the C-S nozzle	16
Figure 2.3. Optical image of C-S nozzle components	23
Figure 2.4. Initial core-shell prints with silicone	23
Figure 2.5. Rheological behavior of formulated inks	24
Figure 2.6. Syntactic foam printing	26
Figure 2.7. Printed C-S specimens.....	27
Figure 2.8. Core-shell cross-sections and core eccentricity.....	29
Figure 2.9. Printed versus prescribed core volume and relationship with flowrate.....	29
Figure 2.10. X-ray CT micrographs.....	31
Figure 2.11. Mechanical properties and analytical model predictions	32
Figure 2.12. Mixed sample micrographs	35
Figure 2.13. Optical and scanning electron microscopy of 1.2-mm-diameter core-shell samples.....	35
Figure 2.14. Material indices and core eccentricity	37
Figure 2.15. X-ray CT tomographs of CF samples.....	40
Figure 3.1. Scanning electron micrographs of GMBs	48
Figure 3.2. DIW hardware for foam printing and pressure measurements.....	51
Figure 3.3. Rheological behavior of formulated foam inks	55
Figure 3.4. Printed foam samples for density and pressure measurements	59
Figure 3.5. Example of characteristic extrusion pressure profiles.....	61
Figure 3.6. Varied GMB loading and flowrate pressure profiles	62

Figure 3.7. Average steady-state pressure measurements versus flowrate	64
Figure 3.8. Density versus flowrate plots	66
Figure 3.9. Density versus flowrate and density versus steady-state pressure plots.....	68
Figure 3.10. Printed S32HS foam samples for mechanical testing.....	71
Figure 3.11. Flexural stress-stain curve a) and fracture surfaces	72
Figure 3.12. S32HS foam compression testing.....	73
Figure 3.13. Compression modulus and strength of S32HS foam.....	75
Figure 3.14. Property space map of compression properties	76
Figure 3.15. Optical micrographs of C-S cross-sections printed with S32HS foam	78
Figure 3.16. $E^{1/3}/\rho$ versus measured core volume fraction	79
Figure 4.1. Nozzle tip dissection and nozzle volume	89
Figure 4.2. Silicone transition behavior	91
Figure 4.3. Experimentally measured transition lengths versus estimated lengths	92
Figure 4.4. Printed silicone T-joint (60x35x15 H mm).....	94
Figure 4.5. Cross-sectional analysis of transition behavior with CF and foam inks	96
Figure 4.6. Multimaterial CF/foam flexural samples.....	98
Figure 4.7. Schematics of multimaterial beams in bending.....	100
Figure 5.1. Carbon fiber and silicon carbide shelled C-S structures	106
Figure A1. Geometries and idealizations for analytical C-S model development.....	125
Figure A3.1. Pressure-driven flow model predictions and experimental SSP values.....	133

1. INTRODUCTION

1.1 Motivation

Additive manufacturing, widely known as three-dimensional (3D) printing, has grown since its conception three decades ago into a billion dollar industry where it is currently being used in manufacturing sectors such as aerospace, automotive, and biomedical [1]. AM technologies, wherein components are built up layer-by-layer in an “additive” fashion, have revolutionized all areas of manufacturing by affording the ability to significantly reduce many of the design constraints present in conventional “subtractive” manufacturing techniques and allowing fabrication of novel complex geometries that cannot be readily molded, machined, or extruded [2]. Continued expansion and the ever increasing interest in AM capabilities has titled it as a new paradigm for material manufacturing [3], leading experts to claim it will be the enabling technology for a third Industrial Revolution [4, 5].

Despite advancements, progress is still needed to drive 3D printing beyond its established role as a rapid prototyping technology and expand its application in manufacturing. Growth in application space will be assisted by: (1) the development of new high-performance composite feedstock materials and (2) the engineering of new printing methods and hardware to enable fabrication of hybrid materials, described as “a combination of materials or material and space in configurations and connectivities that offer enhanced performance”[6]. Development of these new hybrid materials and methods, such as co-deposition via core-shell printing detailed in this work, will support expansion of the range of printed materials, to include functional and structural high-performance hybrid materials. These new materials will not only help overcome current challenges and advance AM as a whole but can benefit various areas of life such as

improved health with patient specific implants or drug delivery, energy conservation through use of efficient lightweight components, and economy through cost savings when manufacturing complex geometries.

Of the existing AM technologies, polymer extrusion additive manufacturing remains undoubtedly the most common, making it the cornerstone of AM [5]. Polymer extrusion AM can be divided into two types based on feedstock material and processing conditions: (1) fused filament fabrication (FFF) of thermoplastics and (2) direct ink write (DIW) of thermosets. While both have showed promise in producing high mechanical and functional properties in components, DIW, an extrusion-based technology consisting of the direct deposition of viscoelastic feedstock materials at ambient temperatures, is more adept for efficiently printing multimaterial hybrid architectures.

Although numerous hybrid architectures exist, by drawing inspiration and motivation from nature, the core-shell architecture, which is not only functionally advantageous but also enables realization of composites with high stiffness-to-weight ratios, was chosen as the hybrid architecture of emphasis. Thus, the aim of this work is to leverage the capabilities of direct write (DIW), to investigate printing of the core-shell (C-S) architecture and multimaterial hybrid architectures for lightweight applications.

In this work, fundamental knowledge pertaining to hybrid core-shell printing of highly loaded, reinforced epoxy inks is gained by investigation into feedstock formulation, print behavior, processing effects, and mechanical properties. This knowledge will help guide future development of C-S materials and printing methods, that can ultimately help expand the use of direct ink write through production of high-performance, multimaterial, hybrid components.

1.2 Direct Ink Write (DIW) Additive Manufacturing of Polymer Composites

Two main forms of extrusion-based polymer AM exist- fused filament fabrication (FFF) and direct ink write- that are differentiated by the type of feedstock material and processing conditions used. FFF consists of liquefying a thermoplastic at elevated temperatures, allowing extrusion through a print nozzle which then solidifies after deposition by cooling. Upscaling of FFF technology has led to systems such as big area additive manufacturing (BAAM), that have demonstrated the capability to print large scale, high-performance components for a variety of applications [7, 8]. However, application obstacles such as thermally induced distortion and insufficient inter-layer adhesion [9], makes DIW more conducive to printing of hybrid architectures.

Direct ink write (DIW) polymer AM utilizes the direct material deposition of viscoelastic thermoset feedstocks at ambient temperatures, that are latently cured after printing. High feedstock versatility allows fabrication of a broad range of materials such as polymers [10-12], ceramics [13-15], metals [16-18], and composites. Critical to the DIW process, ink formulations must exhibit certain favorable rheological properties such as shear thinning and viscoelastic behavior. Shear thinning permits ink extrusion through fine diameter nozzles under ambient conditions without requiring prohibitively high pressures. During deposition, inks must behave viscously to allow flow but once deposited, must behave elastically, possessing a high shear storage modulus, G' , and shear yield strength, τ_y , for shape retention [19].

1.3 Direct Ink Write (DIW) Thermoset Feedstock Materials

Feedstocks have been specifically created for DIW by addition of rheological modifiers (nano-clay platelets), viscosifying agents, and reinforcement fillers such as silicon carbide whiskers [20, 21], graphene [11], and short carbon fibers [19, 22, 23] into a thermoset epoxy matrix. Recent efforts to improve mechanical properties of printed materials have focused on the addition of fiber reinforcements, notably carbon fibers (CFs), that provide increased strength and stiffness but in turn, introduces challenges in printing such as increased viscosity and fiber clogging [8]. DIW CF reinforced composites have shown significant progress, exhibited by recent work in fabrication of lightweight cellular structures with high stiffness [19, 22], making it a fitting option for use as the main structural shell material in this work.

For low-density applications, syntactic foams, consisting of hollow spheres dispersed in a binder phase, are utilized for their high specific and compressive strength. The hollow spheres, which are used to introduce void area, can vary in size from nanometer to millimeter and are commonly referred to as microballoons (MBs) when sub-millimeter in size. Although several types of MBs have been used, such as carbon MBs [24] and cenospheres (ceramic) [25], glass MBs (GMBs) in an epoxy matrix remains the predominant combination in research and applications [26]. Syntactic foams have been applied mainly in marine sectors for buoyancy and compressive strength, yet continued research has expanded application to core materials in sandwich structures and aerospace applications [27]. Although formulation is necessary to provide the needed rheological properties, utilization of a syntactic foam provides a route to introduce

engineered porosity during printing, especially during co-deposition with a CF reinforced composite, making it an ideal candidate for use as the core material in DIW printing.

1.4 Core-shell Fabrication and DIW Printing

Fabrication of the core-shell architecture has been studied in extrusion processes such as electrospinning and polymer extrusion additive manufacturing to provide both functional and structural benefit. On the nano scale, electrospinning provides a route to fabricate composite and hollow core-shell fibers with diameters in the nanometer range through utilization of coaxial nozzles. During spinning, C-S nanofibers are collected on a plate to produce a non-woven mat or spooled to create a continuous fiber. Nanofiber mats are of interest to applications such as filters (oil filters, molecular filters) and protective clothing while nanofibers themselves show potential in applications such as microelectronics (batteries, energy capture), optics, and biomedical components (drug delivery) [28-30]. While utilization of the C-S architecture in electrospun fibers has afforded improvement in nanomaterials, application of the C-S architecture on micro- and milli-meter size scales will also enable new advancements.

Implementation of the core-shell architecture via material extrusion additive manufacturing processes has been investigated in previous research through various approaches with different material systems. Core-shell bioprinting or 3D plotting, consisting of printed C-S filaments with diameters of a few hundred microns, has gained interest recently by enabling fabrication of novel tissue scaffolds and drug delivery vessels. These processes utilize low viscosity feedstocks, mainly hydrogels, extruded out of concentric nozzles or microfluidic devices, to enable construction of components such

as hollow filament scaffolds that enable nutrient delivery through the core and C-S microfibers that can be loaded with drugs or other bioactive molecules to give tunable release profiles [31-33]. Even though these C-S components are advantageous to bio applications, low mechanical properties from biocompatible hydrogels limit application where structural integrity is needed. Providing the ability to print filaments ranging in diameter from a few hundred microns up to a few millimeters with filler reinforced inks, core-shell printing via DIW has been studied and shown successful in producing a variety of C-S architectures that afford improvement both functionally and structurally. Ceramics with a hollow core were fabricated by extruding a cast feedrod composed of a camphene core-camphene/alumina shell and then post treating with a drying, heating, and sintering process to remove the camphene and densify the alumina framework [34]. Carbon core and alumina shell filaments were printed in a truss structure utilizing a piston co-extrusion unit to coextrude alumina and carbon aqueous colloidal gels [35]. Aiming to produce lightweight ceramic architectures with high specific stiffness, hollow C-S struts in a lattice structure were printed using a coaxial printhead where an aqueous particle-stabilized foam ink was coextruded with a fugitive wax core [36]. Extending into functional applications, a fugitive viscoelastic hydrogel shell was utilized to encapsulate and support a liquid photocurable core to allow printing of optical waveguides with a custom coaxial printhead [37]. Finally, polymer multicore-shell filaments have been fabricated with a flexible epoxy core, elastomeric silicone interface, and brittle epoxy shell resulting in both high stiffness and toughness properties [38]. Despite advancements, there exist no examples to date of utilizing DIW to print fiber-reinforced C-S structures, leaving vast potential that has yet to be fully realized. This work aims to

mimic the high-performance capability of core-shell architectures exemplified in natural materials such as, plant stems, animal quills, and bird feathers [39] through utilization of C-S DIW printing. Similar to sandwich panels, C-S composites are mechanically efficient hybrid structures that combine two materials in a specified geometry, configured such that a dense stiff material surrounds a lightweight foam core, to produce properties of high bending stiffness and resistance to buckling at a low weight [40]. This work reports efforts to further advance core-shell printing by developing a process to print C-S architected filaments, along with a new low-density syntactic foam feedstock that provides further improvement to C-S architectures and also enables printing of high-performance foams, and finally, a new method to utilize a C-S nozzle to fabricate multimaterial components.

1.5 Research Outline

With the overarching goal of advancing DIW application space by fabricating and characterizing a syntactic foam core - CF reinforced shell architected composite and multimaterial composite via DIW, this work focuses on the following objectives:

- (i) ***Development of core-shell hardware and printing process:*** In order to study core-shell printed structures, it was necessary to engineer printing hardware, mainly a new custom, co-axial, co-deposition core-shell nozzle, and develop printing procedures. Epoxy based carbon fiber reinforced and glass micro-balloon foam feedstocks are formulated, and their rheological properties characterized. Flexural tests are used to investigate specific stiffness and strength properties and an analytical model is developed to predict the

mechanical improvement afforded by the C-S architecture provides. This work on the development of core-shell printing is discussed in Chapter 2.

(ii) *Optimization of foam core processing:* Syntactic foams are plagued by microballoon fracture, as seen during core-shell printing in Chapter 2, increasing the foam core density and decreasing the lightweight performance of the printed C-S samples. To achieve an optimal printed foam and fully leverage C-S application, investigation into relationships between flowrate, pressure in the nozzle, GMB loading, GMB type, and printed properties is discussed, along with development of high-performance monolithic foam components. Application of an improved foam in printed C-S components is also briefly examined. This work on investigation of syntactic foam processing is discussed in Chapter 3.

(iii) *Investigation of multimaterial printing utilizing the core-shell nozzle:* The final objective builds upon the previous two by developing a C-S printing route to enable fabrication of multimaterial components. The C-S nozzle provides the unique ability to transition between different compositions while maintaining a continuous filament, resulting in graded transition regions that are more robust compared to printing with two separate nozzles. This transition behavior, dependent upon material and nozzle type, and the measured flexural properties are investigated. This work on multimaterial printing utilizing the core-shell nozzle is discussed in Chapter 4.

**2. CARBON FIBER AND SYNTACTIC FOAM HYBRID
MATERIALS VIA CORE-SHELL MATERIAL EXTRUSION
ADDITIVE MANUFACTURING**

This chapter was adapted from a published version [41] by Robert C. Pack, Stian K. Romberg, Aly A. Badran, Nadim S. Hmeidat, Trenton Yount, and Brett G. Compton: R. C. Pack, S. K. Romberg, A.A. Badran, N. S. Hmeidat, T. Yount, and B.G. Compton. “Carbon Fiber and Syntactic Foam Hybrid Materials via Core-Shell Material Extrusion Additive Manufacturing.” *Advanced Materials Technologies*, (2020).

Changes to the text include addition of the supplemental figures and tables to the main body text, relabeling of all figures and tables accordingly, and reorganization into distinct sections. R.C. Pack performed the ink formulation, core-shell printing, sample characterization, mechanical testing, and writing of the article. S.K. Romberg derived the analytical model and assisted with writing, A.A. Badran performed the X-ray computed tomography characterization, N.S. Hmeidat assisted with rheological measurements, T. Yount assisted in ink formulation, and B.G. Compton assisted with data analyzation and oversaw article writing.

2.1 Abstract

Biological materials often employ hybrid architectures, such as the core-shell motif present in porcupine quills and plant stems, to achieve unique specific properties and performance. Drawing inspiration from these natural materials, a new method to fabricate lightweight and stiff core-shell architected filaments is reported. Specifically, a core-shell printhead conducive to printing highly loaded fiber-filled inks, as well as a new low-density syntactic foam ink, are utilized to 3D-print core-shell architectures consisting

of a syntactic epoxy foam core surrounded by a stiff carbon fiber-reinforced epoxy composite shell. Effective printing of test specimens and structures with controlled geometry, composition, and architecture is demonstrated. The new foam ink exhibits density as low as 0.68 g cm^{-3} and core-shell structures exhibit up to 25% higher specific flexural stiffness ($E^{1/3}/\rho$) than either constituent alone. Finally, a new mechanical model is presented to predict this performance improvement while accounting for potential eccentricity of the core.

2.2 Introduction

Many biological materials utilize hybrid structures, in which constituents with dissimilar mechanical or functional properties are cleverly arranged to produce improved specific properties, unique combinations of strength, stiffness, and toughness, and overall performance unattainable from a single material [42]. The core-shell (C-S) architecture is an excellent example of this approach manifest in nature by plant stems [42, 43], hedgehog spines [39, 44], and porcupine quills [45, 46], (**Figure 2.1**) which employ a low-density foam core surrounded by a dense, stiff outer shell. This approach results in a larger diameter structure when compared to an equivalent mass structure made of shell material alone [44], thereby enabling significantly higher bending stiffness and buckling resistance in the natural hybrid architecture, and enabling optimal structural and functional performance to the organism at minimal metabolic cost.

Additive manufacturing, which offers novel capabilities absent in traditional manufacturing [3], enables fabrication of bioinspired architectures such as the C-S motif described above. In particular, direct ink writing (DIW), a type of material extrusion



Figure 2. 1. North American porcupine quill cross-sections. Scale bar = 500 μ m

additive manufacturing, allows precise patterning of viscoelastic feedstock materials at ambient temperatures to build structural and/or functional components in a layer-by-layer fashion [47]. A wide variety of feedstock inks have been formulated for DIW, allowing fabrication of a broad range of materials including polymers [10-12, 48], ceramics [13-15], metals [16-18], and composites. For example, epoxy-based composite feedstocks reinforced with silicon carbide whiskers [20, 21, 49], nanoclay [10], graphene [11], and carbon fibers [12, 19, 23, 50] have been explored recently to improve strength and stiffness in printed materials. Further mechanical improvement can be realized by applying the C-S architecture to high stiffness carbon fiber (CF) inks coupled with low-density foam inks for the shell and core materials, respectively.

Implementation of the core-shell architecture via DIW has been investigated for both functional and structural applications with polymers and other material systems. For example, Moon et al. fabricated hollow-core ceramics by extruding a fugitive camphene core surrounded by a camphene/alumina shell, followed by sintering to densify the alumina framework [34]. Fu et al. printed carbon core-alumina shell filaments in a truss structure utilizing a piston-driven co-extrusion unit with alumina- and carbon-filled aqueous colloidal gels [35]. For lightweight hierarchical ceramic architectures, Muth et al. printed hollow C-S struts using an aqueous particle-stabilized foam ink coextruded with a fugitive wax core [36]. Extending into functional applications, Lorang et al. utilized a fugitive viscoelastic hydrogel shell to encapsulate and support a liquid photocurable core to print optical waveguides [37]. Recently, Mueller et al. utilized a 3D-printed core-shell printhead to create multicore-shell filaments with a flexible epoxy core, elastomeric silicone interface, and brittle epoxy shell. Lattice materials printed in this

motif showed considerable increase in energy absorption during crushing with minimal reduction in elastic stiffness [51]. This approach, when combined with high-performance carbon fiber-reinforced inks and low-density syntactic foam inks, could enable an entirely new class of ultra-low-density hybrid cellular materials with superior specific stiffness and buckling resistance combined with the potential to dramatically improve toughness [51] and damping [52] over traditional cellular materials.

Here, we report for the first time a new core-shell printhead (**Figure 2.2**) specifically designed to print highly loaded, fiber-filled inks, as well as a new low-density syntactic epoxy foam ink for use as a low-density core material in hybrid core-shell architectures. Composite-foam C-S architectures exhibit up to 25% higher specific flexural stiffness ($E^{1/3}/\rho$) than either of the constituents alone, while the printable foam is ~40% less dense than existing printed polymers with comparable mechanical properties.

2.3 Experimental Methods

2.3.1 Epoxy-based Ink Formulation

Inks were prepared by mixing Epon 826 epoxy resin (Momentive Specialty Chemicals, Inc. Columbus, OH) with 5 parts per hundred (pph) by weight resin 1-Ethyl-3-methylimidazolium dicyanamide (BASF Basionics VS03, Sigma-Aldrich, Inc., St. Louis, MO), dimethyl methylphosphonate (DMMP, Sigma Aldrich, St. Louis, MO), nanoclay (Garamite 7305, BYK-Chemie GmbH, Wesel, Germany), and chopped, unsized carbon fibers (Dialead K223HE, Mitsubishi Plastics Inc, Tokyo, Japan) or glass microballoons (S32, 3M Materials, St. Paul, MN) using a planetary mixer (FlackTek,

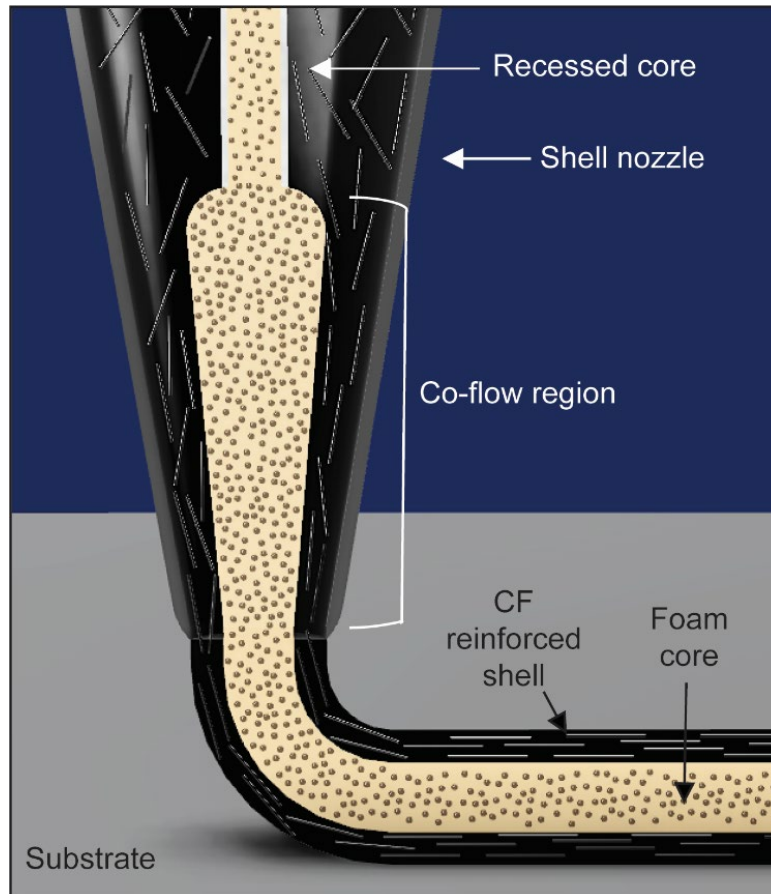


Figure 2.2. Schematic cross-sectional view of the C-S nozzle. The nozzle enables co-extrusion of a syntactic foam core and CF-reinforced shell.

Inc., Landrum, SC). Ink constituents are shown in **Table 2.1**. For both inks, Epon 826, DMMP, and VS03 were added together and mixed for 1.5 minutes at 1500 rpm. All mixing stages were conducted under vacuum at 0.1 atm. Garamite was then added and mixed for 2 min at 1700 rpm. Next, carbon fibers or GMBs were added in $\frac{1}{2}$, $\frac{1}{4}$, $\frac{1}{4}$, increments and mixed for 2 min at 1800 rpm between each addition. Finally, inks were remixed for 1.5 min at 1800 rpm prior to loading the syringe barrel.

2.3.2 Core-shell Nozzle

The core-shell nozzle was fabricated from parts obtained from McMaster-Carr, Inc. The upper core hub was fabricated from a male-female hex thread adapter milled out to encase luer lock quick turn sockets that hold the straight core tip (2.54-cm length, 660- μm ID). The shell injection hub consists of stainless-steel tubing (1.8-mm ID) inserted into a modified tube plug and secured with adhesive. Luer lock couplings were attached to the core and shell hubs for connection to pumps.

2.3.3 Ink Rheology

The rheological properties of each ink were characterized at $\sim 22^\circ\text{C}$ using a Discovery HR-2 Rheometer (TA Instruments, New Castle, DE) with 25-mm parallel plate geometry for both core and shell inks, and 40-mm parallel platens for the epoxy resin. A gap of 500 μm and 1 mm was used for the epoxy resin and core/shell inks, respectively. The apparent viscosity was characterized using continuous flow sweeps under controlled shear rate, and viscoelastic properties were measured using oscillatory amplitude sweeps at 1 Hz under stress control. Measurements were preceded by a 120-

Table 2.1 Core and shell ink constituents

Ink constituent	Carbon fiber ink (g)	Carbon fiber ink (vol %)	Glass micro-balloon ink (g)	Glass micro-balloon ink (vol. %)
Epoxy resin (Epon 826)	33	69.4	30	35.3
Nanoclay	2.2	3.4	2	1.7
DMMP	2.3	4.9	3	3.6
Curing agent	1.7	3.9	1.5	1.9
Carbon fibers	16.7	18.5	0	0
Glass microballoons	0	0	13.5	57.5

second conditioning step at 0.01 s^{-1} , followed by zero-stress equilibration for 120 seconds.

2.3.4 Direct Ink Write Printing

Inks were loaded into 10 mL syringe barrels (Nordson EFD, Westlake, OH) and centrifuged at 3600 rpm for 3.5 minutes using a Sorvall™ ST-8 Centrifuge (ThermoFisher Scientific, Waltham, MA) to degas. Syringe barrels were then loaded into high-pressure adapters (HP3, Nordson EFD, Westlake, OH), where ink is extruded pneumatically, that were mounted on the z-axis of the printer (Shoptbot Tools Inc., Durham, NC). For core-shell printing, pressure adapters were used to feed ink into volumetric dispensing pumps (Eco-pen, ViscoTec America Inc., Kennesaw, GA) connected to the C-S nozzle via luer lock couplings. Single-layer flexural samples (35 mm L x 12.75mm W x filament diameter H) and rectangular compression samples (13.5 mm x 13.5 mm x 10-25mm) were printed on PTFE-coated aluminum substrates (Bytac, Saint-Gobain Performance Plastics, Worcester, MA), directed by G-code generated from scripts written in Scilab software (Scilab Enterprises, France). Tapered tips of 1.6-mm- and 1.2-mm-diameter are used for printing. To determine flowrate, the volume of ink extruded per unit of time was calculated using the tip inner diameter and print speed, and then the prescribed flowrate was set to match in a 1:1 ratio. Printed samples were cured at 100°C for 24 hours followed by 2 hours at 220°C.

2.3.5 Printed Sample Characterization

Density measurements on cured samples utilized Archimedes method and sample dimensions were measured with digital calipers. Optical micrographs were taken using a

VHX-5000 digital microscope (Keyence Corporation of America, Itasca, IL) and scanning electron micrographs were taken using a Phenom Desktop SEM (Nanoscience Instruments, Inc, Phoenix, AZ). Core volumes were determined using the rule of mixtures and the measured density of printed monolithic samples. Measurements were verified by area analysis on optical micrographs. Eccentricity measurements were conducted on micrographs utilizing ImageJ software [53]. Three-point flexural tests were conducted at ambient temperature on as-printed samples with an electromechanical load frame (Model 45, MTS Systems Corporation, Eden Prairie, MN, USA) using a 1 KN load cell, span of 25 mm, and a crosshead speed of 0.01 mm s^{-1} . Compression testing was performed on the MTS utilizing spherically seated platens, a 100 KN load cell, and a crosshead speed of 0.01 mm s^{-1} . Reported average properties consist of 5 samples.

The 3D X-ray microscopy was conducted using a Zeiss Xradia 520 Versa CT microscope (Zeiss, Pleasanton, CA USA) at the University of Colorado, Boulder Materials Instrumentation and Multimodal Imaging Core Facility. Samples were scanned with no source filter at 50keV voltage, 4W power, 2.5-s exposure time for each 1600 projection on a 4x objective lens (total scan time=2.5 h), and a pixel binning mode of 2. Reconstruction utilized a Filtered Back Projection algorithm to generate 995 cross-sectional images, with a resolution of $1.6 \mu\text{m}$ per voxel. Image processing and visualization was conducted using Dragonfly software (Object Research Systems, Montreal, Canada).

2.4 Results and Discussion

2.4.1 Ink Formulation

Epoxy-based inks were formulated following previous approaches for fiber reinforced inks [12, 19]. An epoxy resin (Epon 826), latent curing agent, diluent, nanoclay, and carbon fibers (CFs) (18% by volume, 6 mm initial length) were utilized. While nanoclay has been shown to increase the strength and stiffness of printed epoxy composites [10, 49], it primarily serves as the rheological modifier, imparting the shear thinning and yield stress behavior required for DIW printing. Additionally, a diluent reduces initial viscosity in the epoxy resin allowing higher solids loading and a latent curing agent provides an extended printing window [19]. To provide compatibility during co-deposition and eliminate curing complications between dissimilar materials, identical matrix constituents were used to develop a new printable syntactic foam ink filled with glass microballoons (GMBs) (S32, 58% by volume, 20-80 μm diameter). Aiming to achieve the stiffest shell and lowest density core possible utilizing the chosen ink constituents, both shell and core inks were formulated (**Table 2.1**) to attain the highest practical volume loading of CF or GMB while still resulting in consistent extrusion and printing. 18 vol.% CF loading in epoxy is comparable to, or higher than most examples of 3D-printed epoxy composites in the literature [12, 19, 49, 50, 54, 55], with the notable exception of Nawafleh and Celik [56], who achieved up to 46 vol% CF in printed epoxy composites by utilizing a novel vibration-assisted print head.

2.4.2 Core-shell Printhead Development and Printing

Various C-S nozzle designs have been described in existing literature, yet most possess specific disadvantages for fiber-filled inks, including: i.) complex flow paths prone to clogging when fibers are present, ii.) integral construction preventing facile disassembly and cleanout in the event of clogging, and iii.) a fixed outlet diameter reducing the design flexibility and printhead versatility. Addressing these challenges, our printhead utilizes a modular C-S design consisting of an upper core housing attached to a shell injection hub (**Figure 2.3**) with straight core and tapered shell nozzles attached to the hubs via Leur lock fittings. Key design features include a recessed Luer lock core nozzle, creating a co-flow region that enables continuous variation of core-to-shell ratio, as demonstrated by Mueller et al. [51], and a replaceable Leur lock shell nozzle that enables printing of different filament diameters without the need for major hardware change (**Figure 2.4a**). Initial test prints with silicone display the ability to easily prescribe both core fraction and filament diameter (**Figure 2.4a**), as well as fabricate sparse lattice structures that can benefit from the C-S architecture (**Figure 2.4b**).

2.4.3 Rheological Characterization

Rheological behavior (**Figure 2.5**) reveals both inks display prominent shear thinning and similar viscosities of $\sim 10^3$ Pa·s at a 1 s^{-1} shear rate.

This behavior is advantageous, because similar viscosities decrease the likelihood of core movement during co-flow and increase probability of the core remaining centered and encapsulated [57-59]. Core and shell inks exhibit a high plateau storage modulus

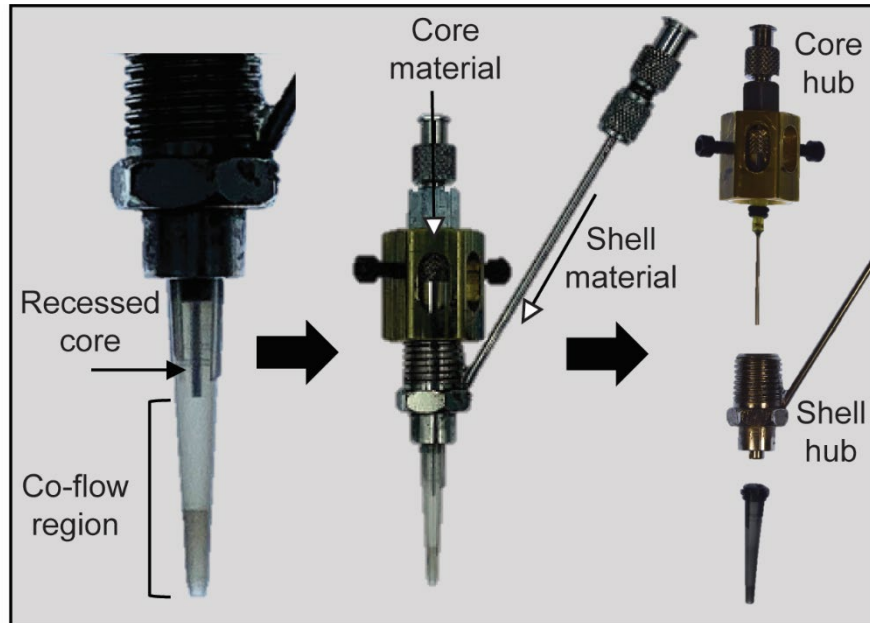


Figure 2.3. Optical image of C-S nozzle components. Moving left to right, a recessed core nozzle and co-flow region, complete nozzle assembly, and modular breakdown is displayed.

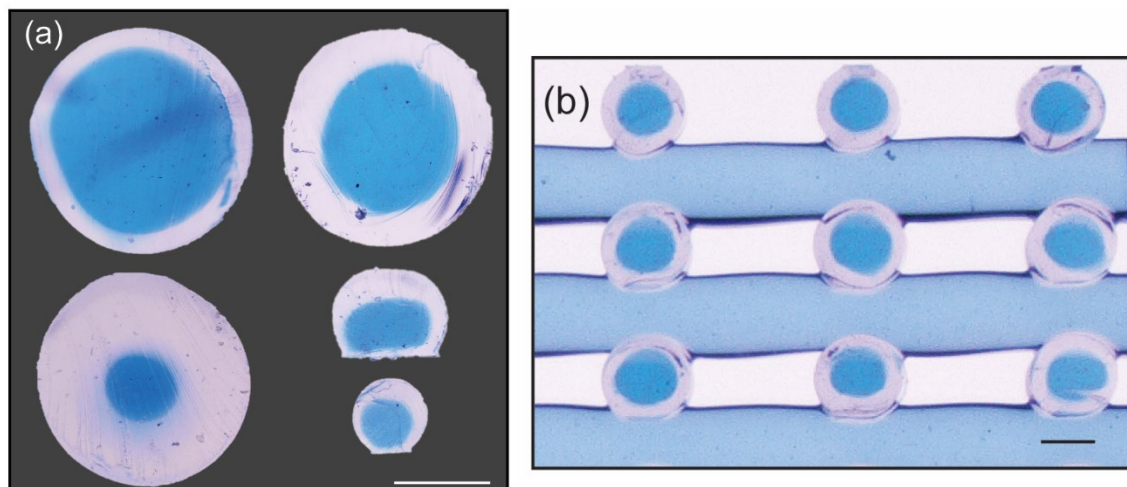


Figure 2.4. Initial core-shell prints with silicone. a) Cross-sectional images of printed silicone core-shell filaments demonstrating the ability to change core volume fraction and filament diameter. b) Cross-sectional view of a printed silicone C-S lattice structure. All scale bars = 500 μm

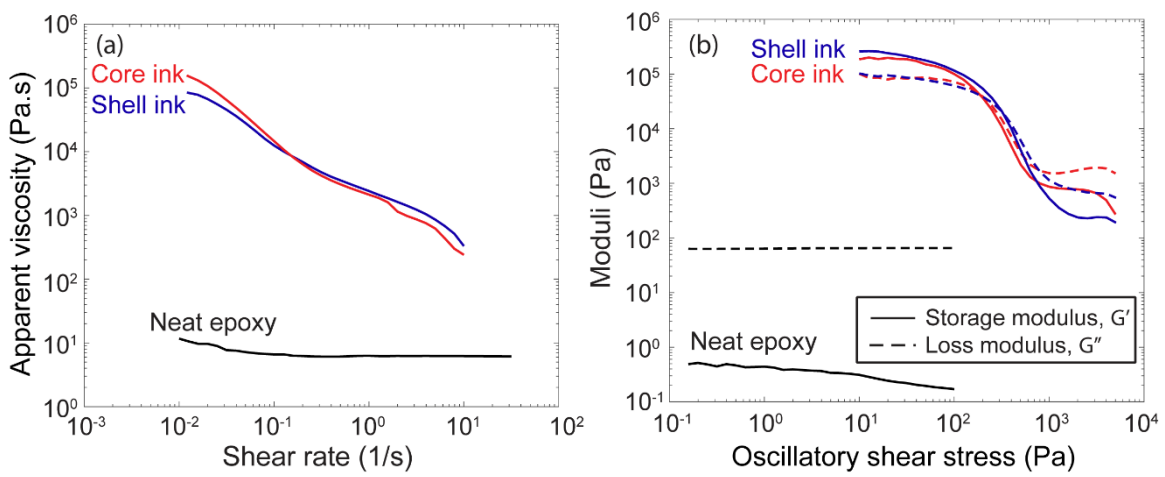


Figure 2.5 Rheological behavior of formulated inks. Log-log plots of (a) apparent viscosity vs shear rate and (b) storage and loss moduli vs oscillatory shear stress for neat epoxy and epoxy-based foam (core) and CF composite (shell) inks

($G' \sim 2 \times 10^5$ Pa) and shear yield stress ($\tau_y, \sim 2 \times 10^2$ Pa) enabling them to maintain shape during printing and curing steps (24 hrs at 100°C).

2.4.4 Initial Foam Mechanical Properties

At first, the mechanical properties of the newly formulated syntactic foam were quantified by printing single layer flexural bars, compression blocks (**Figure 2.6a**), and honeycombs (**Figure 2.6b**), where extrusion was accomplished utilizing pneumatic pumps. The printed foam displayed a low density of 0.68 g cm^{-3} , matching the theoretical density, based on the density and volume fraction of constituents. Three-point flexure specimens exhibited a flexural modulus (E_{flex}) of 2.8 GPa and flexural strength of 36 MPa. In compression, a modulus of 3.4 GPa and strength of 71.3 MPa were observed, comparable to conventional syntactic foams of similar density [27, 60].

2.4.5 Characterization of Printed Core-shell Structure

To investigate fabrication of the core-shell architecture, single layer C-S samples (**Figure 2.7a**) were initially printed with a large 1.6-mm-diameter shell nozzle to decrease probability of clogging, subsequently followed by use of a smaller 1.2-mm-diameter nozzle for printing of finer features. Here, printing utilized continuous cavity volumetric pumps to control flowrate and vary the core volume fractions (V_f). To demonstrate printing of more complex structures, C-S triangular honeycombs were also fabricated (**Figure 2.7b**). Optical microscopy of the surface of printed structures (**Figure 2.7c**), along with x-ray computed tomography (xCT) renderings (**Figure 2.7d**) reveal carbon fibers 200-400 μm in length, strongly aligned with the print direction along with GMBs forming the foam core. Optical micrographs of single-layer cross-sections

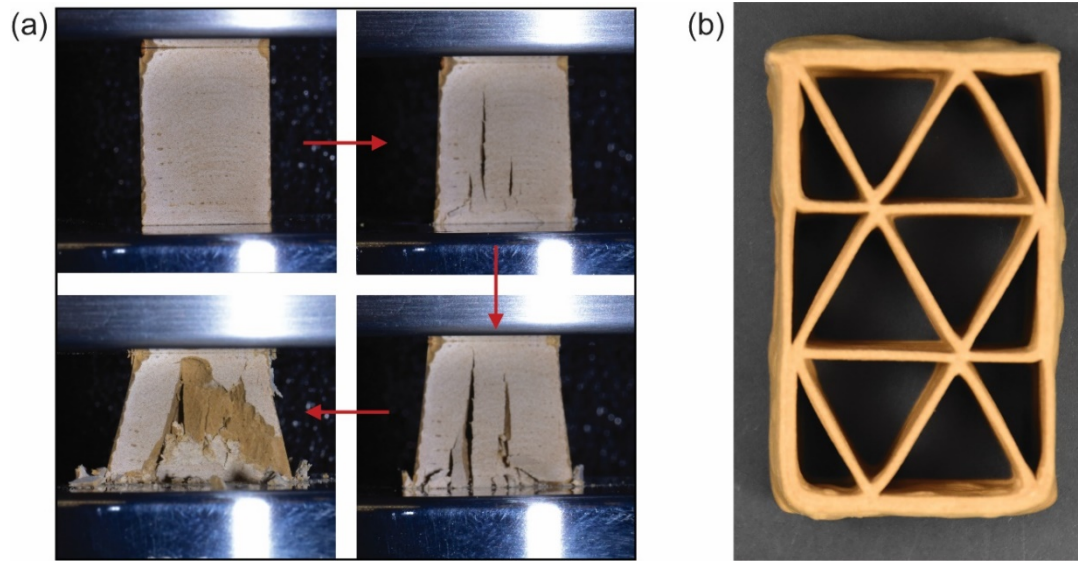


Figure 2.6. Syntactic foam printing. a) Syntactic foam compression testing of nominally 15 mm (W) x 15 mm (T) x 20 mm (H) blocks printed utilizing air pressure for extrusion. b) Printed triangular honeycomb foam sample (40 mm (W) x 20 mm (T) x 20 mm (H)).

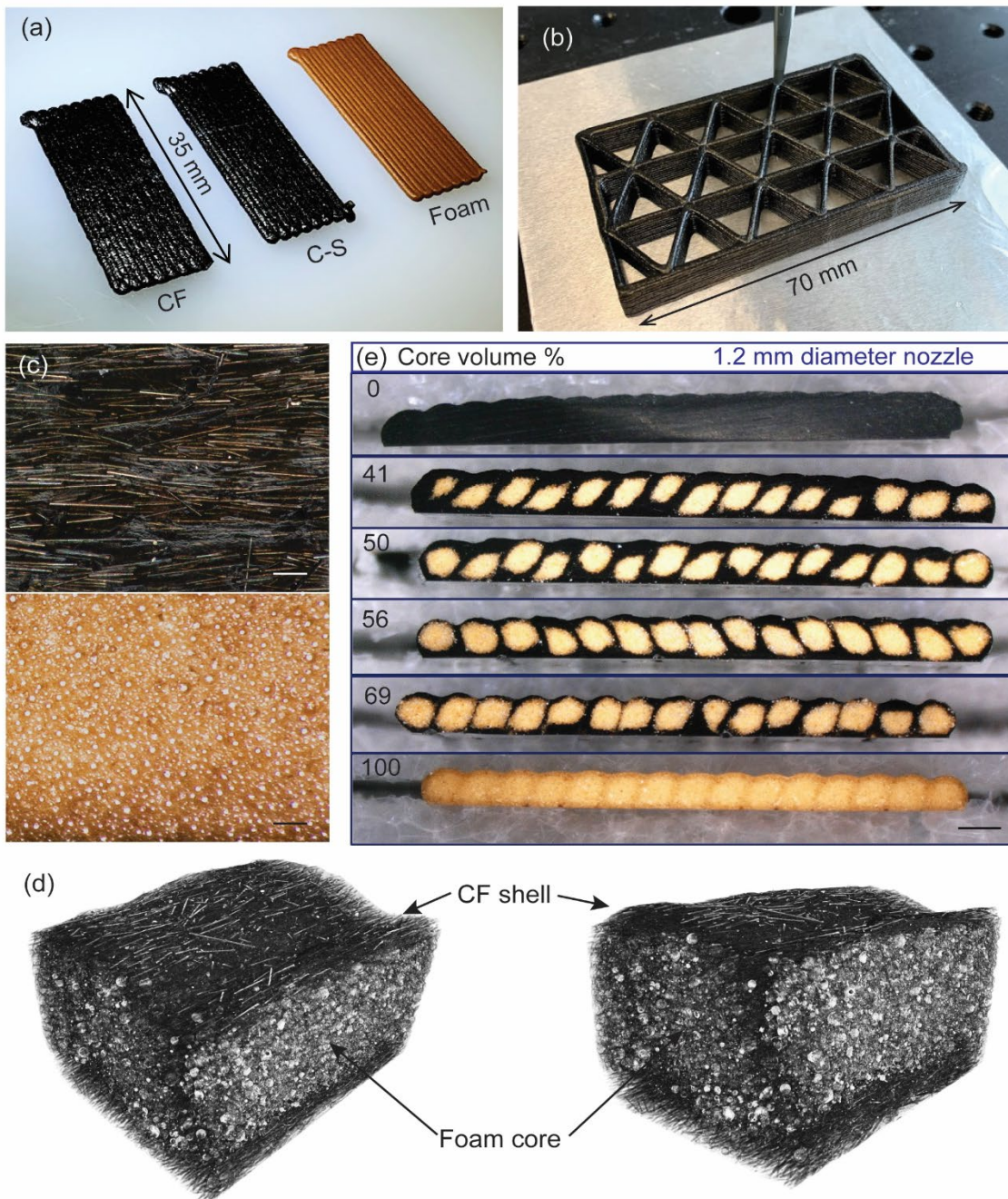


Figure 2.7. Printed C-S specimens. a) Single layer CF composite, C-S, and foam flexural samples. b) C-S printing of a lightweight triangular honeycomb structure. c) Micrographs of the top filament surface showing aligned CFs (100-400 μm length) and dispersed GMBs (20-80 μm diameter) in printed filaments. [Scale bar = 200 μm] d) X-ray CT 3D renderings of printed C-S samples. e) Cross-sectional micrographs of 1.2 mm C-S flexure samples. [Scale bar = 1 mm]

(**Figure 2.7e**) show successful fabrication of C-S structured filaments with no apparent printing induced porosity and minimal defects in the 1.2-mm samples. In contrast, 1.6-mm samples show notable eccentricity (**Figure 2.8**), defined as the distance from the center of the core to the center of the sample, along with irregular core geometry and insufficient filament overlap. Samples comprised of 100% CF composite ($V_f = 0$) exhibited a density of 1.41 g cm^{-3} while the 100% foam samples ($V_f = 1$) displayed densities of 0.87 g cm^{-3} when using a 1.6-mm-diameter nozzle, and 0.84 g cm^{-3} when using a 1.2-mm-diameter nozzle, notably higher than previous samples printed using only air pressure to drive extrusion. The higher density and discrepancy between prescribed and printed core volume fraction (**Figure 2.9a**) are attributed to fracture of GMBs during the pumping process. Interactions between GMBs within the ink, and between GMBs and the rotor and stator of the continuous cavity pump led to high pressure and shear stresses that can cause GMBs to rupture. Fracturing of GMBs, particularly larger, weaker ones, leads to increased density in the extruded ink and lower core volume than prescribed. Printing filaments with higher core volume fractions requires higher core flowrates, which, in turn, increases pressure and shear stresses in the pumps, leading to higher rates of GMB attrition. This phenomenon can be seen in the comparison between the prescribed flow rate and the measured core volume fraction (**Figure 2.9b**). A direct relation is apparent, with the largest difference arising at the highest flowrate ($1200 \mu\text{L min}^{-1}$, 1.6-mm-nozzle). Volumetric pumps provide the necessary control over flowrate and filament composition (V_f) but further investigation into optimal composition and print parameters is needed to minimize rupture of GMBs and obtain lower as-printed density.

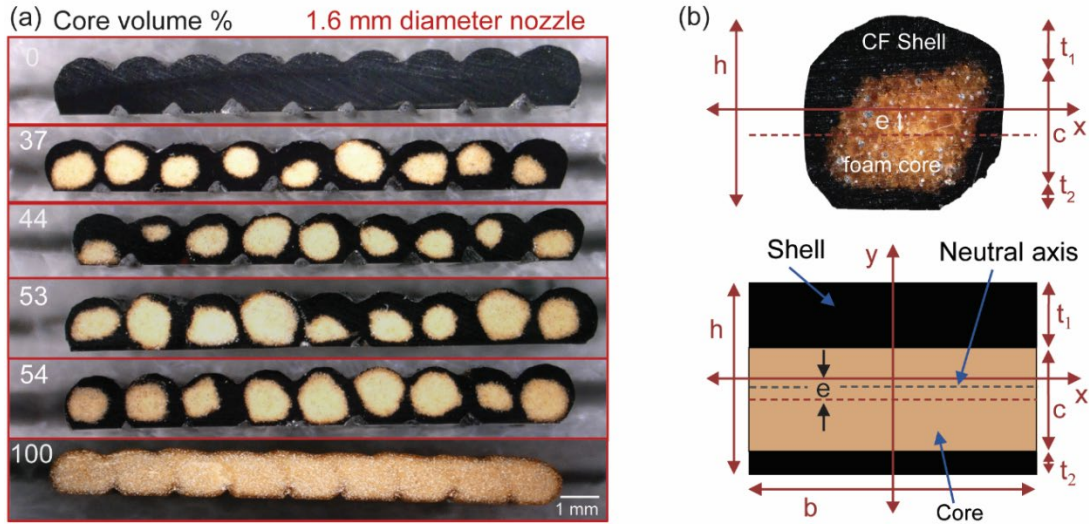


Figure 2.8. Core-shell cross-sections and core eccentricity. a) Cross-sections of 1.6-mm samples show existence of print defects from insufficient filament overlap and flowrate, attributed to GMB fracture at the high required flowrates. b). Core eccentricity, e , and sandwich idealization schematic (bottom) of the C-S samples used for the model.

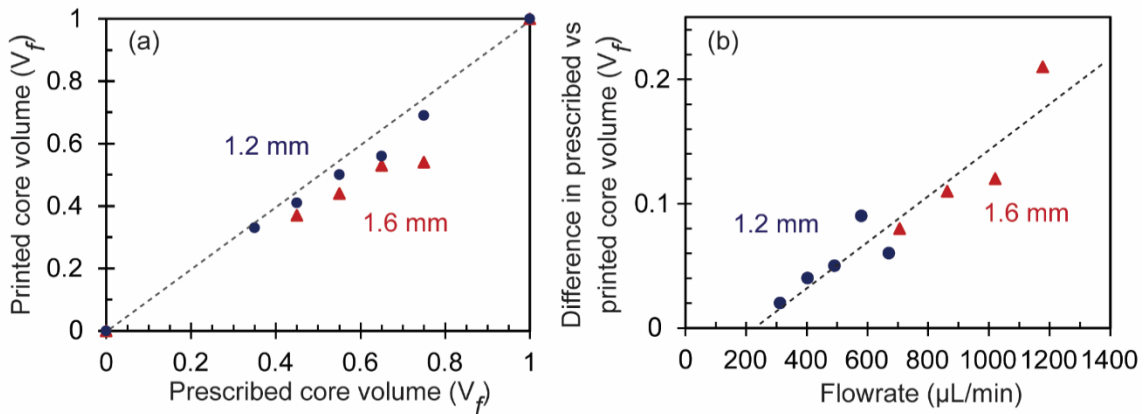


Figure 2.9. Printed versus prescribed core volume and relationship with flowrate. a) Comparison between the measured printed core volume and the prescribed core volume during printing. b) The difference in prescribed and printed core volumes increases with increasing core flowrate due to increased attrition of the GMBs and resulting increase in density.

To further investigate printed C-S structure, xCT scans (**Figure 2.10**) and optical microscopy were conducted on the 1.2-mm samples with a V_f of 0.65. End-on images (**Figure 2.10a**) reveal the GMB-filled foam core, comprised of GMBs with diameters up to ~ 60 μm , surrounded by highly aligned CFs in the shell, indicated by near circular fiber cross-sections. CFs align during extrusion, producing an advantageous increase in stiffness along the print direction [61-63]. An orthogonal view (**Figure 2.10b**) further reveals the high degree of CF alignment in the shell.

The core-shell interface is pore-free and distinct (**Figure 2.10c**), with a few small regions where GMBs and CFs are mixed, seen in **Figure 2.10a**, and small regions where adjacent cores bridge one another (**Figure 2.10c**). Crescent-shaped glass remnants are visible in the core (**Figure 2.10d**), supporting the hypothesis that some GMBs rupture in transit through the pumps.

2.4.6 Flexural Testing of Core-shell Samples

To quantify the potential mechanical benefits of the C-S architecture, single-layer samples were tested under three-point bending. Flexural modulus (E_{flex}) and strength are plotted against density in **Figure 2.11a** and **2.11b**, including a baseline data set comprising the core and shell materials simply mixed together at prescribed volume fractions. Measured properties are summarized in **Table 2.2**. Samples comprised of 100% CF composite display the highest mechanical properties, with the samples printed using 1.6-mm-diameter nozzle exhibiting the largest average E_{flex} of 23 GPa with a density of 1.41 g cm^{-3} . A noteworthy phenomenon was observed in the 1.2-mm samples, where introduction of a foam core up to $0.41 V_f$, produced statistically similar E_{flex} values

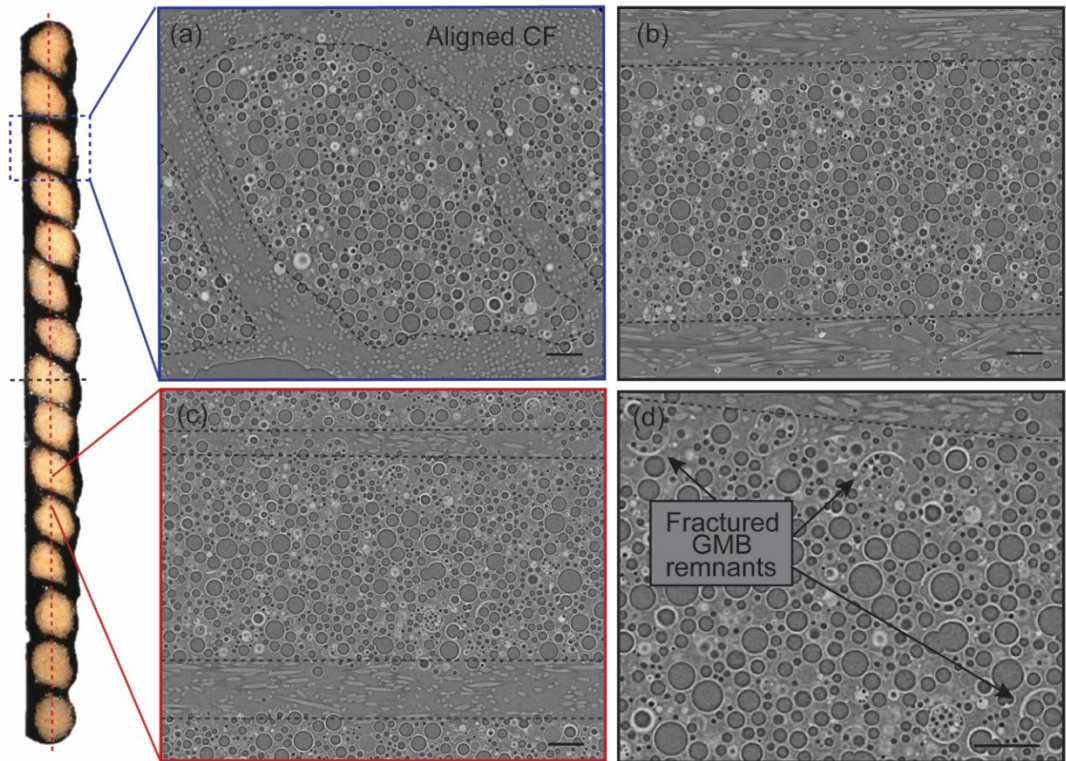


Figure 2.10. X-ray CT micrographs. a) end-on, b) side-on, c) and top-down views. C-S filament architecture consists of a highly aligned CFs in the shell surrounding the syntactic GMB foam core. d) Hemispherical glass fragments indicate fractured GMBs. All Scale bars = 100 μm.

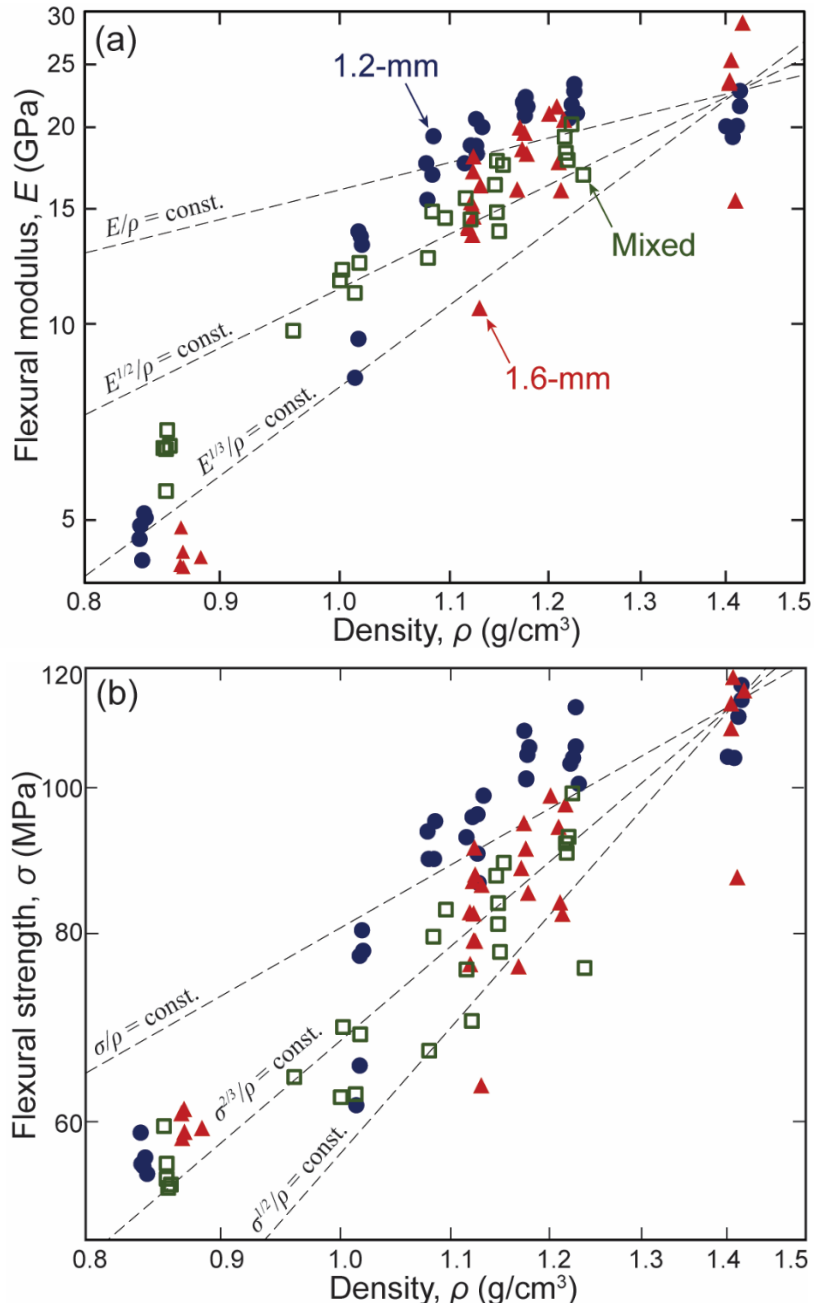


Figure 2.11. Mechanical properties and analytical model predictions. a) Flexural modulus vs density measurements with material design guidelines. b) Flexural strength vs density measurements with material design guidelines.

Table 2.2. Core flowrate, mechanical properties, density, and average normalized eccentricity for printed samples

1.2-mm-diameter tapered nozzle							
Core vol. %	Core flowrate ($\mu\text{l}\cdot\text{min}^{-1}$)	E_{flex} (GPa)	Flexural Strength, σ (MPa)	Density ($\text{g}\cdot\text{cm}^{-3}$)	$E_{flex}^{1/3} / \rho$ ($\text{GPa}^{1/3}\text{g}^{-1}\text{cm}^3$)	Standard deviation	Average \bar{e}
0	0	20.72	110.46	1.41	1.94	0.04	-
33	312	21.82	105.71	1.23	2.28	0.04	0.29
41	402	21.55	104.65	1.18	2.37	0.02	0.31
50	491	19.24	93.43	1.13	2.38	0.04	0.35
56	580	17.37	92.11	1.09	2.38	0.07	0.33
69	670	11.67	72.49	1.02	2.22	0.17	0.39
100	690	4.81	56.66	0.84	2.01	0.04	-
1.6-mm-diameter tapered nozzle							
0	0	23.29	108.97	1.41	2.02	0.15	-
37	706	19.32	91.34	1.21	2.22	0.10	0.46
44	863	18.45	87.07	1.17	2.25	0.06	0.42
53	1020	15.46	82.99	1.13	2.21	0.15	0.42
54	1177	14.28	79.91	1.12	2.16	0.03	0.35
100	1045	4.44	59.76	0.87	1.88	0.04	-
Mixed samples (1.2-mm-diameter tapered nozzle)							
0	-	-	-	1.41	-	-	-
29	-	18.46	89.95	1.22	2.16	0.06	-
40	-	16.02	83.79	1.15	2.19	0.08	-
47	-	14.37	74.96	1.10	2.21	0.05	-
63	-	11.39	65.33	1.00	2.25	0.04	-
84	-	6.35	55.84	0.86	2.15	0.06	-
1	-	-	-	0.75	-	-	-

(21.8 ± 1.1 and 21.5 ± 0.5 GPa) compared to the monolithic CF composite (20.7 ± 1.4 GPa), while reducing the density by 16% from 1.41 g cm^{-3} to 1.18 g cm^{-3} . We hypothesize that the presence of the foam core in the co-flow region increases the fiber alignment in the shell compared to printing the composite material alone. The resulting increased stiffness offsets the loss of CF composite in the core and results higher flexural moduli. Support for this hypothesis will be discussed with the mechanics model shortly. Foam samples displayed the lowest average E_{flex} of 4.8 and 4.4 GPa at 0.84 and 0.87 g cm^{-3} for samples printed with the 1.2- and 1.6-mm nozzles, respectively. The CF composite displayed the highest average flexural strength, σ_{flex} , of 110 MPa, whereas the foam showed the lowest at ~ 60 MPa.

The C-S samples printed with the 1.2-mm-diameter nozzle exhibit superior strength throughout the density range, with approximately 25% higher flexural strength than the mixed baseline samples (**Figure 2.12**). This may be attributed to the C-S architecture positioning the higher-strength CF composite furthest from the neutral axis of bending, where it is used most efficiently.

Investigation into polished cross-sections (**Figure 2.13a-b**) and the flexural fracture surfaces (**Figure 2.13c-f**) supports evidence of a strong, pore free interface between the core and shell region, showing no distinctive interface line, other than indicated by different filler material (CF or GMB) in the optical and SEM micrographs (**Figure 2.13b-d**). The shell fracture surfaces (Figure S4e) reveal a weak bond between matrix and CF, indicated by minute fracture induced voids around the fibers and fiber pullout. However, fractured CF's indicate the load was adequately transferred from the matrix, enabling the fibers to provide effective reinforcement. In comparison, the core

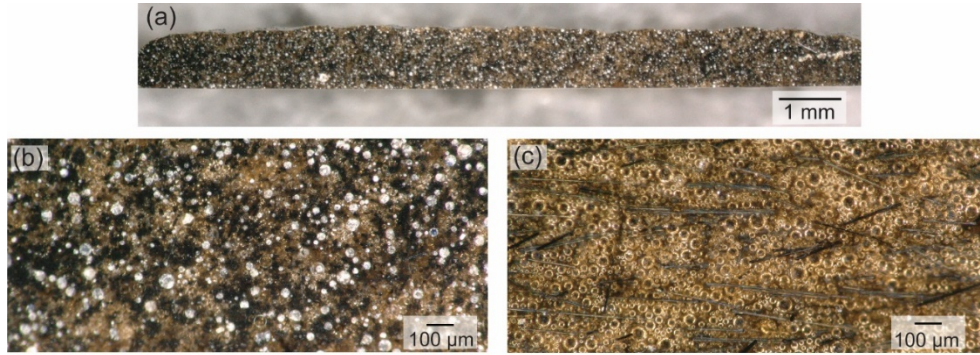


Figure 2.12. Mixed sample micrographs. a) and b) Optical micrographs of cross-section of mixed sample and c) filament surface.

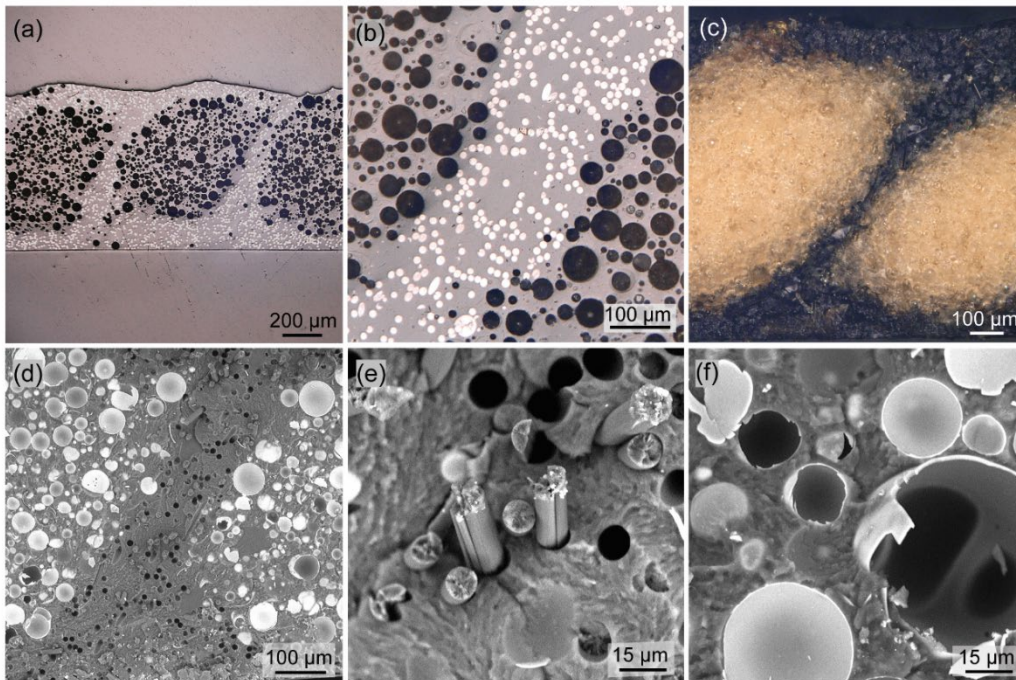


Figure 2.13. Optical and scanning electron microscopy of 1.2-mm-diameter core-shell samples. a) and b) Optical micrographs of polished core-shell cross-sections c) Optical micrograph of fracture surface. d-f) SEM micrographs showing flexural fracture surfaces. d) and e) Carbon fiber pullout and f) micro balloon failure is visible.

fracture surface (Figure S4f) reveals a stronger bond between GMB and epoxy matrix, indicated by absence of fracture induced voids around the GMB and minimal GMB pullout. Failure in the core region is seen to occur mainly by GMB fracture. In both regions, matrix deformation is prominently seen.

2.4.7 Selection of Material Index and Comparison

Structural members that seek to maximize elastic stiffness with minimal weight can be evaluated and compared using three different figures of merit. For those loaded axially, the specific stiffness (E/ρ) is the appropriate material index, while for beams with fixed span and cross-sectional shape, but variable size, the relevant performance metric is $E^{1/2}/\rho$, and for panels in flexure with fixed span and depth but variable thickness, as well as panels subject to elastic buckling, $E^{1/3}/\rho$ is the relevant metric. Included in **Figure 2.11a** and **2.11b** are these design guidelines for lightweight axial members (E/ρ and σ/ρ), beams ($E^{1/2}/\rho$ and $\sigma^{2/3}/\rho$), and panels ($E^{1/3}/\rho$ and $\sigma^{1/2}/\rho$) [64]. Based on these material indices, we can see that our core-shell hybrids outperform the base constituents for all weight sensitive applications. However, in the context of 3D printing, our primary goal is to enable low-density cellular structures with enhanced mechanical properties. In this case, the cell walls are best approximated as panels, and $E^{1/3}/\rho$ is the most meaningful material index for comparison. In **Figure 2.14a**, modulus data is plotted using the material index for a lightweight, stiff panel ($E^{1/3}/\rho$) as a function of V_f . 1.2-mm samples are superior in comparison to other tested samples, exhibiting up to a 25% increase in performance over that of either constituent alone, solely due to the C-S architecture. As V_f increases up to ~ 0.6 , $E^{1/3}/\rho$ also increases, reaching a maximum average value of

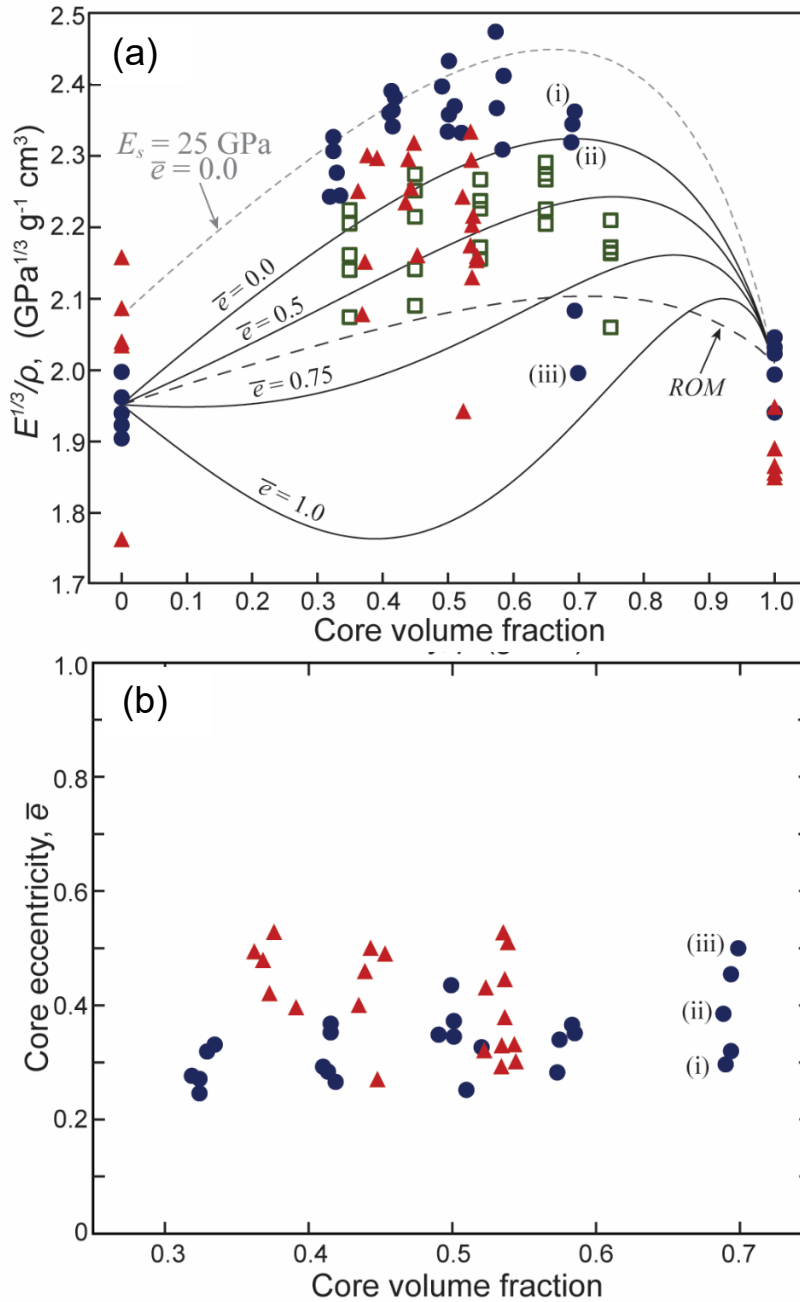


Figure 2.14. Material indices and core eccentricity. a) $E^{1/3}/\rho$ vs. measured core volume fraction. Solid lines are model predictions for various levels of eccentricity. The long-dashed line represents the rule-of-mixtures prediction for homogeneously mixed constituents, and the short-dashed line represents the model prediction for a shell with flexural modulus of 25 GPa. d) Eccentricity measurements. Data points labeled (i), (ii), and (iii) are indicated in both c) and d) showing that higher eccentricity correlates with lower performance

2.38 $\text{GPa}^{1/3}\text{g}^{-1}\text{cm}^3$ and a maximum single measured value of 2.47 $\text{GPa}^{1/3}\text{g}^{-1}\text{cm}^3$, for the 1.2-mm samples. A similar trend is observed for both the 1.6-mm C-S samples and the mixed baseline samples, albeit at lower performance values.

2.4.8 Core Eccentricity Measurements and Model Analysis

Defining normalized eccentricity, \bar{e} , as the average distance from the center of the core to the center of the filament, normalized by the theoretical thickness of the shell, enables quantification of the mechanical impact of core eccentricity. Measurements (**Figure 2.14b**) indicate greater eccentricity in the 1.6-mm samples than in the 1.2-mm samples, qualitatively seen by comparing cross-sections from **Figure 2.7e** and **Figure 2.8a**. Although the scatter in data is significant, inspection of corresponding data points in **Figure 4c** and **4d** supports the hypothesis that \bar{e} is an indicator of mechanical performance: point (i) exhibits the smallest $\bar{e}=0.3$ and corresponds to the highest performance index (2.36 $\text{GPa}^{1/3}\text{g}^{-1}\text{cm}^3$) while point (iii) exhibits the largest $\bar{e}=0.5$ and corresponds to the lowest performance index (1.99 $\text{GPa}^{1/3}\text{g}^{-1}\text{cm}^3$). This behavior holds true for most printed samples, but clearly a more in-depth study of this complex phenomenon is warranted.

To estimate effects of \bar{e} on performance, a model is proposed that considers the printed specimens as a sandwich structure (**Figure 2.8b**). Model derivation is reported in the Appendix section “Eccentric sandwich composite model”. The model follows the derivation of the effective modulus of composites in bending [65] and results in the following expression:

$$E_{f,eff} = \alpha[E_s + (E_c - E_s)V_f^2] \quad (\text{Eq.2.1})$$

where E_c is the flexural modulus of the foam core, E_s is the flexural modulus of the composite shell, and α is the knockdown factor for eccentricity, which is a function of \bar{e} , E_c , E_s , and V_f (S1.35). Using the average properties from the monolithic samples printed with the 1.2-mm nozzle to define E_c , ρ_c , E_s , and ρ_s , model predictions are plotted in **Figure 2.14a** for varying levels of eccentricity.

The mechanical model predicts the correct trends, but lower performance than is actually observed. However, comparing fiber alignment in the C-S (**Figure 2.7 c and d, and 2.10 a-d**) and CF composites (**Figure 2.15**) suggests that the average fiber orientation may be higher in the C-S samples than in the monolithic CF samples that were used as input to the model. This hypothesis is consistent with the fact that extrusion processes generally result in higher orientation of fibers, whiskers, or polymer chains near the wall of an extrusion die or nozzle than in the middle of the flow[66-70]. This feature has been observed experimentally in thermoplastic/CF printed composites [67, 69] and extruded glass fiber-reinforced polypropylene [66], and has been predicted numerically for both small and large deposition nozzles [68, 70]. In our specific case, we have the added fact that the presence of the core nozzle in center of the flow path further disrupts fiber orientation as the material flows around the core nozzle to fill the void space that the core material would normally occupy. When the core is present, a higher proportion of the shell material experiences higher shear rate and shear stress near the wall, potentially leading to higher average orientation of fibers when printing C-S samples. In fact, using a shell modulus of 25 GPa results in better matching between model predictions and experimental data (**Figure 2.14a**). This suggests a potential

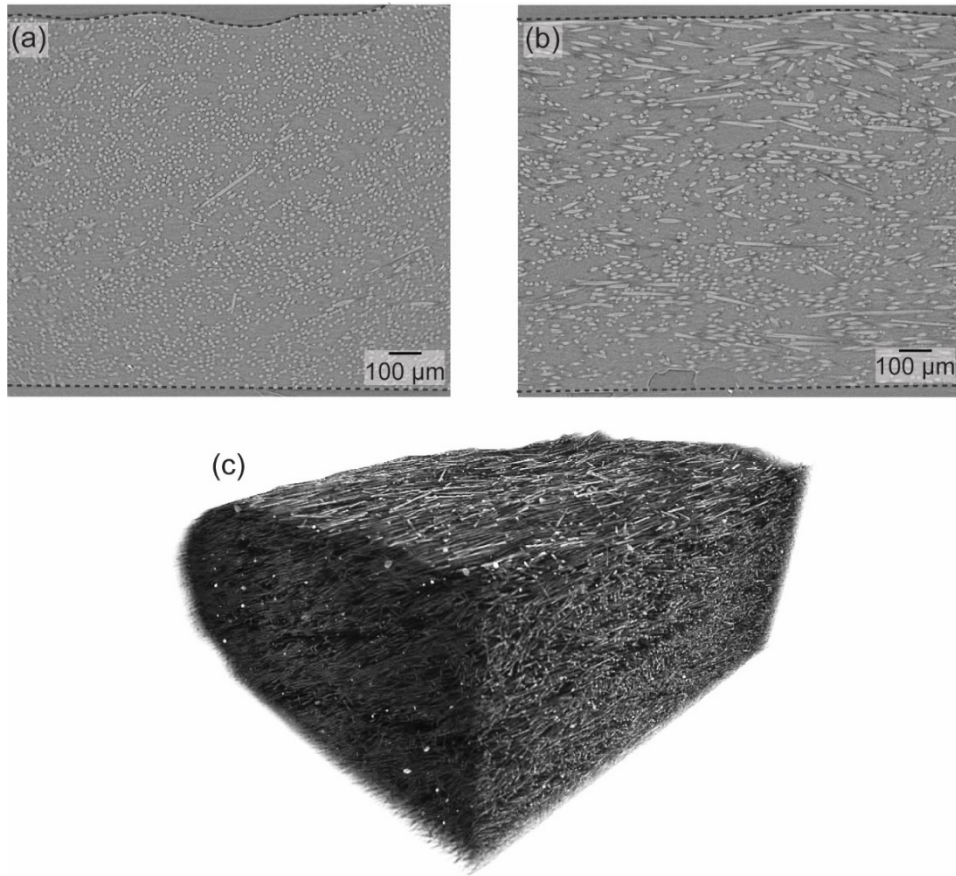


Figure 2.15. X-ray CT tomographs of CF samples. a) end-on and b) side-on views of CF composite samples. c) 3D rendering of CF composite.

synergistic effect: C-S printing more efficiently utilizes each constituent *and* improves the absolute properties of the shell composite.

2.5 Conclusion

In summary, we have demonstrated a method to 3D-print lightweight architected filaments, consisting of a new syntactic foam ink surrounded by a stiff carbon fiber-reinforced shell, that exhibit superior mechanical properties. Our modular coaxial nozzle has the capability to print highly loaded, fiber-reinforced epoxy feedstocks to effectively fabricate components with controlled geometry, composition, and architecture. A new mechanics model successfully predicts mechanical properties of the C-S architecture and accounts for potential eccentricity of the core. This approach can be readily applied to complex geometries, such as cellular structures, to produce structural components that extend the combined boundaries of low-density and high mechanical performance.

**3. 3D PRINTING OF GLASS MICROBALLOON SYNTACTIC
FOAMS VIA MATERIAL EXTRUSION ADDITIVE
MANUFACTURING**

3.1 Abstract

Syntactic foams exhibit high specific properties and are widely utilized in weight sensitive structural applications. Syntactic foams are amendable to fabrication via direct ink write (DIW) additive manufacturing (AM), by incorporation of glass microballoons (GMB) into an epoxy feedstock ink. AM of syntactic foams offers benefits over conventional routes, such as increased design flexibility, and the ability to print foam hybrid materials. However, GMBs are prone to failure during extrusion, as shown previously in Chapter 2, and result in a detrimental increase in density. In this work, the relation between GMB loading, extrusion pressure, nozzle diameter, and flowrate on printed density are investigated to understand the conditions leading to GMB failure and optimize those process parameters. GMB failure was determined to predominantly occur during extrusion through the volumetric pumps, but noticeable density increase, especially at high flowrates, indicates GMB failure also occurs in the nozzle tip. Parameter optimization led to noticeable improvement; however, a new ink was formulated with GMBs (S32HS) that exhibit a lower average diameter and higher crush strength, which ultimately enabled printing of foams without prominent GMB failure. S32HS foam samples displayed a near theoretical printed density (0.69 g/cc) with a high compressive modulus (4.94 GPa) and strength (100 MPa). Implementation of the higher strength GMBs into the C-S architecture enabled further improvement, with a 5% increase over previous material index values ($E^{1/3}/\rho$) of the C-S hybrid. Successful development and printing of a new S32HS foam shows potential for application in high-performance, lightweight structures.

3.2 Introduction

Polymer foams, materials which have engineered voids or porosity, have attracted attention for their low density and high specific properties. Multiple types of foams exist, ranging from conventional single-phase foams made by expanding a single polymer, to composite foams, constituted of a polymer foam with additional solid phases such as particles or fibers. This study focuses on polymer syntactic foams (SFs), a special type of particle reinforced, closed cell, composite foam consisting of hollow spheres dispersed in a polymer matrix [26]. These hollow spheres can range in size from nanometers to a few millimeters in diameter and can be made from a variety of materials such as glass [71, 72], carbon [24, 73], or ceramic (cenospheres) [25, 74]. While various options are available for matrix polymer and microsphere material, glass microballoons (GMBs) (20-200 μm diameter) are the most prevalent SF constituent. GMBs are advantageous for use in structural applications due to displaying a spherical morphology, less defects and irregularities, greater control over microsphere size, better predictability in properties, and overall higher quality when compared to other microballoons [72, 73, 75]. Due to their closed-cell nature, low density, high buoyancy, low coefficient of thermal expansion, and high specific properties, SFs have found wide use in marine, automotive, and aerospace sectors. Examples include use in buoys, rudders and bodies of submarines, construction of deep sea exploration vehicles, hollow areas in aircraft, propeller fillers, wing-mounted antennae, and the core in sandwich panel structures [27, 75].

Syntactic foams are commonly fabricated through conventional processing methods of injection and compression molding, which imposes constraints on design freedom and requires expensive tooling in order to fabricate complex parts [25, 72, 75].

Alternatively, material extrusion additive manufacturing (AM), a process in which components are constructed in a layer-by-layer fashion via direct material deposition, allows fabrication of custom, tailored, complex geometries that would be otherwise be costly or unattainable through conventional routes. AM of polymer SFs is still in its infancy but recent work utilizing fused filament fabrication (FFF) has demonstrated the feasibility of utilizing material extrusion AM processes. For example, Bharath et al. blended up to 60 volume percent (vol.%) GMBs into a high density polyethylene (HDPE) thermoplastic matrix to produce a lightweight foam feedstock material which enabled printing via FFF [75]. Similarly, Singh et al. utilized 40 vol % GMBs in HDPE to print three-phase foams, consisting of a microstructure with matrix, GMBs, and air voids [76]. Utilizing fly ash cenospheres (up to 60 vol. %) instead of GMBs in an HDPE matrix, Patil et al. also successfully printed a three-phase foam geared toward lightweight buoyant structures [77]. While these works have produced quality foam parts, they experience challenges such as component warpage from heating and cooling steps, insufficient adherence to the substrate, weak adhesion between layers, large porosity between layers and filaments, and a high degree of difficulty in manufacturing quality SF filaments that are inherent to the FFF process [75, 76, 78, 79]. To overcome these limitations, we utilize direct ink write (DIW), another type of material extrusion additive manufacturing which consists of the direct deposition of viscoelastic thermoset feedstock materials (inks) at ambient temperatures. DIW is conducive to SF printing, eliminating the need for filament feedstock and thermal cycles during printing, and employing a post print thermal cure which provides thorough crosslinking and adhesion between layers. In Chapter 2, the significant potential of DIW printing of SFs was demonstrated by

successfully formulating a new GMB SF ink that was used to print complex foam structures in addition to being utilized as a low-density core material in hybrid core-shell architectures printed via DIW which exhibited superior specific properties [41].

Although research on DIW printing of SFs is scarce, Nawafleh et. al followed a similar approach by using epoxy/GMB inks to print SF samples that displayed high specific properties but also exhibited higher printed densities than theoretical, indicating the occurrence of detrimental GMB fracture [80].

In order to optimize the performance of DIW printed, lightweight foam structures, as well as maximize the benefit of the C-S architecture, it is crucial to obtain a low density in the final printed foam. Density reduction through GMB incorporation is dictated by two factors: i) the volume fraction of GMBs in the feedstock ink and ii) the number of intact GMBs after printing [72]. Following the ink formulation presented in Chapter 2, the maximum limit of GMB volume fraction which still allowed consistent printing was determined and set at 58 vol.%, comparable to loadings (~ 60 vol.%) attained in FFF [75] and DIW feedstocks [80]. However, prominent GMB fracture occurred during extrusion, resulting in a detrimental density increase. Thus, this work addresses the need to investigate and optimize print parameters, mainly nozzle size and flowrate, in order to minimize GMB failure, decrease printed foam density, and largely advance development of printed lightweight foam structures.

In this study, two types of GMBs (S32 and S32HS) of the same density are incorporated in foam inks at volume loadings of 45, 50, and 58 percent and printed with three different nozzle diameters. Pressure measurements are taken with a pressure sensor placed between the pump exit and nozzle tip at varied flowrates (200-1400 $\mu\text{L min}^{-1}$) and

compared with printed density. Decreased density is achieved utilizing S32HS GMBs and subsequently used to print flexural bars, compression blocks, and honeycomb samples for mechanical testing. Finally, flexural core-shell samples are printed with the new S32HS ink, exhibiting up to a 5% increase in specific flexural stiffness ($E^{1/3}/\rho$) over values reported in previous C-S work [41].

3.3 Materials and Methods

3.3.1 Epoxy-based Syntactic Foam Ink and Glass Microballoons

Epoxy-based syntactic foam inks were prepared following the same formulation and mixing protocols presented in previous work (Chapter 2). Identical constituents (**Table 2.2**) of Epon 826 epoxy resin, VSO3 latent curing agent, DMMP diluent, and nanoclay rheological modifier were used. Two types of commercially available GMBs, S32 and S32HS (3M Materials, St. Paul, MN), were utilized as fillers. These GMBs exhibit matching morphology and composition, consisting of hollow spheres with thin walls made of soda-lime-borosilicate glass, and densities of 0.32 g cc^{-1} . They differ in strength, with S32HS exhibiting triple the crush strength (6,000 psi, 41.4 MPa) compared to S32 GMBs (2,000 psi, 13.8 MPa). The difference in strength is driven by the diameter of the particles, where S32HS and S32 GMBs display 25 μm and 40 μm average particle diameters, respectively. Physical properties of GMBs reported by the manufacturer are displayed in **Table 3.1** [81-83]. Scanning electron micrographs of GMBs in **Figure 3.1** reveal spherical morphology and a noticeable size difference. Ink constituents were kept at constant proportions with respect to the epoxy matrix, while GMB loading was varied to produce inks with 45 vol.%, 50 vol.%, and 58 vol.% S32 GMBs, hereby referred to as

Table 3.1. Glass microballoon properties

Property		S32	S32HS
Composition		Soda-lime-borosilicate glass	
Shape		Hollow spheres with thin walls	
True density (g/cc)		0.32	0.32
Crush strength (MPa)		13.8 (80% survival)	41.4 (90% survival)
Particle Size Distribution (μm)	10 th %	20	--
	50 th % (average)	40	25
	90 th %	70	--
	Top size (95 th %)	80	47

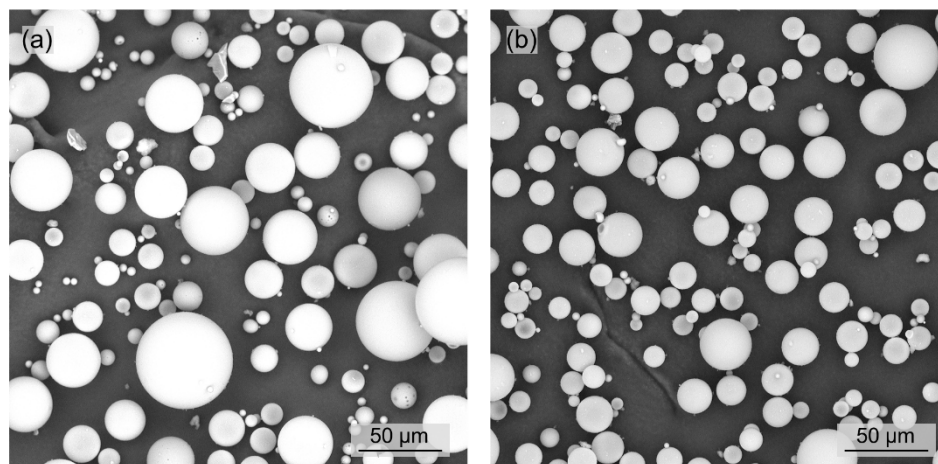


Figure 3.1. Scanning electron micrographs of GMBs. a) S32 and b) S32HS glass microballoons. A spherical morphology is seen with S32 GMBs displaying larger diameters, up to 80 μm .

S32-45, S32-50, and S32-58, respectively, and an additional ink with 58 vol.% S32HS GMBs (S32HS-58). All mixing was conducted using a planetary mixer under vacuum at 0.1 atm following the procedures outlined in Chapter 2.

3.3.2 Parallel Plate Rheology

The rheological properties of the inks were measured under laboratory ambient temperature (~ 21 °C) using a Discovery HR-2 Rheometer (TA Instruments, New Castle, DE) with a 25 mm parallel plate geometry and a gap distance of 1 mm for all foam-based inks. The apparent viscosity was characterized using continuous flow sweeps, carried out at controlled shear rates (from 0.01 up to 50 s^{-1}), and the viscoelastic properties were measured using oscillatory sweeps conducted at a frequency of 1 Hz under controlled shear stresses (from 10 up to 5000 Pa). All measurements were preceded by a 120 seconds conditioning step at a constant shear rate of 0.01 s^{-1} , followed by an equilibration period for 120 seconds to allow the ink structure to recover.

3.3.3 Direct Ink Write Platform, Extrusion Pressure Measurements, and Sample Printing

After mixing, inks were loaded into 10 ml syringe barrels and centrifuged for 3.5 min at 3600 rpm to remove entrapped air. Syringes were then loaded into pneumatic pressure adapters (HP3, Nordson EFD, Westlake, OH) to feed ink into volumetric dispensing pumps (Eco-pen, ViscoTec America Inc., Kennesaw, GA) utilized for extrusion. Pumps are mounted on the Z-axis of a custom 3-axis DIW platform (ShopBot Tools Inc., Durham, NC) directed by G-code generated from scripts written in Scilab software (Scilab Enterprises, France) to enable printing. All samples were printed on

PTFE-coated aluminum substrates and thermally cured in two steps: 24 hours at 100°C followed by 2 hours at 220°C.

To investigate the extrusion pressure experienced during printing, foam rectangular samples (nominally 35 mm L x 12.5 mm W x 1.75 mm H) were printed with S32-45, S32-50, S32-58, and S32HS-58 inks at flowrates ranging from 200-1400 $\mu\text{l min}^{-1}$. To enable pressure measurement, a pressure sensor (flowplus¹⁶, ViscoTec America Inc., Kennesaw, GA) was connected inline via Luer lock between the volumetric pump exit and the nozzle tip inlet as shown in (**Figure 3.2**). Data was recorded at a frequency of 10 Hz to produce a pressure profile. Samples were printed utilizing straight Luer lock nozzle tips (2.54 cm length, McMaster-Carr, Atlanta, GA) with inner diameters of 966 μm and 660 μm , along with printing directly out of the pressure sensor (1.8 mm ID) to provide a baseline. Print speed was set to match in a 1:1 ratio with the flowrates investigated.

The S32HS-58 ink was used to print flexural samples (35 mm L x 12.5 mm W x 1.75 mm H), compression blocks (15 mm x 15mm x 20mm), and hexagonal honeycombs (7 mm and 14 mm cell size) with the 966 μm nozzle tip and a flowrate of 400 $\mu\text{l min}^{-1}$ for mechanical testing. Flexural samples were tested as printed. Compression blocks were machined on all sides while honeycombs were only machined on the top and bottom to obtain flat, parallel faces prior to compression testing.

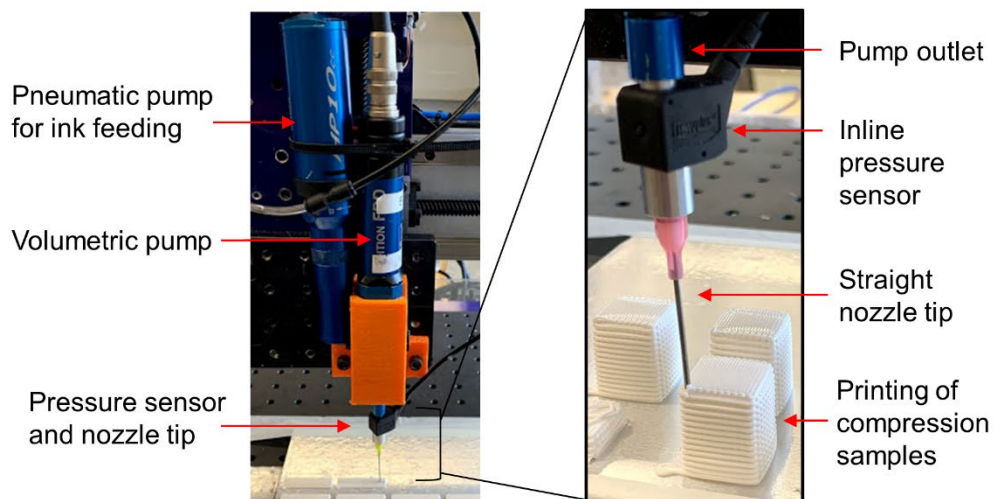


Figure 3.2. DIW hardware for foam printing and pressure measurements. Left, complete pump setup with a pneumatic pump feeding the volumetric pump for extrusion. Right, pressure sensor, inline between the volumetric pump outlet and nozzle tip inlet, during printing.

Finally, to determine the improvement S32HS foam affords to the C-S architecture, single layer C-S samples with prescribed core volume fractions (V_f) of 0.45, 0.55, 0.65, and 0.75 were printed with the new C-S nozzle, following the same printing protocols as described in Chapter 2. A 600- μm -diameter straight nozzle tip and 1.2-mm-diameter tapered nozzle was utilized for the inner core and outer shell nozzles, respectively.

3.3.4 Characterization

Density measurements on all samples were performed via Archimedes method and sample dimensions measured using handheld digital calipers. Optical microscopy was conducted using a VHX-5000 digital microscope (Keyence Corporation of America, Itasca, IL) and scanning electron microscopy was performed with a Phenom Desktop SEM (Nanoscience Instruments, Inc., Phoenix, AZ) to investigate sample geometry, fracture surface, GMB state, and foam structure. Flexural testing was conducted in 3-pt bend configuration on an electromechanical load frame (model 45, MTS Systems Corporation, Eden Prairie, MN) with a 1-kN load cell, span of 25 mm, and a crosshead speed of 0.01 mm s^{-1} . Compression testing was performed on the MTS utilizing spherically seated platens, a 100 kN load cell, and a crosshead speed of 0.01 mm s^{-1} . Honeycombs were only compression tested in the through-thickness orientation. All reported mean values consist of five sample measurements.

3.4 Results and Discussion

3.4.1 Direct Ink Write and Syntactic Foam Processing- Constraints and Considerations

DIW is exploited in this study due to the ability it affords to not only print complex foam structures but also effectively deposit multiple materials, specifically via co-extrusion through the C-S nozzle. Certain inherent characteristics of the DIW process pose challenges in ensuring GMB survival and obtaining low densities in printed GMB foams. GMBs are prone to breakage by compression and shear forces experienced in constraining points and tight clearances and also by impacts between GMBs and GMBs or GMBs and pump components [84]. Minimizing the shear stress and extrusion pressure by minimizing pump speed (flowrate) and maximizing outlet diameter can aid to minimize breakage [85]. Practically, however, some conditions are inherent or necessary for DIW printing and cannot be avoided. Extrusion out of sub-millimeter nozzle tips enables printing of foam structures with fine features and the ability to utilize SFs as a core material in C-S structures. Additionally, volumetric pumps, which impose harsh processing conditions, are necessary to provide a constant flowrate when printing filled epoxy inks and allow the control of composition in printed C-S filaments. Also, time efficiency must also be considered as flowrate can be decreased but at the cost of increased print time and decreased sample output.

To increase probability of GMB survival, progressive cavity pumps, a type of volumetric pump that provides a lower shear environment than an auger-type pump, capable of extruding high viscosity materials, are utilized in this study [86, 87]. It is worth acknowledging that a plethora of options exist for constituent materials of SFs,

making it difficult to find previous studies that utilize the same GMB type and extrusion currently used. To the author's knowledge this is the first study specifically utilizing epoxy-based SF inks with S32 and S32HS GMBs, printed using progressive cavity volumetric pumps via DIW. As such, pilot studies consisting of parameter optimization trials were conducted to gain understanding into the relationship between processing conditions, ink composition, ink rheology, and final printed density which subsequently enables fabrication of high-performance SF and C-S architectures.

3.4.2 Parallel Plate Rheology

For successful DIW printing, foam inks must be viscoelastic, exhibiting the following rheological properties: (i) shear thinning behavior to allow extrusion out of sub-millimeter diameter nozzles under ambient conditions and (ii) once deposited on the substrate, inks must possess a high shear storage modulus, G' , and shear yield strength, τ_y , for shape retention [10, 19, 88]. Rheological behavior of all foam inks investigated are displayed in **Figure 3.3**. In **Figure 3.3a**, GMB volume loading increases the apparent viscosity. The S32HS-58 ink displays the highest viscosity over the probed shear rate range, showing a viscosity of 605 Pa.s at a shear rate of 10 s^{-1} compared to 240 Pa.s for the S32-58 ink. This is attributed to decreased particle size and particle size distribution. All inks exhibit shear thinning behavior, indicated by a decrease in viscosity with increasing shear rate.

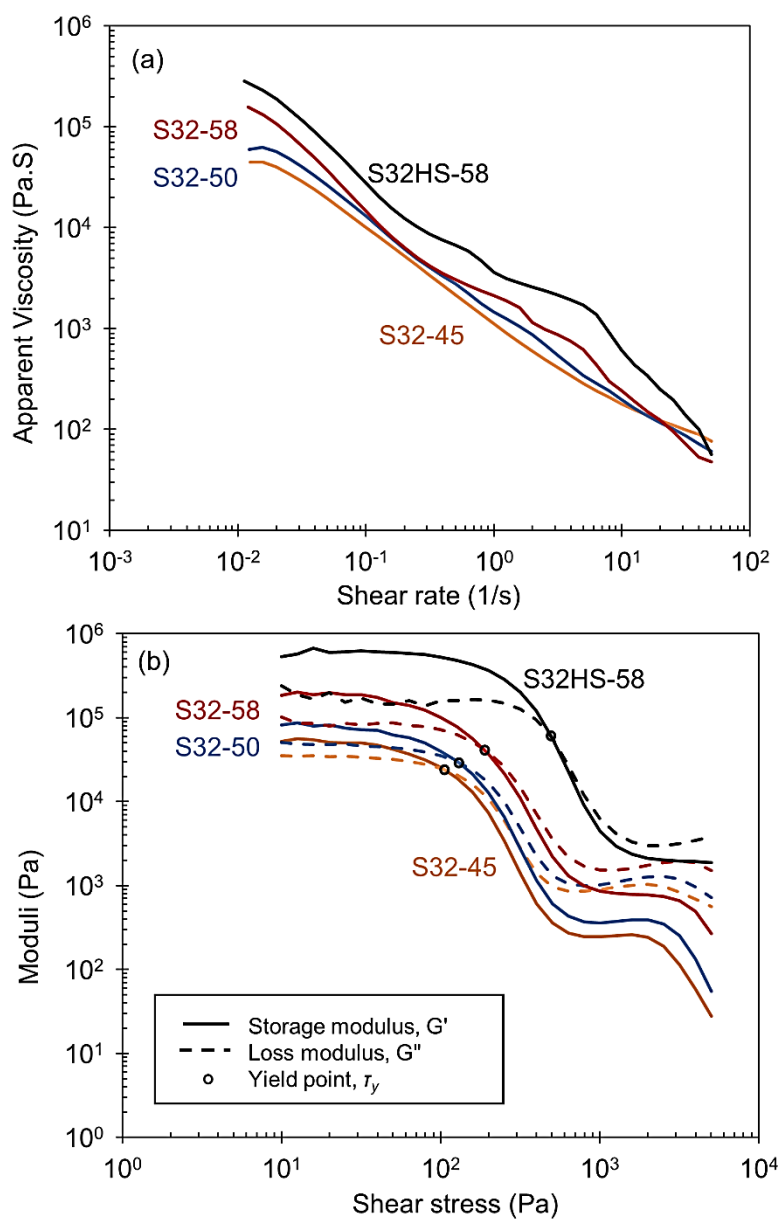


Figure 3.3. Rheological behavior of formulated foam inks. Log-log plots of (a) apparent viscosity vs shear rate and (b) storage and loss moduli vs oscillatory shear stress for foam inks with varied volume fractions of GMBs (45,50, and 58vol. %).

Quantification of shear thinning behavior is determined by fitting curves (**Figure 3.3a**) to the power law model:

$$\eta = K\dot{\gamma}^{n-1} \quad (3.1)$$

where η is the viscosity, K is the consistency index, and $\dot{\gamma}$ is the shear rate. The shear-thinning index, n , describes the degree of shear thinning, with a higher degree of shear thinning corresponding to smaller n ; for shear thinning fluids, $n < 1$, for shear thickening fluids, $n > 1$, and for Newtonian fluids, where viscosity is independent of shear rate, $n = 1$ [59, 89]. Values for n and K were computed by linear regression over the measured shear rate range (0.01 to 50 s⁻¹) and shown in **Table 3.2**. K values show a direct relationship n an indirect relationship with GMB loading. All formulations exhibit shear thinning index values less than 0.16, reaching similar minimum values of 0.06 and 0.08 for S32-58 and S32HS-58 inks, respectively. These low n values indicate significant shear thinning behavior which is advantageous in reducing the pressure required for material extrusion

Plots of the storage (G') and loss moduli (G'') versus shear stress are shown in **Figure 3.3b**. An increase in GMB volume loading increases both G' and G'' , with S32HS-58 ink exhibiting the largest G' of $\sim 6 \times 10^5$ Pa. For all inks, G' dominates at low shear stresses, resulting in elastic behavior but as the applied stress increases, G' decreases to values below G'' , indicating the ink has yielded and flowed, exhibiting viscous behavior. The yield stress (τ_y), the point of transition from elastic to viscous behavior, is determined by the intersection of G' and G'' [90].

Table 3.2. Rheological properties of foam inks.

Ink (GMB-vol.%)	n	K (Pa.s ⁿ)	τ_y (Pa)
S32-45	0.16	1340	110
S32-50	0.11	1600	134
S32-58	0.06	2030	196
S32HS-58	0.08	4140	501

Reported in **Table 3.2**, τ_y values increase with increasing GMB loading, from a minimum of 100 Pa for S32-45 to a maximum of 500 Pa for S32HS-58. Foam inks exhibit adequate G' values and high yield stress values, needed to enable extrusion and shape retention in the printed part. Overall, all foam inks display prominent shear thinning and viscoelastic behavior needed for successful DIW printing.

3.4.3 Foam Sample Printing

In-line pressure measurements were taken as rectangular foam samples were successfully printed with all foam inks, utilizing straight nozzles with diameters of 660 and 966 μm . Volumetric pumps enabled all inks to be consistently extruded out of all nozzles, including inks with maximum loading (S32-58 and S32HS-58) out of the smallest nozzle (660 μm) (**Figure 3.4a**). In **Figure 3.4b**, a slight visual difference is seen, in which samples become lighter in color with larger volume fractions of GMBs. Sufficient print quality was achieved with all inks but as GMB loading and yield stress decreased, shape and feature retention also decreased. The S32-45 sample displays a smooth and shiny surface, in which filaments prominently coalesce, compared to the S32-58 sample where surface filament features are well defined.

3.4.4 Extrusion Pressure Measurements

In the current DIW setup (**Figure 3.2**), inks pass through two separate zones where GMB fracture can occur: i) the volumetric pump, in which inks fill submillimeter diameter cavities formed by a rotor and stator, that translate along as the rotor rotates and ii) the deposition nozzle, where inks, driven by flow from the pump outlet, are extruded

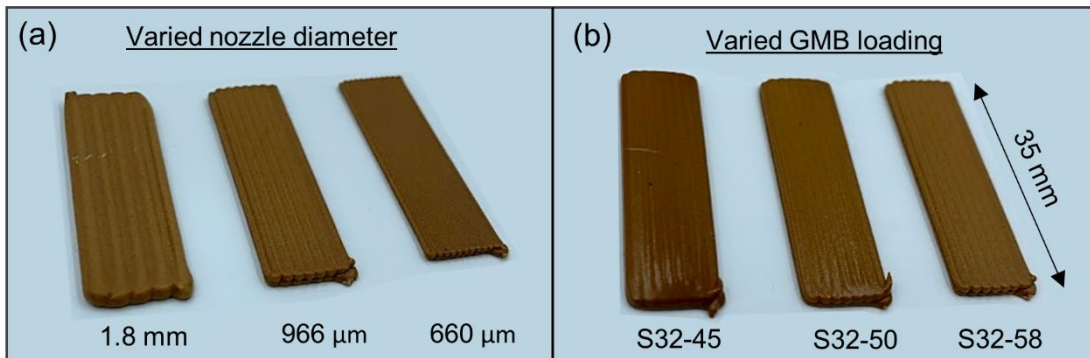


Figure 3.4. Printed foam samples for density and pressure measurements. a) S32-58 samples printed out of the pressure sensor alone (1.8 mm) and with 966- and 660μm-diameter-nozzle tips. b) Samples with 45,50, and 58 vol. % S32 GMBs printed out of a 966 μm-diameter-nozzle. Note: S32HS-58 samples are not pictured but exhibit similar print characteristics as S32-58 samples.

through a circular orifice of small diameter (<1mm) [91]. Pressure within the pump cannot be measured in the current setup, however, placement of the inline pressure sensor between the pump outlet and nozzle inlet allows measurement of the required extrusion pressure and GMB fracture behavior in the nozzle tip.

Experimentally measured pressure profiles (**Figure 3.5a**) reveal two characteristic pressure regions: i) a peak start pressure required to initiate flow and ii) a steady state pressure (SSP) when steady flow is achieved. The latter is used for further comparison. All inks permitted consistent extrusion, indicated by a level SSP plateau, but on rare occasion (3 occurrences out of 100 samples), a jamming or clogging event occurred in the nozzle, resulting in an abrupt pressure jump as seen in **Figure 3.5b**. If flow through the nozzle ceases, ink continues to flow out of the pump, increasing nozzle pressure until the jam is broken and flow resumes. In contrast, a drop in pressure indicates ceasing of ink flow out of the pump but this was not observed during any prints. Aside from providing insight into process mechanisms, real-time in-line pressure measuring is beneficial for monitoring extrusion/print status and process control [92].

All foam inks exhibit similar behavior, where an increase in GMB loading and viscosity increases SSP. For example, pressure profiles of inks printed with the largest 966 μm -diameter-nozzle at a flowrate of 400 $\mu\text{L}/\text{min}$ are shown in **Figure 3.6a**, revealing an increase in average SSP from 0.5, 0.68, 1.17, and 1.28 MPa for S32-45, S32-50, S32-58, and S32HS-58 samples, respectively. Additionally, increasing flowrate also increases SSP, as seen in **Figure 3.6b**, where doubling of the flowrate increases SSP by 30% for S32-58 inks (966 μm nozzle). Pressure undulations are noticeable and attributed to pulses

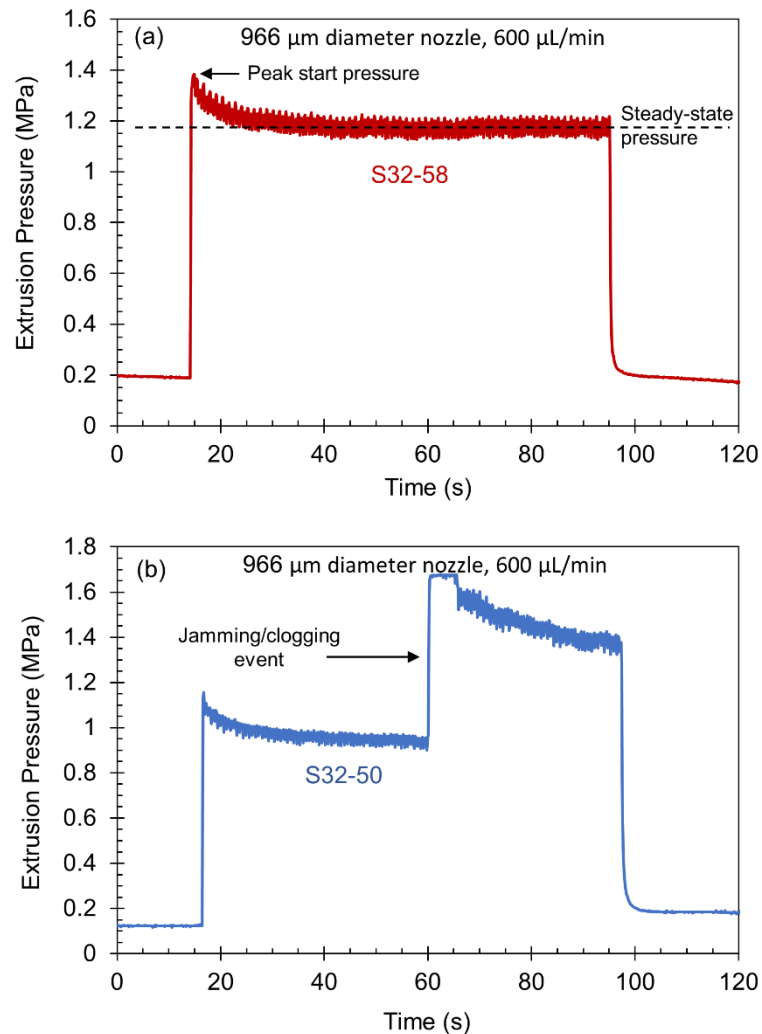


Figure 3.5. Example of characteristic extrusion pressure profiles. a) A normal pressure profile, exhibiting a peak start pressure followed by a steady-state pressure during steady flow. b) A pressure spike from a jamming event in the nozzle. Jamming events were rarely seen but demonstrates how inline pressure measurements are beneficial for on-the-fly monitoring of extrusion status.

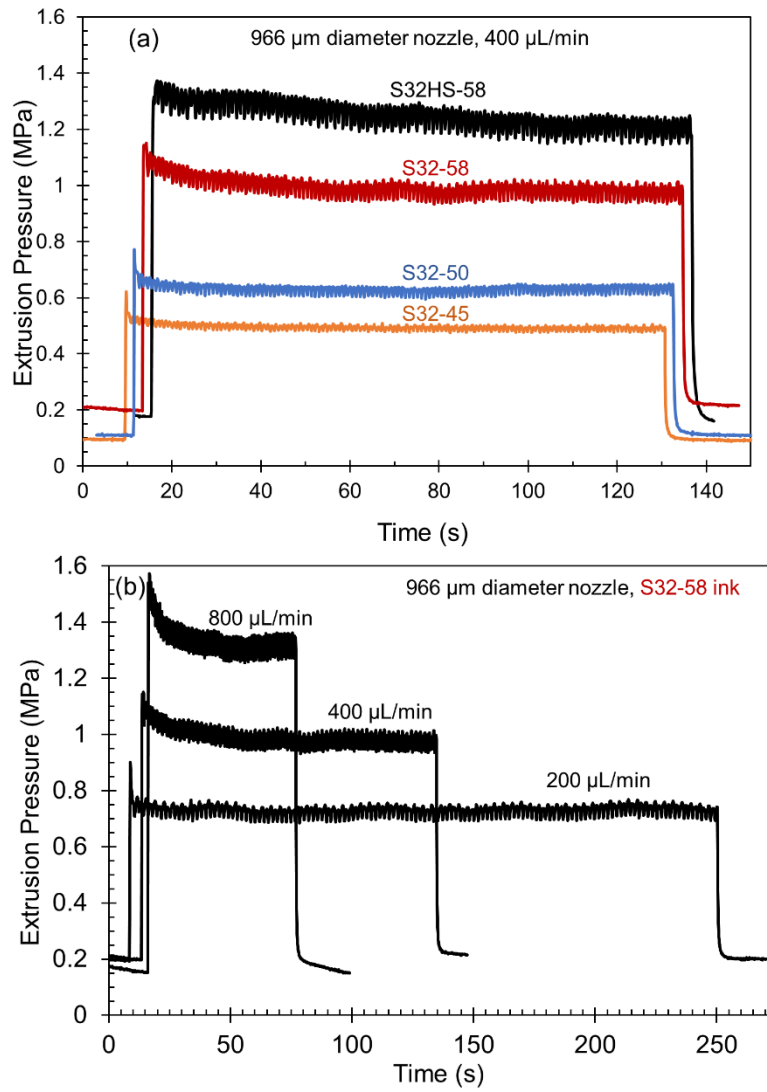


Figure 3.6. Varied GMB loading and flowrate pressure profiles. a) Pressure measurements displaying an increase in pressure with increased GMB vol loading b) Increased flowrates lead to increased pressure values.

in flow caused by rotations of the rotor. Faster rotor rotation needed for higher flowrates results in more tightly packed undulations.

For complete assessment of loading and flowrate effects, measured SSP values are plotted over the entire flowrate range in **Figure 3.7**. Samples printed with no nozzle tip, directly out of the pressure sensor (1.8 mm diameter), exhibited low SSP values (0.08-0.2 MPa) and a weak, direct relationship with flowrate. Only a few data points could be obtained for samples printed with the 660 μm nozzle (data not shown) due to measured pressures exceeding the ~ 1.65 MPa pressure limit of the sensor. S32-45 and S32-50 samples displayed SSPs of 0.95 and 1.4 MPa, and 1.1 and 1.5 MPa at 200 and 400 $\mu\text{L}/\text{mm}$, respectively. 966 μm nozzle SSPs values all exhibited a strong linear relationship with flowrate where S32HS-58 displayed the largest slope (0.0016), followed by S32-58 (0.0009), and similar values for S32-50 and S32-45 (0.0005). The observed linear trends enable simple prediction of SSP for each GMB loading, guiding optimization of flowrate when extrusion equipment limitations are present [8].

Utilizing pressure-driven flow models, extrusion pressure in the nozzle can be estimated with the Hagen-Poiseuille (HP) equation, given by:

$$P = \frac{8 \eta Q L}{\pi R^4} \quad (3.2)$$

where P is the extrusion pressure, Q is the volumetric flowrate, R is the nozzle radius, L is the nozzle length, and η is the viscosity [8, 59, 89]. Viscosity is calculated with the power law model (Equation 3.1), utilizing K and n values measured with parallel plate rheology.

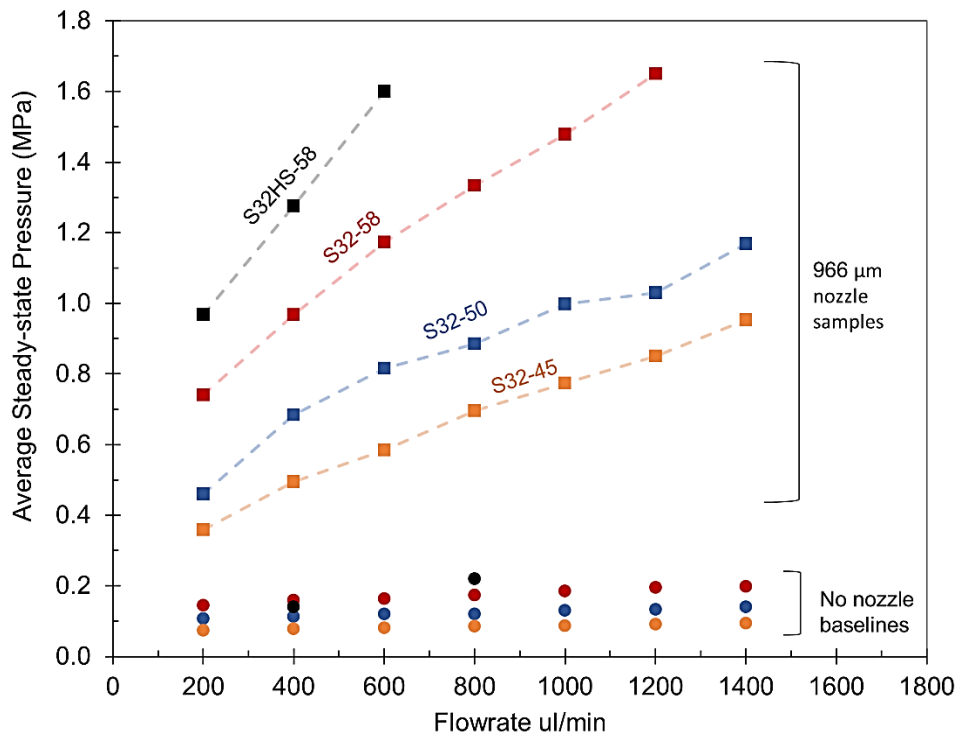


Figure 3.7. Average steady-state pressure measurements versus flowrate.

Shear thinning behavior of the inks is accounted for with the Rabinowitsch correction, allowing calculation of the true shear rate ($\dot{\gamma}$) at various flowrates following:

$$\dot{\gamma} = \frac{4Q}{\pi R^3} \left(\frac{3n+1}{4n} \right) \quad (3.3)$$

Model values, reported in the Appendix section “Pressure-driven flow model for foam inks” (**Table A3.1** and **Figure A3.1**), were substantially lower than experimental values, with the difference increasing as GMB loading and flowrate increased. Variance is attributed to factors such as nozzle geometry and effects of the large volume loading of GMB fillers, displaying limitations in application to loaded (fillers) polymers that exhibit low shear thinning index values (<0.2), but further investigation in model correction or adaptation is beyond the scope of this work.

3.4.5 Density Characterization

In order to determine optimized extrusion parameters that minimize GMB breakage, a density evaluation was conducted. Baseline samples that were collected and cured from as-mixed inks, prior to extrusion, and cured displayed measured densities that matched calculated theoretical densities of 0.79, 0.76, and 0.69 g/cc for inks loaded with 0.45, 0.50, and 0.58 volume fraction GMBs respectively, indicating GMB failure does not occur during the mixing process. To decouple pump and nozzle effects, samples were printed with no nozzle tip (**Figure 3.8a**). In all S32 GMB samples, GMB failure consistently occurs during passage through the pumps, shown as densities increased from baseline to printed samples, with S32-58 samples displaying the largest increase (0.69 to 0.74 g/cc, +9%). Across the flowrate range, S32-45 and S32-50 densities were similar (< 1% density increase) whereas increasing S32 GMB loading to 58 vol.% (S32-58)

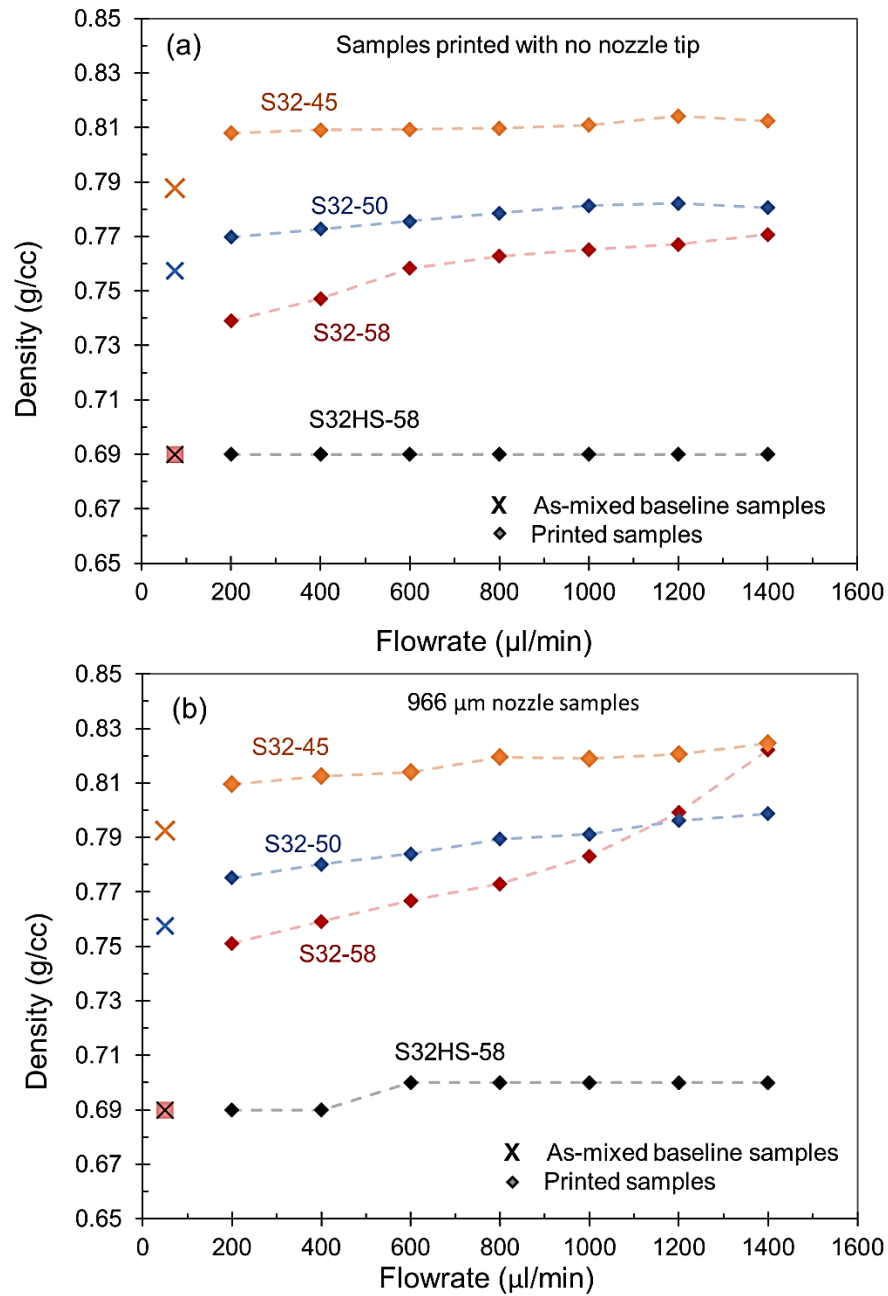


Figure 3.8. Density versus flowrate plots. a) Samples printed with no tip, directly out of pressure sensor and b) samples printed with a 960 µm-diameter-nozzle.

produced a slight increase (0.74-0.77 g/cc) with increasing flowrate. In contrast, utilization of S32HS GMBs, even at a 58 vol.% loading, facilitates near complete GMB survival, displaying flowrate independent densities of 0.69 g/cc matching baseline values.

Initially, printing with the largest nozzle (966 μm -diameter) was explored (**Figure 3.8b**). At low loadings, S32-45 and S32-50 samples exhibited no significant flowrate dependence (<3% increase), whereas S32-58 foam displayed a direct trend, revealing density increase (0.75-0.82 g/cc) over the flowrate range, and a density spike from 800-1400 $\mu\text{L}/\text{min}$. When specifically utilizing the large nozzle and S32 GMBs, the maximum loading of 58 vol. % remains the best candidate for achieving the lowest density, especially prior to the density spike, at flowrates normally employed during printing (<1000 $\mu\text{L}/\text{min}$). S32HS samples remain superior however, exhibiting no significant GMB failure from passage through the nozzle tip, indicated by densities that remain similar to theoretical over the entire flowrate range.

Extrusion through 660 μm -diameter nozzle was also studied as it comprises the core nozzle in the core-shell nozzle. The decrease in nozzle size had a noticeable effect (**Figure 3.9a**), as S32 samples exhibited an increase in density with increasing flowrate, all approaching similar density at high flowrates of 1200-1400 $\mu\text{L}/\text{min}$. S32-45 and S32-50 densities displayed linear trends, compared to S32-58 which displayed a similar density spike as observed with the large nozzle, albeit at a lower flowrate (200 $\mu\text{L}/\text{min}$). It is hypothesized the observed density spike indicates the onset of jamming events in the nozzle, occurring at lower flowrates as nozzle area is decreased. Also noteworthy, when utilizing the smaller nozzle with S32 GMBs, S32-50 foams display lower densities than S32-58, illustrating lower density can be achieved by lowering GMB loading.

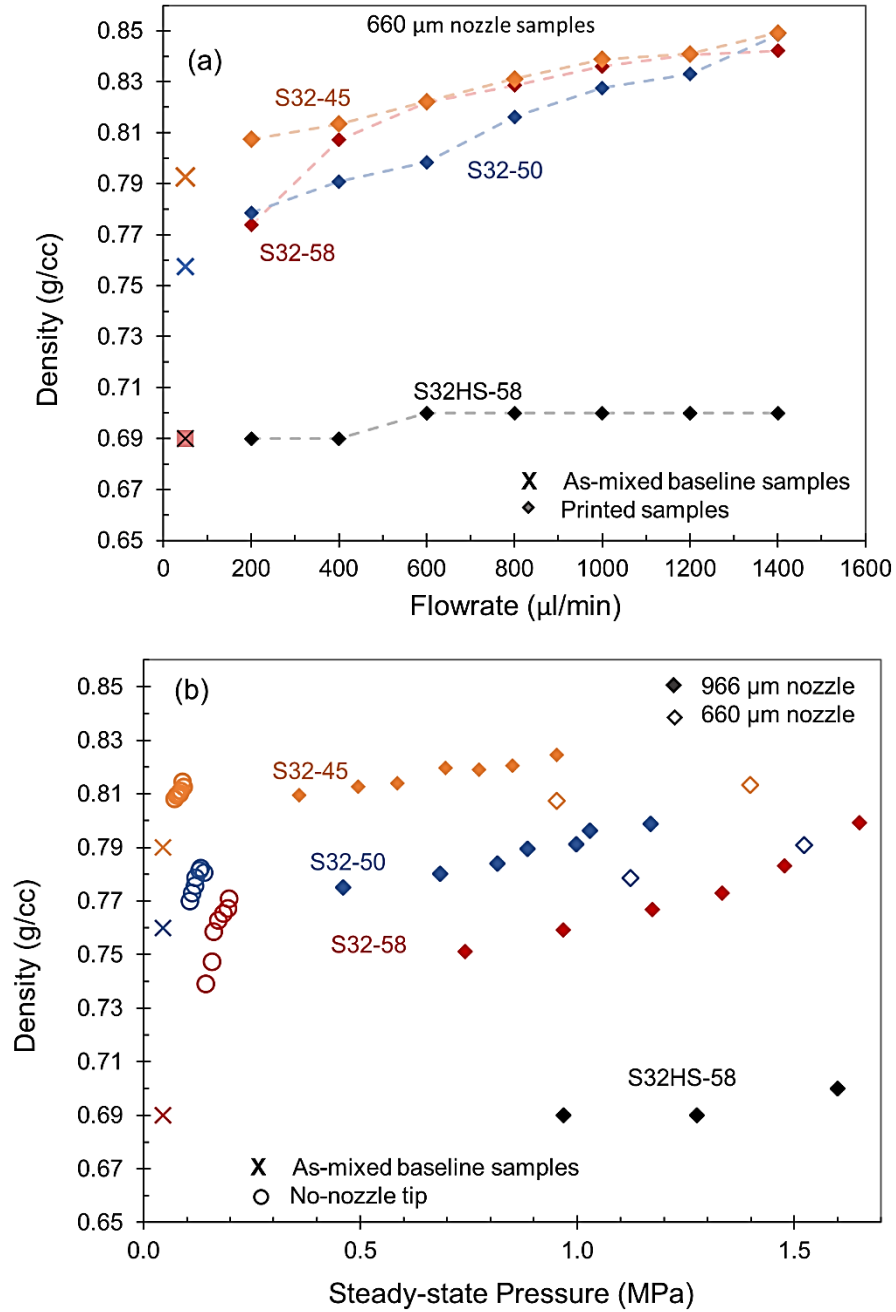


Figure 3.9. Density versus flowrate and density versus steady-state pressure plots. a) Density versus flowrate for 660 μm-diameter-nozzle samples. b) Density vs steady-state pressure for all nozzles.

Improved performance with decreased consumption of GMBs is of significance when material cost, usage, and availability are important factors. Nonetheless, S32HS foam remains superior overall, maintaining near theoretical density across all flowrates.

Density versus measured SSP is plotted in **Figure 3.9b**, allowing for further comparison. S32 inks printed absent of a nozzle tip, at low pressures (0.1-0.2 MPa), exhibit prominent density increase. Further, S32 GMBs exhibit substantially higher crush strengths (13.8 MPa) than measured SSP, indicating S32 GMB failure is unlikely a result of SSP experienced in the nozzle. S32HS foam density is independent of SSP, experiencing the highest pressure while maintaining a constant low density.

To summarize, fracture of S32 GMBs predominantly occurs during passage through the volumetric pumps and is dependent upon flowrate. At higher flowrates and higher volume loadings, further fracture occurs from GMB impacts and shear within in the nozzle. Pertinent to C-S printing, if S32 GMBs are used in future work, decreasing loading to 50 vol.% provides a foam with the lowest density after printing. Extrusion pressure required for polymer flow through the nozzle was successfully measured but is not a direct indicator of S32 GMB survival. In situations where extrusion route and GMB type cannot be changed, optimizing the processing parameters of flowrate, GMB loading, and nozzle diameter can provide noticeable improvement. However, altering of GMB type, specifically to S32HS GMBs, proved considerably more effective in eliminating GMB fracture and achieving near theoretical printed density. This is attributed to a decreased average size, smaller size distribution, and increased strength, enabling S32HS GMBs to remain unaffected by small nozzle diameters and flowrates used in this study.

Proving superior to S32 foams by negating detrimental processing effects and displaying the lowest printed density, S32HS foam was utilized for further foam printing and study.

3.4.6 S32HS Mechanical Performance

With the ability to print foam structures at near theoretical density, S32HS-58 ink was utilized to successfully print flexural and compression samples (**Figure 3.10**) for mechanical characterization. Measured mechanical properties are summarized in **Table 3.3**. Printed foam 3-pt flexure samples displayed a density of 0.69 g/cc, modulus of 3.54 GPa, and strength of 60.8 MPa. Similar properties were observed in S32-58 foam samples printed through the C-S nozzle in previous work (Chapter 2) but C-S samples also displayed a 21% higher density (0.84 g/cc), demonstrating the weight saving improvement the S32HS-58 foam affords. Flexural stress-strain curves are plotted in (**Figure 3.11a**) revealing brittle fracture, characteristic of highly loaded SF foams[75]. During flexure, samples experience both tension and compression. SEM micrographs of the top compression side (top, **Figure 3.11b**) reveal noticeable GMB failure, with minimal pullout, indicating a strong interface between GMB and matrix. On the bottom tensile side (**Figure 3.11b**), GMB failure is still present but a larger number of GMBs remain intact, with visible matrix deformation, and a couple occurrences of GMB pullout visible.

To further investigate foam performance, compression blocks (**Figure 3.12a**) and honeycombs with 7- and 14-mm cell sizes were successfully printed and tested, demonstrating the ability to fabricate complex foam geometries utilizing DIW and increase weight reduction (**Figure 3.10b**). Compression blocks were machined on all

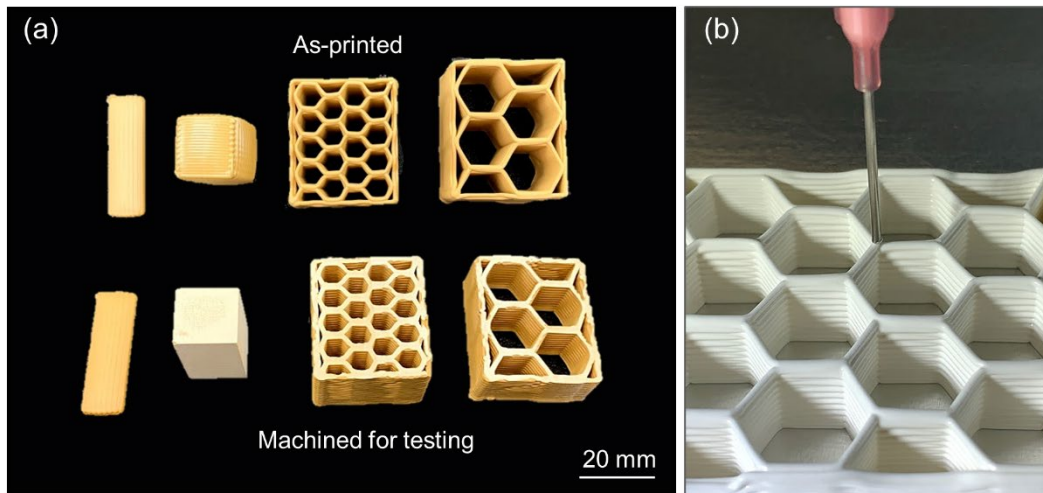


Figure 3.10. Printed S32HS foam samples for mechanical testing. a) Rectangular flexural samples, compression blocks, and honeycombs both as-printed and machined for testing. b) DIW printing of honeycombs demonstrating ability to fabricate complex foam geometries.

Table 3.3. Mechanical properties of S32HS foams

Sample	Test	Modulus (GPa)	Strength (MPa)	Density (g/cc)	Relative Density
Rectangular	Flexural	3.54 ± 0.08	60.80 ± 3.07	0.69	---
Blocks	Compression	4.94 ± 1.24	100.1 ± 5.81	0.69	---
7mm honeycomb	Compression	2.04 ± 0.19	41.59 ± 2.12	0.37	0.53
14mm honeycomb	Compression	1.25 ± 0.21	23.86 ± 2.40	0.21	0.36

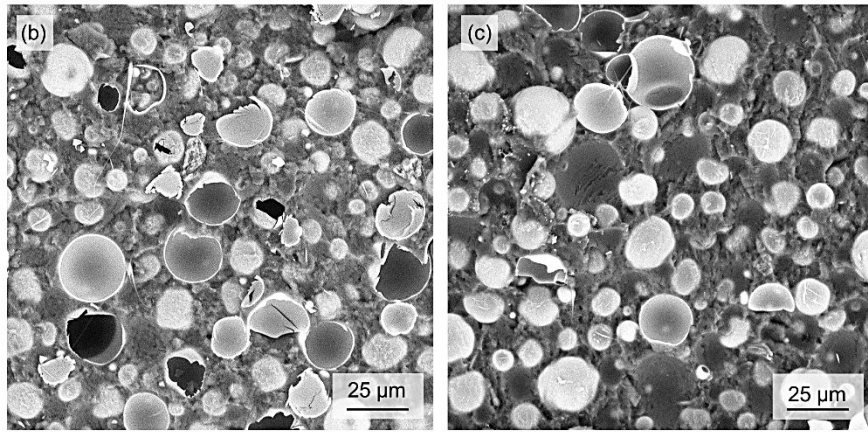
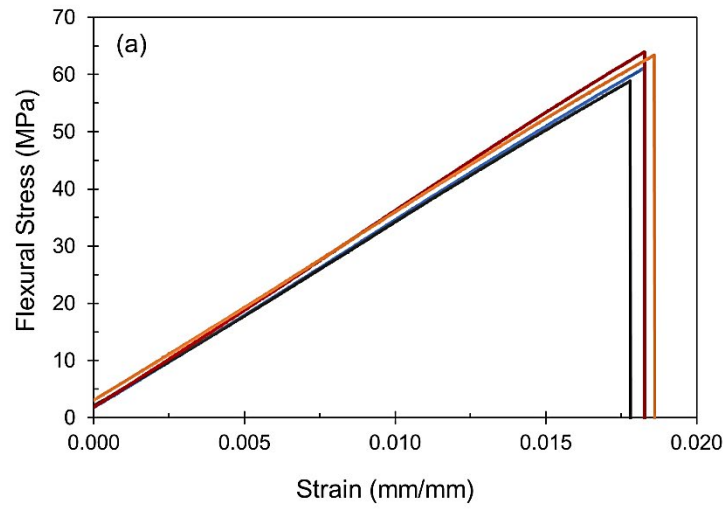


Figure 3.11. Flexural stress-stain curve a) and fracture surfaces. SEM micrographs of b) compression and c) tension side of sample.

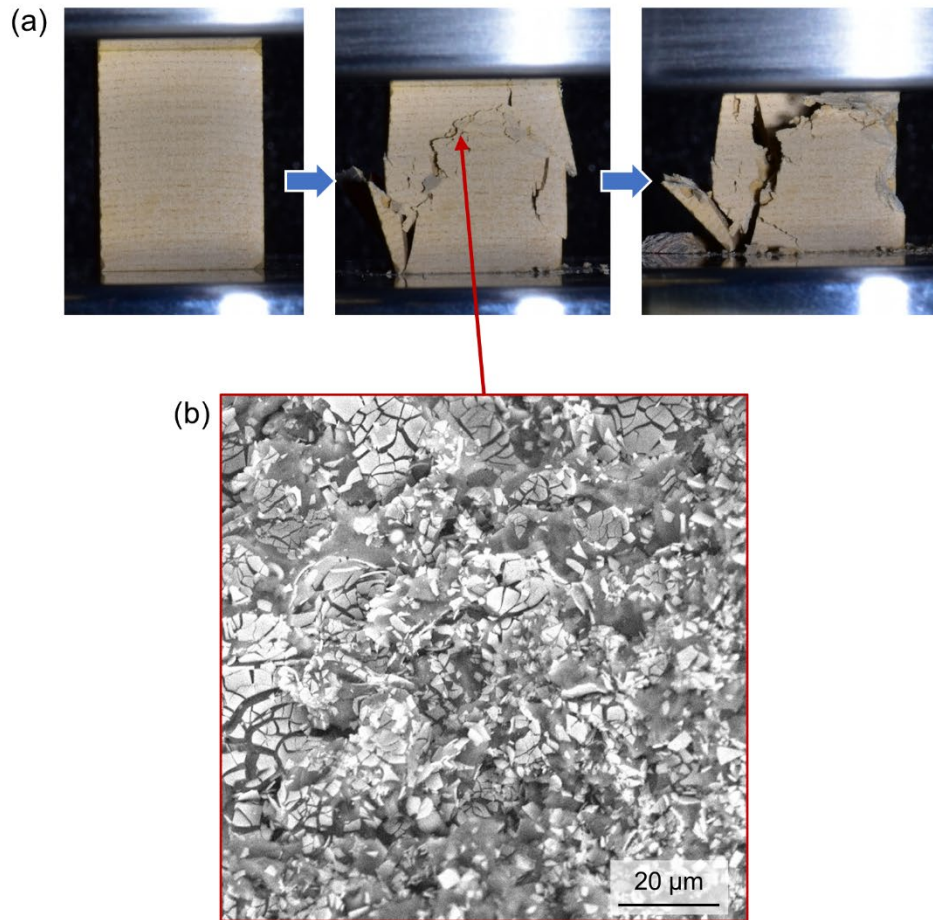


Figure 3.12. S32HS foam compression testing. a) Compression blocks during testing and b) SEM micrograph of failure surface showing complete GMB crushing.

sides prior to testing while honeycombs were only machined on the top and bottom surface to provide parallel faces (**Figure 3.10a**). Foam honeycombs are commonly used as core materials in sandwich panels, thus honeycomb samples were tested in a flatwise orientation to measure out of plane compression properties [93]. SEM micrographs of compression block failure surfaces reveal complete crushing of GMBs (**Figure 3.12b**). Modulus and strength values are plotted in **Figure 3.13a** and **3.13b**, with bulk samples displaying the highest modulus (4.94 GPa) and strength (23.9 MPa) at a density of 0.69 g/cc. Honeycomb samples display a linear decrease in modulus and strength with relative density. These properties follow established scaling laws for out of plane properties of honeycombs undergoing fracture, given by:

$$\frac{E}{E_s} = \frac{\rho}{\rho_s} \quad (3.4)$$

and

$$\frac{\sigma}{\sigma_s} = \frac{\rho}{\rho_s} \quad (3.5)$$

where E_s , σ_s , and ρ_s are the compressive modulus, compressive strength, and density of the solid foam material, respectively, and E , σ , and ρ are the measured properties of the honeycomb samples [93, 94]. Utilizing properties from compression blocks for calculation, predicted modulus values **Figure 3.14a** are in good agreement with experimental data. In contrast, predicted strength values **Figure 3.14b** are slightly higher than experimental, attributed to possible print defects such as inadequate filament stacking and wavy walls. Data for honeycomb samples displayed small scatter, indicating S32HS foam enabled consistent printing of honeycomb geometries.

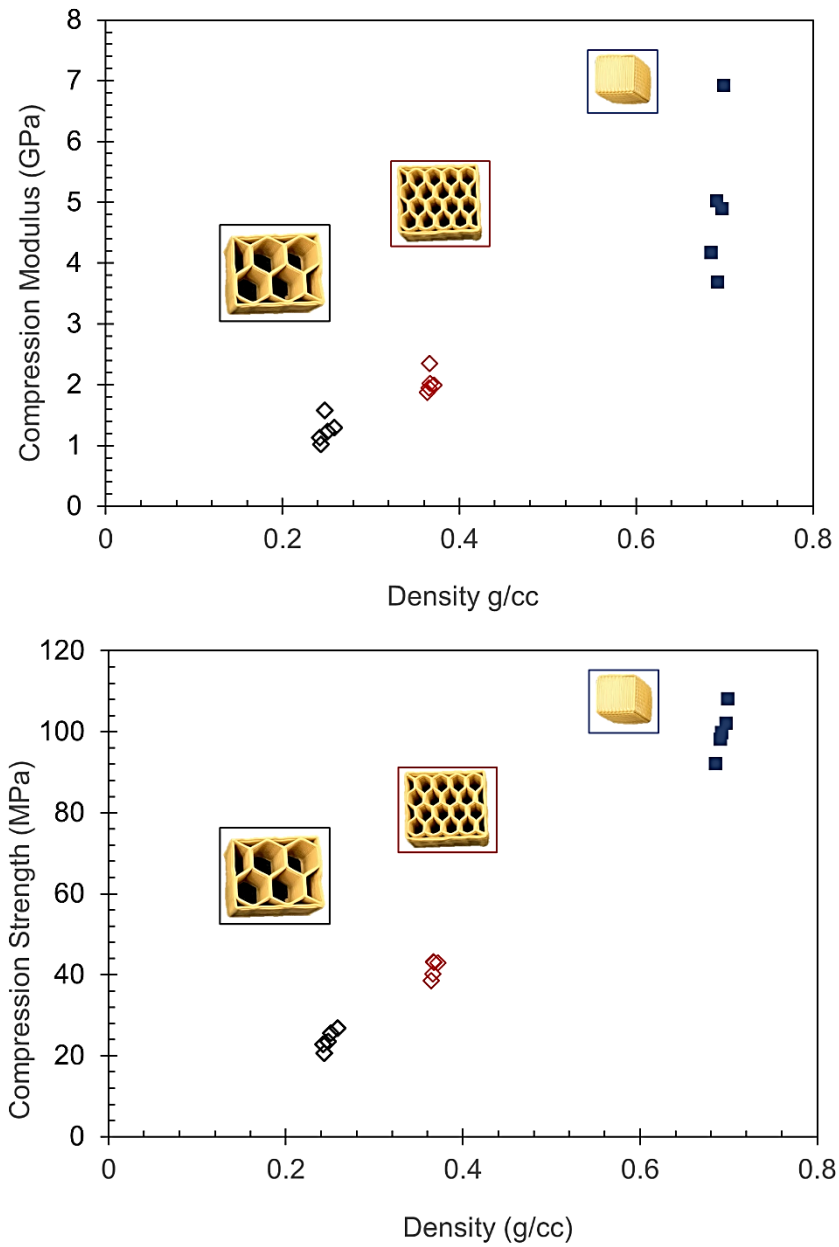


Figure 3.13. Compression modulus and strength of S32HS foam. a) Modulus and b) strength with representative sample geometries of 100, 53, and 36% relative density.

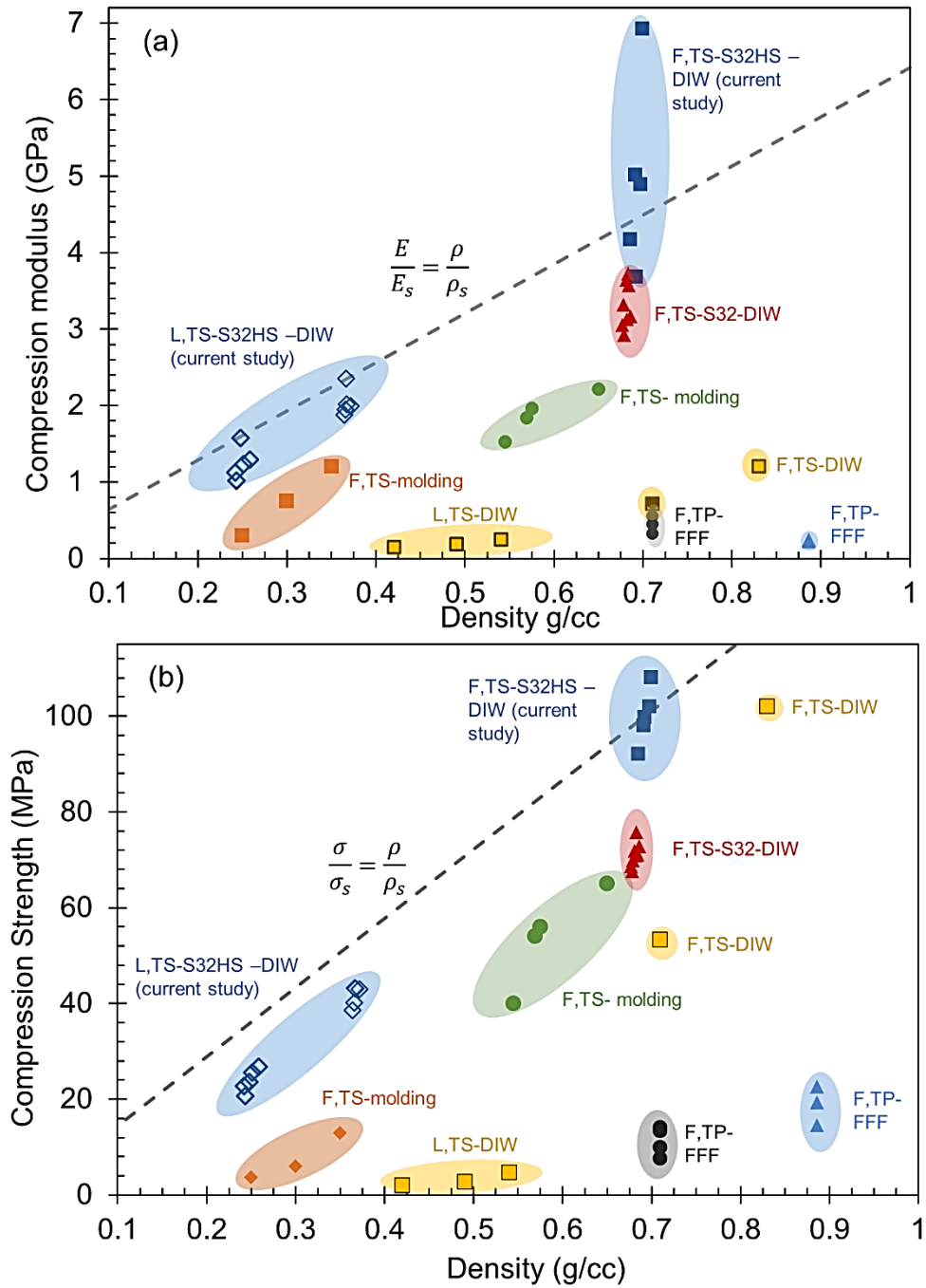


Figure 3.14. Property space map of compression properties. a) Modulus versus density and b) Strength versus density. Analytical predictions are displayed as dashed lines calculated using properties of the S32HS foam blocks. Labels indicate foam geometry, whether solid foam (F) or lattice structure (L), matrix polymer, whether thermoset (TS) or thermoplastic (TP), and processing route.

To compare the mechanical performance of the printed foam structures, experimental data is plotted along with literature and previous S32 foam sample values (Chapter 2) in **Figure 3.14a** and **3.14b**. Labels indicate foam geometry, whether solid foam (F) or lattice structure (L), type of polymer matrix, either thermoset (TS) or thermoplastic (TP), and process type (DIW, FFF, or molding). S32HS printed foam (F,TS-S32HS-DIW) exhibits modulus and strength values ~2x times higher than previous printed S32 foam (F,TS-S32-DIW) and molded two-phase GMB thermoset foams (F,TS-molded, [60]), 2-5x higher than current DIW printed foams (F,TS-DIW, [80]), and up to 5x times higher than GMB thermoplastic FFF printed foams (F, TP-FFF, [76, 77]). S32HS honeycomb structures, enabling achievement of lower densities by tailor the geometry, also showed 2-5x higher strength and modulus values over molded 3-phase thermoset foams (F,TS-molded, [24]) and current DIW printed lattices in literature (L,TS-DIW, [80]). Overall, DIW printing of S32HS foam enables fabrication of high-performance foam structures that exhibit superior properties to other current foams.

3.4.7 Application of S32HS-58 Foam to Core-shell Architecture

Previous core-shell prints were hindered by the inability to achieve an optimal low-density foam core. To investigate improvement afforded by the new S32HS foam, flexural samples were printed with 0.40, 0.44, 0.53, and 0.61 core volume fractions and tested under 3-pt bending. Optical micrographs of C-S cross-sections (**Figure 3.15**) show minimal defects and low core eccentricity, indicating the S32HS foam enables successful C-S printing. Flexural properties of C-S samples are reported in **Table 3.4** while **Figure 3.16** displays $E^{1/3}/\rho$, the material index utilized for quantification of performance for



Figure 3.15. Optical micrographs of C-S cross-sections printed with S32HS foam.

Table 3.4. Flexural properties of core-shell samples with S32HS foam.

Core Volume Fraction	Density (g/cc)	Modulus, E (GPa)	Strength, σ (MPa)	Index, $E^{1/3}/\rho$
0.40	1.13	16.4 ± 1.6	90.5 ± 11.9	2.25 ± 0.07
0.44	1.10	18.7 ± 0.5	99.2 ± 3.0	2.41 ± 0.03
0.53	1.04	17.2 ± 1.1	94.6 ± 2.6	2.49 ± 0.05
0.61	0.98	14.6 ± 0.6	86.3 ± 3.4	2.50 ± 0.05

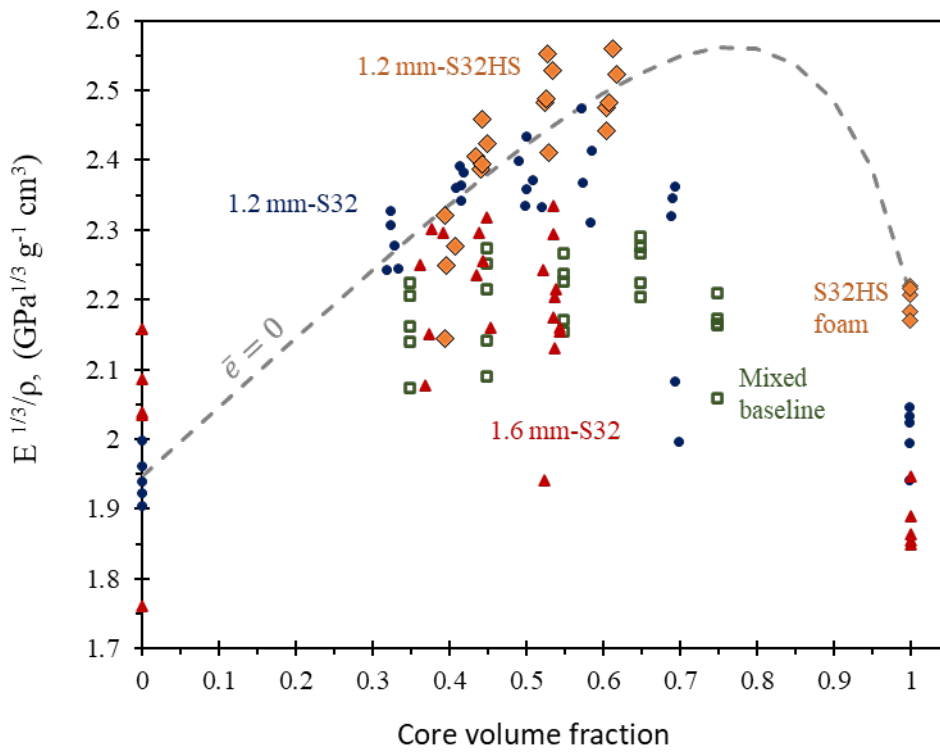


Figure 3.16. $E^{1/3}/\rho$ versus measured core volume fraction. Core-shell samples printed with the new S32HS foam exhibit significantly higher index values than previous samples.

light, stiff panels, plotted versus core volume fraction. Implementation of the S32HS foam C-S samples produces similar modulus and strength values as previous S32 C-S samples, however at 20% lower densities. The decrease in density enables an index increase up to 5% over S32 foam samples, and ~30% compared to constituent CF samples. As V_f increases up to ~0.6, $E^{1/3}/\rho$ also increases, reaching a maximum average value of $2.50 \text{ GPa}^{1/3} \text{ g}^{-1} \text{ cm}^3$ and a maximum single measured value of $2.56 \text{ GPa}^{1/3} \text{ g}^{-1} \text{ cm}^3$. Analytical predictions ($\bar{\epsilon} = 0$) are also plotted, showing good agreement with experimental values for the S32HS foam.

3.5 Conclusions

The initial part of this study explored multiple aspects of syntactic foam DIW printing, beginning with initial investigation into ink rheology, extrusion pressure, nozzle diameter, and GMB loading to gain understanding of the mechanisms involved in GMB failure during extrusion and attempt to optimize processing parameters to achieve a lower density foam than printed in previous work. In the second half of the work, a new S32HS foam, proven effective in resisting GMB failure during printing, is used to fabricate flexural and compression samples that were stronger and stiffer than conventional SFs and current DIW printed foams. Honeycomb samples were also successfully printed, exploiting AM's unique ability to produce complex geometries. A summary of findings is presented below:

- In-line nozzle pressure measurements provided real-time monitoring of extrusion status.

- S32 GMB failure was determined to predominantly occur during passage through volumetric pumps.
- Maximum loading of 58% S32 GMB, resulted in the presence of a density spike, which moves to higher flowrates with decreased nozzle diameter, thought to be caused by the onset of sphere jamming.
- Specifically related to C-S nozzle application, decreasing S32 GMB loading to 50 vol.% results in the lowest printed density at moderate flowrates (300-1000 $\mu\text{L}/\text{min}$).
- Utilization of S32HS GMBs, which exhibit decreased average diameter and increased strength compared to S32 GMBs, produced a foam unaffected by DIW processing, resulting in a 18% decrease in printed density (0.69 g/cc).
- Superior specific flexural and compressive properties were displayed in structures fabricated with the new S32HS foam. Printed structures showed up to 5x higher compressive strength and modulus values compared to foams produced through conventional routes, fused filament fabrication, and DIW printing.
- Implementation of the S32HS into the C-S architecture resulted in a 5% increase in index value over previous samples, and even larger 30% increase over constituent CF index values.

4. MULTIMATERIAL HYBRID ADDITIVE MANUFACTURING ENABLED BY CORE-SHELL NOZZLE

4.1 Abstract

Multimaterial components often exhibit enhanced properties over single material systems, yet, processing of such structures can be challenging. Material extrusion additive manufacturing offers a potential route to fabricate complex multimaterial structures but is limited by the need to use two nozzles. In the first two chapters, the capability to print both core-shell architectures and hybrid lattice structures with our new C-S nozzle was demonstrated. In this work we further expand the capability of C-S printing, by demonstrating multimaterial 3D printing using the core-shell nozzle which enables “on-the-fly” switching between materials during fabrication, without the need for two nozzles. Material transition behavior is analyzed, enabling accurate determination of transition lengths, which are needed for print path and component design. Multimaterial components are successfully fabricated with both silicone and filled epoxy inks (CF and foam). Finally, flexural tests reveal increased properties in C-S printed samples compared to those printed with two nozzles, attributed to benefits of a continuous print path, more efficient use of CFs, and a gradual, graded transition between materials. Overall, our new approach enables material switching with a continuous print path, providing greater design flexibility and compositional control, opening new routes to DIW print multimaterial architectures.

4.2 Introduction

As current research continues to push the boundary of material performance, properties attainable with single materials become limited. One approach to achieve further improvement involves the incorporation of multiple materials and manipulation of

architecture to produce hybrid materials, described as “a combination of materials or material and space in configurations and connectivities that offer enhanced performance”[6]. As multiple materials are added to fabrication, the complexity of manufacturing increases, eclipsing the capability of some traditional processes. In order to fabricate components with multiple materials via traditional routes, various component parts are commonly fabricated and joined to each other, whether it be by adhesive, welding, fastening, etc., introducing unwanted additional weight, material, manufacturing steps, and weak points [75].

Material extrusion additive manufacturing, specifically direct ink write (DIW), provides a promising route to fabricate hybrid multimaterial architectures, where components are built in a layer-by-layer fashion by the direct deposition of viscoelastic feedstock materials[19, 47, 95]. DIW affords a large material selection, as feedstock inks can be formulated for metal[16, 18, 96] and ceramic printing [14, 15], along with a variety of filled thermoset composites [10, 19, 22]. Conducive to multimaterial fabrication, DIW printing is commonly performed at ambient temperatures, employing a curing step post printing which provides stronger bonding between filaments compared to routes such as fused filament fabrication (FFF). Currently, DIW has been utilized to successfully fabricate multimaterial architectures, both on a filament scale with core-shell printing [37, 41, 51], and larger component scale by depositing two separate materials[97, 98].

Multimaterial 3D printing is commonly achieved by extruding each individual material out of separate nozzles. The deposition of one material at a time utilizing multiple nozzles imposes multiple challenges and limitations, including: i) the offset between

nozzles must be correctly calculated and accounted for in the print path to enable correct alignment between deposited filaments, ii) starting and stopping of ink flow produces print defects if flow is initiated/halted too soon or too late, iii) nozzle clearance can limit the ability to deposit material in tight regions of a part, and iv) the abrupt material transition at the filament interface limits compositional and property control.

In the first two chapters, the capability to print both core-shell architectures and hybrid lattice structures with our new C-S nozzle was demonstrated. To further expand the capability of C-S printing, we demonstrate multimaterial 3D printing using the core-shell nozzle which enables “on-the-fly” switching between materials during fabrication, without the need for two nozzles. This approach enables material switching with a continuous print path, providing greater design flexibility and compositional control, opening up new routes to DIW print multimaterial architectures.

4.3 Materials and Methods

4.3.1 Silicone and Epoxy-based Inks

Silicone inks were initially used to study transition behavior with an unfilled ink. SE1700 (polydimethylsiloxane, DOW Corning) was combined with SE 1700 catalyst in a 10:1 ratio by weight. Transparent silicone was utilized for the shell and blue silicone pigment (Smooth-On) was added to the core ink to modify color and enable differentiation between core and shell inks, allowing optical measurements. Mixing was conducted in a planetary mixer (FlackTek) under vacuum at 1500 rpm for a total of 6 minutes.

To investigate material switching with filled epoxy inks, S32HS and CF reinforced inks were formulated following identical protocols reported in Chapter 2 and 3. Note: loadings of CF and S32HS GMBs were kept at 18 and 58 vol. %, respectively, producing shear thinning inks that exhibit viscosities higher than silicone inks [98].

4.3.2 Core-shell Multimaterial Printing

After mixing, inks were loaded into 10 cc syringes and centrifuged at 3600 RPM for 3.5 minutes. Syringes were then loaded into air pressure adapters (Nordson) to feed progressive cavity volumetric pumps (ViscoTec). The core-shell nozzle presented in Chapter 1 was utilized to print multimaterial samples out of one nozzle. The C-S nozzle utilizes a 660- μm -diameter, 2.54 cm long straight tip for the core. Initial silicone prints were conducted with 1.6-mm and 1.2-mm plastic tapered tips (McMasterCarr) and an additional 1-mm-diameter metal taper tip (Global Precision Dispensing Systems, GPD). All silicone prints were cured at 150°C for 30 minutes and filled epoxy ink prints at 100°C for 24 h, followed by 220°C for 2 h.

All print paths were directed by custom g-code, where transition was induced by turning off and on respective pumps. Due to a delay in flow ceasing and initiation, a 0.1-s pause in machine motion was implemented at the time of material switching.

Investigation of transition length was accomplished by printing single filament transition lines with each nozzle and a demonstration “T” joint part (60 mm x 35 mm x 15 mm) was printed with the 1-mm-diameter GPD tip. Flexural samples (nominally 2.2 mm H x 12.5 mm T x 75 mm L) were printed with filled epoxy inks, utilizing both the C-S nozzle and a two-nozzle approach with the GPD nozzle.

4.3.3 Characterization

Optical microscopy (Keyence) was utilized to image transition lines, cross-sections, and printed samples. Measurements were conducted on micrographs to determine the transition length, transition region, and volume of each material. Archimedes density was performed on CF/foam samples to quantify volume of each material in the printed part. Prior to flexural tests, samples were machined to eliminate print defects inherent with two nozzle printing and provide flat faces. 3-pt bend testing was conducted on an electromechanical load frame (MTS) utilizing a 1-kN load cell, span of 33 mm, and crosshead speed of 0.01 mm/s.

4.4 Results and Discussion.

4.4.1 Nozzle Characterization and Transition Length Prediction

To print two materials simultaneously out of a single nozzle, the C-S nozzle was utilized in conjunction with volumetric pumps. The C-S nozzle consists of a recessed inner core tip (660 μm -diameter), coaxially aligned with a removable tapered shell tip, that enables co-deposition of material. For initial extrusion, core or shell ink flow is initiated, filling the shell tip, providing deposition of chosen material. To switch materials, flow of separate inks is ceased and initiated by turning the pumps off or on. The newly-flowing ink must then force out the remaining material from the nozzle end before deposition of new material occurs, and material transition is achieved.

Transition length is dependent on the ink volume below the core tip, hereafter referred to as nozzle volume V_N , which must be cleared before material switch. This was measured by extruding silicone (blue core, clear shell), removing the shell tip (plastic

tapered tips 1.6 and 1.2-mm-diameter), and curing ink in the tip. Once cured, tips were cut open and silicone plugs evaluated. A representative sample could not be adequately removed from the 1 mm GPD tip and thus measurements were taken directly from a dissected tip. Plastic tapered shell tip dissection (1.6 mm), silicone plug for nozzle volume measurements, and GPD nozzle dissection are shown in **Figure 4.1**.

Tapered nozzles exhibit two characteristic cavity geometries, a truncated cone beginning at the bottom of the core tip, with radius r_1 , tapering down to a radius r_2 at a height of h_1 . A cylindrical cavity exists just prior to the tip end, with radius r_2 and height h_2 . Volume of each section is calculated following:

$$V_{tc} = \frac{1}{3}\pi(r_1^2 + r_1r_2 + r_2^2)h_1 \quad (4.1)$$

And

$$V_c = \pi r^2 h_2 \quad (4.2)$$

where V_{tc} is the volume of the truncated cone cavity and V_c is the volume of the cylindrical section. Summation gives total nozzle volume V_N , subsequently utilized to calculate an estimated transition length TL_{est} based on the assumption that the deposited filament diameter (radius, r_f) matches the nozzle tip diameter where:

$$TL_{est} = \frac{V_N}{\pi r_f^2} \quad (4.3)$$

TL_{est} values of 27 mm, 41 mm, and 6.6 mm were determined for the 1.6-mm, 1.2-mm, and 1-mm tapered tips, respectively.

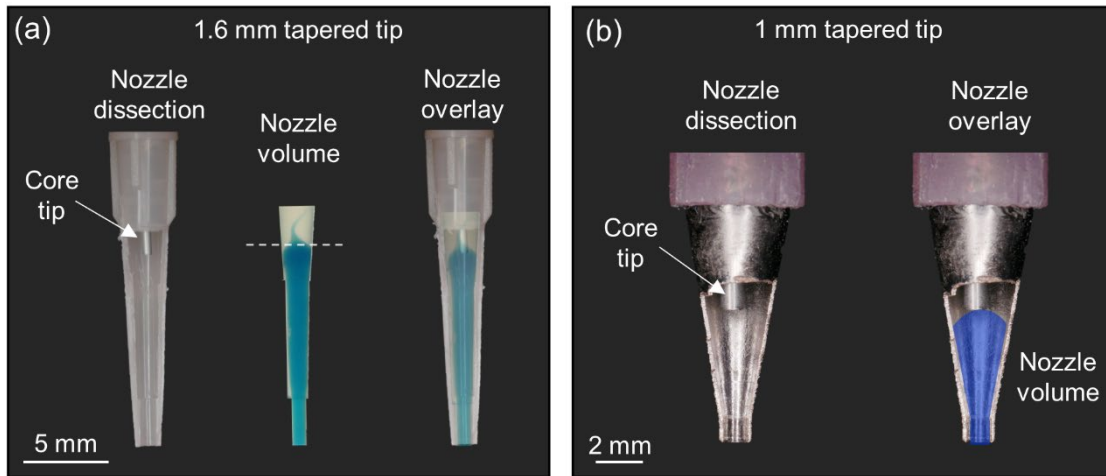


Figure 4.1. Nozzle tip dissection and nozzle volume. a) 1.6-mm-diameter plastic tapered tip. Silicone mold allows direct measurement of nozzle volume. b) 1 mm-diameter GPD nozzle. Estimated nozzle volume shown in blue. Note the GPD exhibits a sharper taper, allowing the core tip to be closer to the tip outlet, producing a smaller nozzle volume of material that must be cleared.

4.4.2 Transition Length Measurements, Gradient Characterization, and Printing

To experimentally investigate transition behavior, single filament silicone lines, where material is switched from core (blue) to shell (clear) and vice-versa, is printed and analyzed with optical microscopy. It is worth noting that utilization of the C-S nozzle allows three different filament compositions to be printed consisting of complete shell material (S), complete core material (C), or core-shell (C-S) architected filament. However, only the transition from complete core to complete shell (C to S) and vice-versa (S to C) is currently studied, as it provides definitive differentiation between the two materials. In **Figure 4.2**, transition lines for the 1.6-mm and 1-mm nozzle are shown, where the beginning of the filament represents the point at which pump flow of material was switched. Three distinct regions **Figure 4.2a** within the filament can be seen: 1) an initial region consisting of the previous material being evacuated from the nozzle, 2) a graded transition region where materials switch, and 3) a region only displayed in C to S switching, where a small core region remains over an extended length, attributed to the remaining core material being drawn out as shell material is extruded around it.

Following the approach in **Figure 4.2a**, lengths of the three regions were experimentally measured, allowing for comparison to TL_{est} values. Calculated values are reported in **Table 4.1**. By plotting experimentally measured values versus estimated values in **Figure 4.3**, it is seen that TL_{est} values correlate well with the length required to clear previous material, L_{mc} as compared to the total transition length, TL_{tot} , the sum of L_{mc} and the length of the graded transition zone L_{gt} . Slight variation can be seen but is attributed to error when manually calculating nozzle volume. Nozzle geometry also has an impact on the transition behavior, indicated by differences in L_{gt} .

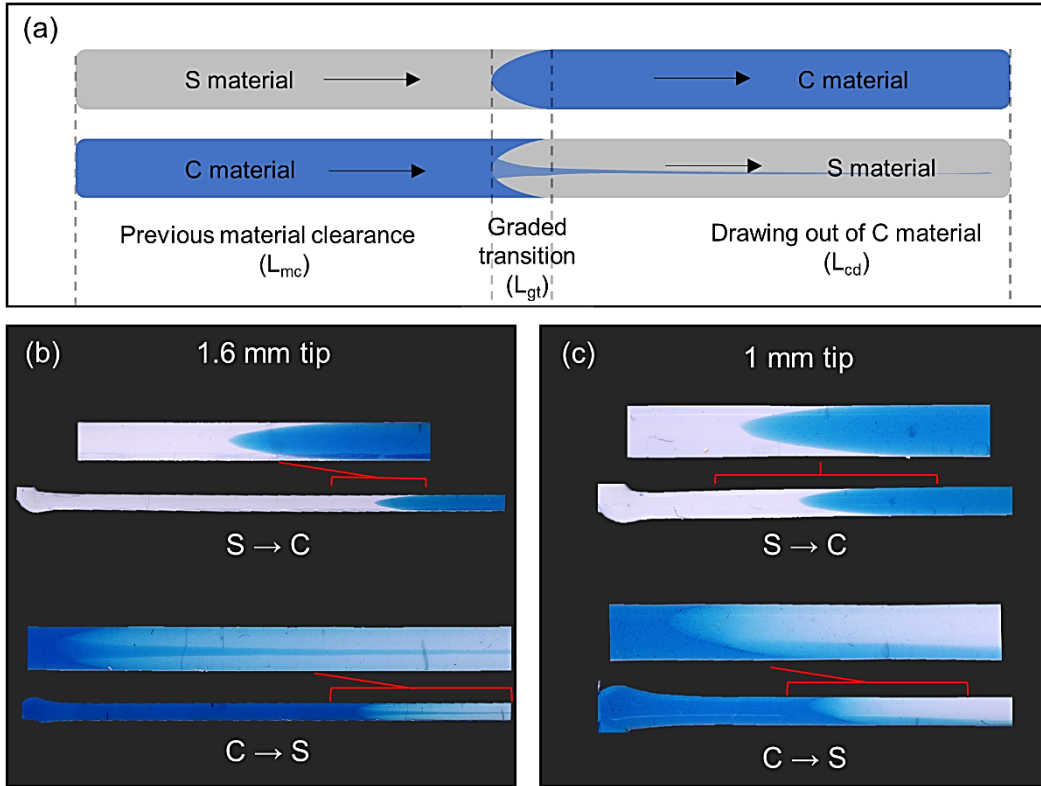


Figure 4.2. Silicone transition behavior. a) Schematic view of transition behavior showing three characteristic regions and lengths. Printed single filaments for transition length measurements in the b) 1.6 mm plastic tapered and c) 1 mm metal tapered tips. Note filaments diameter matches nozzle tip diameter.

Table 4.1. Experimentally measured values for characteristic transitional lengths.

Tip diameter (mm)	Nozzle type	Nozzle volume (mm ³)	TL _{est} (mm)	L _{mc} (mm)	L _{gt} (mm)	TL _{tot} (mm)	L _{cd} (mm)
1.6	Plastic tapered	51	27	29	6	35	45
1.2	Plastic tapered	46	41	47	10	57	60
1	Metal tapered	12	7	7	3	9	11

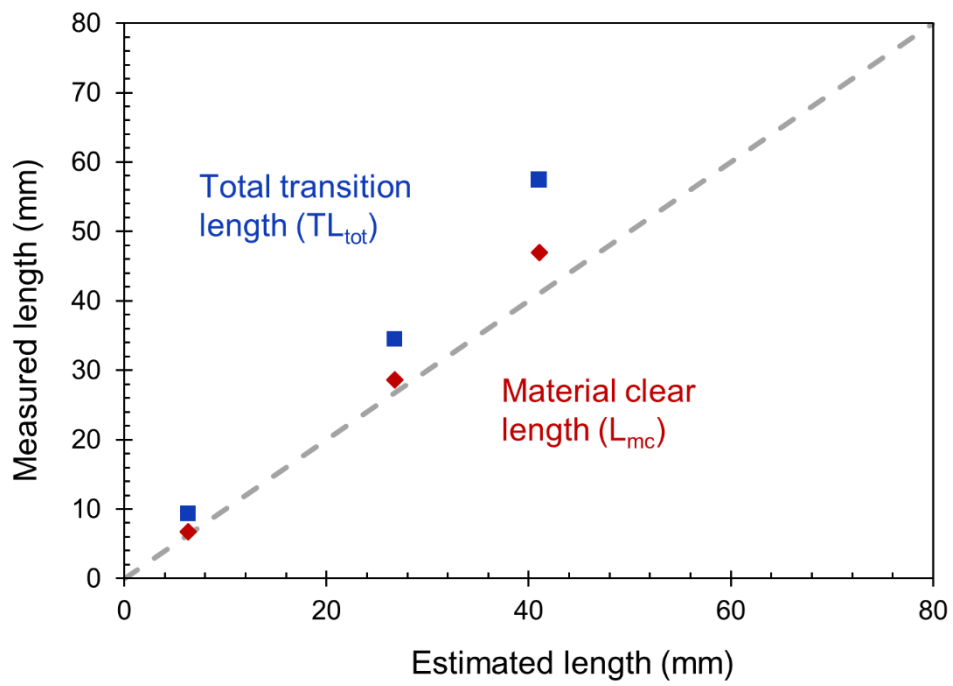


Figure 4.3. Experimentally measured transition lengths versus estimated lengths.

For plastic tapered tips, which have a more gradual taper and greater lengths, L_{gt} is short in relation to L_{mc} , presenting as ~20% the value of L_{mc} . In contrast, the metal tip exhibits a sharper taper and shorter length, displaying L_{gt} values 40% of the measured L_{mc} . Additionally, when moving from C to S, lengths of the core draw zone, L_{cd} , are roughly equal to the length of TL_{tot} . These relationships are advantageous to print path design and determination of material switching points, providing a route to easily calculate characteristic transition lengths from nozzle volumes and estimated values.

To demonstrate printing of two materials out of one nozzle, simple T-joints were printed with the 1-mm-diameter GPD tip, as it provided the shortest TL_{tot} . Printing was achieved with a continuous print path across the joint as seen in **Figure 4.4a**, where X's represent the point at which pump flow was switched. To achieve ideal switching, pumps must turn off and on instantaneously and simultaneously with each other in conjunction with printhead movement. In practical application however, hardware challenges exist such as signal lag between CNC and pump controllers, limitations in pump accuracy, and stoppage and starting time required to initiate and cease pump rotor rotation. To account for these, printhead movement was paused (0.1s) when pump switching occurred. Excessive pause time, likely caused by CNC controller imprecision, produced an over extrusion of material, forming bulges in filaments seen in **Figure 4.4b**. Further demonstrating compositional control, samples were printed where C material was carried across the joint **Figure 4.4c** and transitioned at the joint **Figure 4.4d**. This ability to control filament composition and properties within a part by defining of the print path can provide new possibilities to create improved functional and structural components.

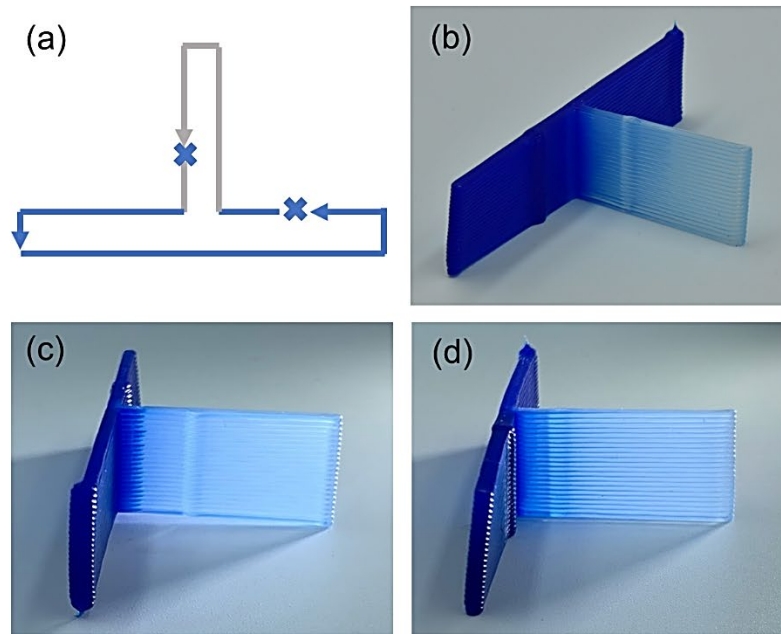


Figure 4.4. Printed silicone T-joint (60x35x15 H mm). a) Continuous print path to fabricate samples. b) Bulges can be seen where over extrusion occurred due to printhead pause. T-joint samples displaying material transition c) directly past and d) at the joint.

4.4.3 Multimaterial Printing with Carbon Fiber and Syntactic Foam Inks

To investigate application of core-shell multimaterial printing with filler loaded inks, transition lines were printed with CF shell and foam core inks. As samples are not translucent, filament cross-sections provide insight into transition behavior (**Figure 4.5**). Single filaments were sectioned at lengths of 5,10,15, and 20 mm, corresponding to the measured L_{mc} , TL_{tot} , and L_{cd} values from previous silicone prints. Loaded material transition displays similar general behavior (**Figure 4.2a**) as non-loaded silicone. At 5 mm, prior to gradient transition, filaments consist completely of material that is being cleared. At 10 mm ($\sim TL_{tot}$), material has neared final transition, exhibiting a composition with ~ 80 vol.% of the switched final material. At 20 mm, near the end of the estimated L_{cd} , material has predominantly switched over, with remnant 1-5 vol.% of previous material still present. Introduction of fillers does produce varied effects. When moving from S to C, after bulk transition, remanent fibers cling to the nozzle wall and are slowly drawn out as foam ink flows out, with minimal fibers still being present a substantial length after transition ($5-10x TL_{tot}$). When switching from C to S, the extended core drawn region is still present, with minimal core being observed up to 30 mm. A noteworthy feature exists in which the gradient transition region creates a core-shell motif within the filament, which could prove beneficial depending on the application. Pristine switching of material is challenging with fillers, especially high aspect ratio fillers (CF) that cling to surfaces and each other and could limit application where mixing or contamination is detrimental.

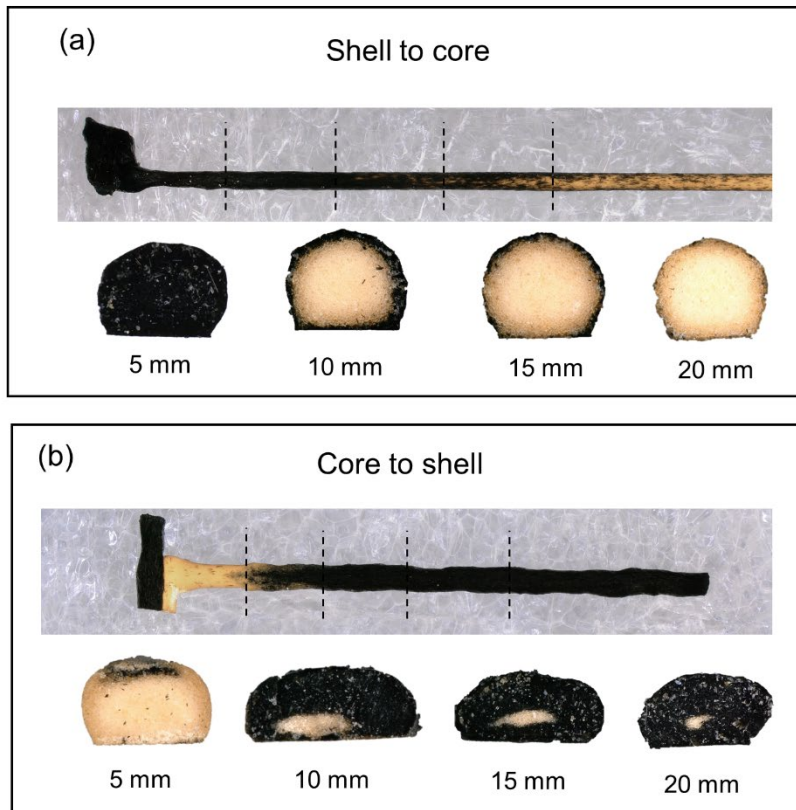


Figure 4.5. Cross-sectional analysis of transition behavior with CF and foam inks. Sections were taken at 5, 10, 15, and 20 mm. a) Shell (CF) to core (foam) and b) core to shell transition.

Mechanical performance of C-S printed multimaterials was investigated by printing 3-pt bend samples with the C-S nozzle (M-C/S) and via the two nozzle (2N) method (**Figure 4.6**), where material transition was prescribed to occur at the sample midpoint ($1/2 L$). Inherent to printing with multiple nozzles, gaps commonly occur at the material interface from the abrupt reverse/change in direction of the print head. Although printing with a continuous filament can alleviate this, samples were machined on all faces to ensure failure was not significantly affected by print defects induced by two nozzles. Initially, material transition in the C-S samples appeared incomplete, however, after machining removed a portion of the outer layer with remnant CFs, a definitive transition can be seen. Density measurements on as-printed samples revealed similar densities of 1.05 g/cc, matching the theoretical density for 50/50 CF/foam.

Flexural failure occurred at the transition line in C-S samples, however, 2N samples exhibited two failure locations; one where fracture occurred entirely in the foam (2N-F) and another occurring at the material interface (2N-I). It is worth noting the load point (fixture pin) was placed at the sample mid-point, directly above the transition line in all samples. 2N sample measurements clustered into two populations, with lower strengths (59 MPa) corresponding to failure in the foam and higher strengths (84 MPa) corresponding to failure at the interface. The increase in properties is attributed to the foam resisting failure away from the load point, allowing a portion of the CF material to contribute to load bearing. Sample misalignment in the test fixture or defects introduced during machining are possible causes of 2N-F failure location. M-C/S samples displayed a 60% increase in stiffness (12.3 GPa) and 16% increase in strength (97 MPa) over 2N-I samples. Investigation into the fracture surfaces (**Figure 4.6**), reveals aligned fibers,

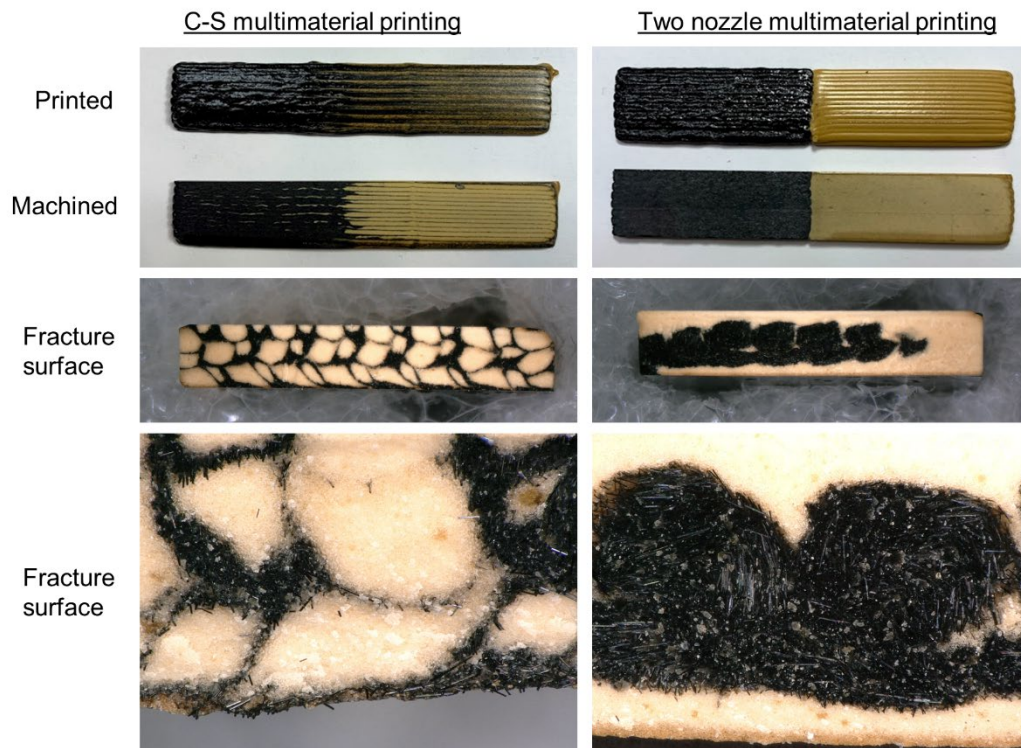


Figure 4.6. Multimaterial CF/foam flexural samples. Left, samples printed with the C-S nozzle and right, samples printed utilizing the conventional two nozzle approach.

induced by the continuous print path in M-C/S samples, and presence of fiber pull-out. In contrast, fibers are randomly aligned in 2N-I samples, as fracture occurs in a region where print path is reversed. With the ability to maintain a continuous print path yet still switch materials, components can be designed to not only benefit from a combination of two materials but also more effectively utilize reinforcement fillers such as CFs in those materials.

4.4.4 Mechanical Improvement and Design Analysis of Graded Transition

To provide guidance in the design of printed C-S multimaterial transitions, a mechanics analysis is conducted to rationalize the enhancement in flexural strength provided by a graded transition. As mentioned in the previous section, increased flexural strength can be attributed to aligned CFs enabled by a continuous print path; however, the following analysis will only focus on the contribution of the graded architecture itself to increased strength. Construction of free body diagrams for beams under bending, with a span length of L , with a sharp interface (**Figure 4.7a**), printed with two nozzles, and a graded transition interface (**Figure 4.7 b**), printed with the C-S nozzle, with a concentrated load (P) at the center, describes the bending moments (M) experienced during flexure where $M = PL/4$. An initial assumption is made that failure is caused by bending and not by shearing. This is supported by qualitative observations made during testing that failure initiates on the tension side and propagates upward through the sample. The flexural stress, σ , is given by the flexure formula:

$$\sigma = \frac{My}{I} \quad (4.4)$$

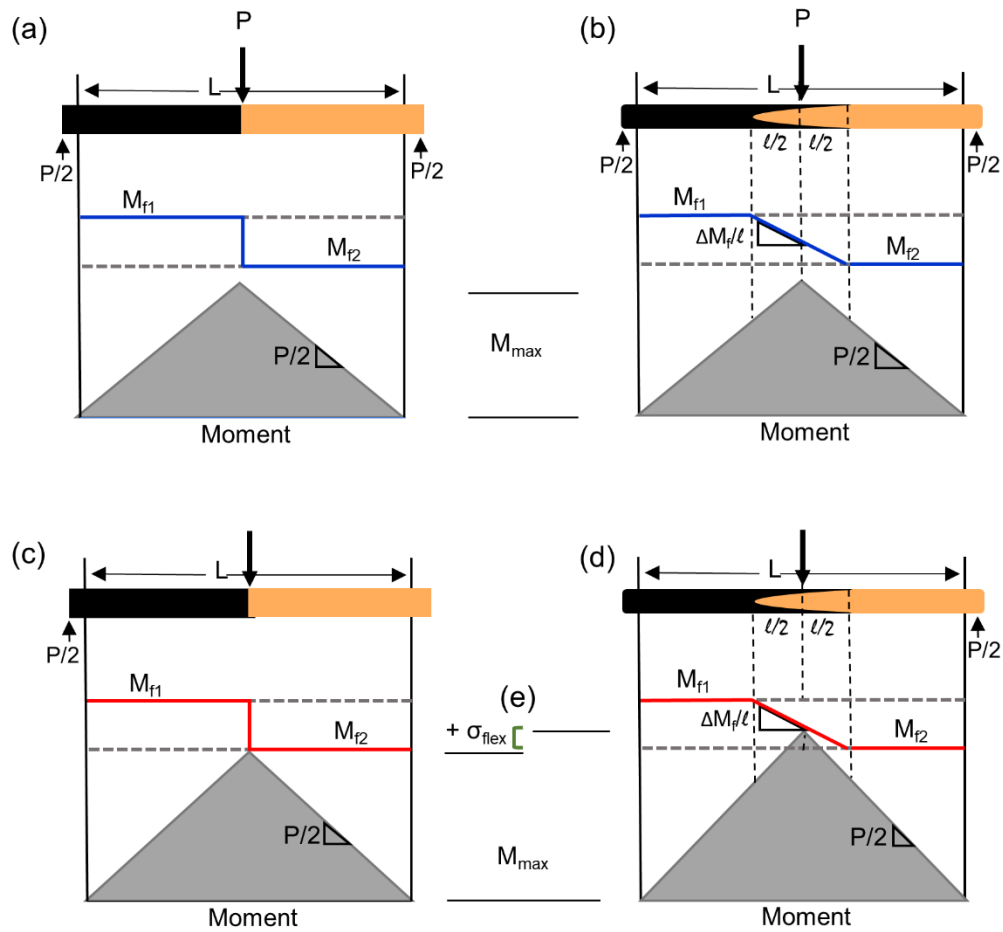


Figure 4.7. Schematics of multimaterial beams in bending. Presence of graded transition between materials produces an increase in flexural strength.

where I is the second moment of area of a rectangle given by:

$$I = \frac{bh^3}{12} \quad (4.5)$$

where h is the thickness of the beam and y is the distance from the neutral axis. The maximum stress occurs at either surface of the beam, $y = h/2$. Plugging in y and I gives a failure strength, σ_f , of:

$$\sigma_f = \frac{6M}{bh^2} \quad (4.6)$$

Rearrangement produces the equation for the bending moment required to cause failure

M_f :

$$M_f = \frac{bh^2 \sigma_f}{6} \quad (4.7)$$

M_f differs with material, denoted by M_{f1} for the higher strength CF composite and M_{f2} for the lower strength foam. A sharp interface will produce a corresponding discrete drop in M_f at the interface. Thus, as load is increased (**Figure 4.7c**), M_{max} increases until it eclipses M_{f2} of the foam and failure occurs. In contrast, a graded transition (**Figure 4.7b**) with length l produces a graded change in M_f , with slope $\Delta M_f/l$. As load is increased, M_{max} reaches a value greater than M_{f2} (**Figure 4.7d**) but does not fail until M_{max} eclipses the composite M_f value in the transition region. This results in an increase in M_{max} in graded transition samples and an increased flexural strength (**Figure 4.7e**).

For optimized design, it can be seen that maximum strength is achieved when:

$$\frac{\Delta M_f}{l} < \frac{P}{2} \quad (4.8)$$

If $\Delta M_f/l$ increases above $P/2$, it moves toward resembling a sharp interface, and M_{max} will eclipse M_f at a lower load, leading to decreased flexural strength. P can be eliminated

from equation 4.8 by utilizing the relationship $M=PL/4$ and then taking M to be the average of M_{f1} and M_{f2} . After rearrangement, the following optimized relationships are produced:

$$\frac{l}{L} \geq \frac{M_{f1} - M_{f2}}{M_{f1} + M_{f2}} \quad (4.9)$$

and

$$\frac{l}{L} \geq \frac{\sigma_{f1} - \sigma_{f2}}{\sigma_{f1} + \sigma_{f2}} \quad (4.10)$$

where l is the length of the graded transition and L is the span length. These relationships provide useful guidance when designing an appropriate transition length and component geometry to achieve optimal strength.

4.5 Conclusions

In summary, we have expanded the capabilities of C-S printing by developing a route to fabricate multimaterial components utilizing the previously developed C-S nozzle. Our route affords the ability to transition between materials, control filament composition, and maintain a continuous filament path, all while printing filled epoxy inks out of one nozzle. The C-S approach can be leveraged to further expand multimaterial AM, enabling fabrication of new hybrid structures with enhanced properties. A summary of findings is listed below:

- The length of material transition is directly related to nozzle volume and geometry and can be accurately estimated by simple nozzle volume calculations.

- Successful printing of a multimaterial T-joint, where continuous print path was maintained across the joint, was demonstrated. Further compositional control was displayed by varying the location of material transition within the sample.
- Filled epoxy inks display similar characteristic transition behavior, allowing transition lengths to be determined from nozzle volume calculations and geometry relationships.
- Multimaterial flexural samples printed with the C-S nozzle displayed increased properties at the location of load, compared to samples printed with two separate nozzles, attributed to aligned fibers enabled by a continuous print path.

5. FUTURE WORK

In this work, the development, capabilities, and benefits of core-shell DIW printing have been demonstrated. C-S printing is still in its infancy, with numerous advances and applications yet to be made and studied. Thus, future study into C-S printing displays promise, warranting continued study. Core-shell architected filaments are advantageous for weight sensitive applications such as cellular structures. Initial investigation was conducted by printing triangular honeycomb structures for compression testing but results were indecisive, exhibiting minimal benefit of C-S samples over monolithic CF. The absence of improvement was attributed to noticeable waviness of the cell walls from stacking faults (**Figure 5.1a**) between filaments in each layer. Thus, an increase in C-S properties over monolithic samples is expected if print quality can be improved. To do so, further study into optimized print parameters, mainly shell nozzle type, layer spacing and filament spacing, and print speed is warranted. Additionally, layer spacing will determine the degree of filament deformation upon deposition, potentially altering the C-S structure and properties, and consequently is worth further investigation. CF-reinforced and syntactic foam inks were the only filler loaded feedstock materials for C-S printing reported in this work. However, one of the advantages of the C-S nozzle is its ability to print epoxy filled inks with a variety of fillers. Structures consisting of a syntactic foam core/SiC whisker-reinforced shell have been successfully printed, demonstrating this versatility (**Figure 5.1b**). Feedstock inks have already been formulated to enable printing of metals, ceramics, and numerous composites, providing a vast selection of materials that could be utilized. Thus, the door is wide open for study into implementation of different material systems that will broaden the application space of C-S printing and advance material extrusion AM as a whole.

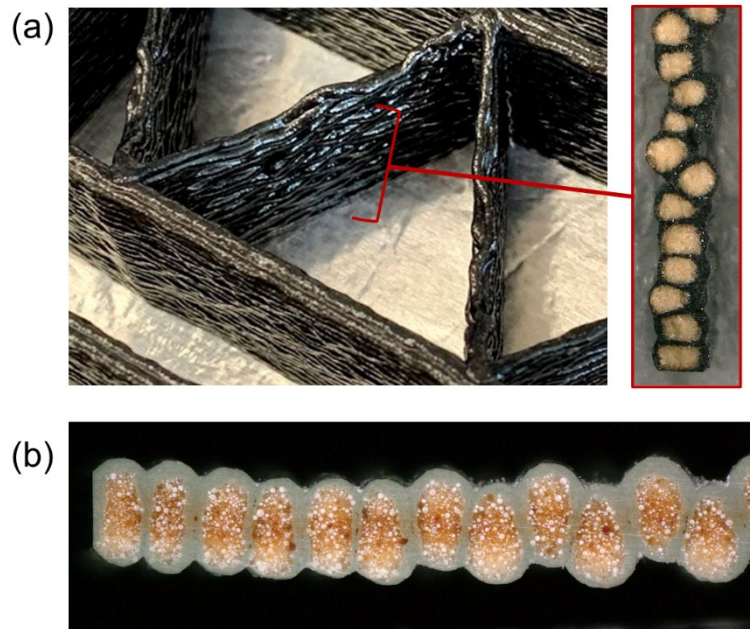


Figure 5.1. Carbon fiber and silicon carbide shelled C-S structures. a) CF- foam triangular honeycombs exhibited stacking faults and wall bowing in single walls. b) SiC C-S single wall demonstrating ability to print with various filled epoxy inks.

6. CONCLUSION

The motivation and goal of this work was to develop a novel core-shell printing approach to achieve improved properties, specifically increased stiffness at low densities. Initially, a novel core-shell nozzle was designed and printing process developed, to enabled printing of architected filaments, consisting of a new syntactic foam ink surrounded by a stiff carbon fiber-reinforced shell. Core-shell architected samples displayed significant improvement, up to 25%, in specific properties over constituent materials. Additionally, a new mechanical model was presented to predict the performance improvement afforded by the C-S architecture while accounting for potential eccentricity of the core model was developed.

After initial success with C-S printing, a challenge arose in obtaining an optimal low-density foam. Previous foam printing resulted in a detrimental increase in density, resultant of GMB fracture during processing. The second study addressed this challenge by investigating the relationship between processing parameters and printed density. It was discovered that GMB failure predominantly occurs during passage through the volumetric pumps. Optimization of GMB loading and flowrate proved effective in lowering density however, switching to GMBs of smaller diameter and higher strength proved much more effective, enabling printing of foams near theoretical density (0.69 g/cc), 18% lower than previous foam. Utilizing the new GMBs, printed foams displayed up to 5x higher compressive strength and modulus values compared to foams produced through conventional routes, fused filament fabrication, and DIW printing. Implementing the new foam in the C-S architecture resulted in a 5% increase in specific stiffness over previous values.

To conclude the work, the capability of C-S printing was expanded by demonstrating multimaterial 3D printing using the core-shell nozzle. This approach enabled “on-the-fly” switching between materials during fabrication, without the need for two nozzles. Material transition behavior was investigated, enabling accurate estimating of transition length. CF and foam multimaterial samples were successfully fabricated with a continuous print path, which exhibited increased stiffness and strength, demonstrating the design flexibility and compositional control afforded by C-S printing.

REFERENCES

1. Tofail, S.A.M., et al., *Additive manufacturing: scientific and technological challenges, market uptake and opportunities*. *Materials Today*, 2018. **21**(1): p. 22-37.
2. Singh, S., S. Ramakrishna, and R. Singh, *Material issues in additive manufacturing: A review*. *Journal of Manufacturing Processes*, 2017. **25**: p. 185-200.
3. Babu, S.S., *Scripta Viewpoint Set: Materials science aspects related to additive manufacturing*. *Scripta Materialia*, 2017. **135**: p. 97-99.
4. Brans, K., *3D Printing, a Maturing Technology*. *IFAC Proceedings Volumes*, 2013. **46**(7): p. 468-472.
5. Stansbury, J.W. and M.J. Idacavage, *3D printing with polymers: Challenges among expanding options and opportunities*. *Dental Materials*, 2016. **32**(1): p. 54-64.
6. Fleck, N.A., V.S. Deshpande, and M.F. Ashby, *Micro-architected materials: past, present and future*. *Proceedings of the Royal Society A: Mathematical, Physical and Engineering Sciences*, 2010. **466**(2121): p. 2495-2516.
7. Ajinjeru, C., et al., *Rheological survey of carbon fiber-reinforced high-temperature thermoplastics for big area additive manufacturing tooling applications*. *Journal of Thermoplastic Composite Materials*.
8. Duty, C., et al., *What makes a material printable? A viscoelastic model for extrusion-based 3D printing of polymers*. *Journal of Manufacturing Processes*, 2018. **35**: p. 526-537.

9. Duty, C., et al., *Z-Pinning approach for 3D printing mechanically isotropic materials*. Additive Manufacturing, 2019. **27**: p. 175-184.
10. Hmeidat, N.S., J.W. Kemp, and B.G. Compton, *High-strength epoxy nanocomposites for 3D printing*. Composites Science and Technology, 2018. **160**: p. 9-20.
11. Compton, B.G., et al., *Electrical and Mechanical Properties of 3D-Printed Graphene-Reinforced Epoxy*. JOM, 2018. **70**(3): p. 292-297.
12. Malek, S., et al., *Lightweight 3D cellular composites inspired by balsa*. Bioinspiration & Biomimetics, 2017. **12**(2): p. 026014.
13. Cai, K., et al., *Geometrically Complex Silicon Carbide Structures Fabricated by Robocasting*. Journal of the American Ceramic Society, 2012. **95**(8): p. 2660-2666.
14. Michna, S., W. Wu, and J.A. Lewis, *Concentrated hydroxyapatite inks for direct-write assembly of 3-D periodic scaffolds*. Biomaterials, 2005. **26**(28): p. 5632-5639.
15. Kemp, J.W., N.S. Hmeidat, and B.G. Compton, *Boron nitride-reinforced polysilazane-derived ceramic composites via direct-ink writing*. Journal of the American Ceramic Society, 2020. **103**(8): p. 4043-4050.
16. Yetna N'Jock, M., et al., *Characterization of 100Cr6 lattice structures produced by robocasting*. Materials & Design, 2017. **121**: p. 345-354.
17. Ahn, B.Y., et al., *Printed Origami Structures*. Advanced Materials, 2010. **22**(20): p. 2251-2254.

18. Jakus, A.E., et al., *Metallic Architectures from 3D-Printed Powder-Based Liquid Inks*. *Advanced Functional Materials*, 2015. **25**(45): p. 6985-6995.
19. Compton, B.G. and J.A. Lewis, *3D-Printing of Lightweight Cellular Composites*. *Advanced Materials*, 2014. **26**(34): p. 5930-5935.
20. Collino, R.R., et al., *Deposition of ordered two-phase materials using microfluidic print nozzles with acoustic focusing*. *Extreme Mechanics Letters*, 2016. **8**: p. 96-106.
21. Xia, Y.L., et al., *Microstructure and mechanical property of Cf/SiC core/shell composite fabricated by direct ink writing*. *Scripta Materialia*, 2019. **165**: p. 84-88.
22. Malek, S., et al., *Lightweight 3D cellular composites inspired by balsa*. *Bioinspiration & Biomimetics*, 2017. **12**(2).
23. Pierson, H.A., et al., *Mechanical Properties of Printed Epoxy-Carbon Fiber Composites*. *Experimental Mechanics*, 2019. **59**(6): p. 843-857.
24. Gladysz, G.M., et al., *Three-phase syntactic foams: structure-property relationships*. *Journal of Materials Science*, 2006. **41**(13): p. 4085-4092.
25. Bharath Kumar, B.R., et al., *Processing of cenosphere/HDPE syntactic foams using an industrial scale polymer injection molding machine*. *Materials & Design*, 2016. **92**: p. 414-423.
26. Gladysz, G.M. and K.K. Chawla, *Composite Foams*, in *Encyclopedia of Polymer Science and Technology*. 2004.
27. Gupta, N., et al., *Applications of Polymer Matrix Syntactic Foams*. *JOM*, 2014. **66**(2): p. 245-254.

28. Li, D., J.T. McCann, and Y. Xia, *Use of Electrospinning to Directly Fabricate Hollow Nanofibers with Functionalized Inner and Outer Surfaces*. *Small*, 2005. **1**(1): p. 83-86.
29. Sun, Z., et al., *Compound Core–Shell Polymer Nanofibers by Co-Electrospinning*. *Advanced Materials*, 2003. **15**(22): p. 1929-1932.
30. Yoon, J., et al., *Recent progress in coaxial electrospinning: New parameters, various structures, and wide applications*. *Advanced Materials*, 2018. **30**(42): p. 1704765.
31. Akkineni, A.R., et al., *A versatile method for combining different biopolymers in a core/shell fashion by 3D plotting to achieve mechanically robust constructs*. *Biofabrication*, 2016. **8**(4).
32. Milojević, M., et al., *Core/shell Printing Scaffolds For Tissue Engineering Of Tubular Structures*. *JoVE*, 2019(151): p. e59951.
33. Perez, R.A. and H.-W. Kim, *Core–shell designed scaffolds for drug delivery and tissue engineering*. *Acta Biomaterialia*, 2015. **21**: p. 2-19.
34. Moon, Y.-W., et al., *Macroporous alumina scaffolds consisting of highly microporous hollow filaments using three-dimensional ceramic/camphene-based co-extrusion*. *Journal of the European Ceramic Society*, 2015. **35**(16): p. 4623-4627.
35. Fu, Z.W., et al., *Robocasting of carbon-alumina core-shell composites using co-extrusion*. *Rapid Prototyping Journal*, 2017. **23**(2): p. 423-433.

36. Muth, J.T., et al., *Architected cellular ceramics with tailored stiffness via direct foam writing*. Proceedings of the National Academy of Sciences of the United States of America, 2017. **114**(8): p. 1832-1837.
37. Lorang, D.J., et al., *Photocurable Liquid Core-Fugitive Shell Printing of Optical Waveguides*. Advanced Materials, 2011. **23**(43): p. 5055-5058.
38. Mueller, J., et al., *Architected Lattices with High Stiffness and Toughness via Multicore–Shell 3D Printing*. Advanced Materials: p. n/a-n/a.
39. Dawson, M.A. and L.J. Gibson, *Optimization of cylindrical shells with compliant cores*. International Journal of Solids and Structures, 2007. **44**(3): p. 1145-1160.
40. Ashby, M.F., *Chapter 11 - Designing Hybrid Materials*, in *Materials Selection in Mechanical Design (Fourth Edition)*, M.F. Ashby, Editor. 2011, Butterworth-Heinemann: Oxford. p. 299-340.
41. Pack, R.C., et al., *Carbon Fiber and Syntactic Foam Hybrid Materials via Core–Shell Material Extrusion Additive Manufacturing*. Advanced Materials Technologies, 2020. **n/a**(n/a): p. 2000731.
42. Wegst, U.G.K., et al., *Bioinspired structural materials*. Nature Materials, 2014. **14**: p. 23.
43. Gibson, L.J., et al., *THE MECHANICAL-PROPERTIES OF NATURAL MATERIALS .2. MICROSTRUCTURES FOR MECHANICAL EFFICIENCY*. Proceedings of the Royal Society-Mathematical and Physical Sciences, 1995. **450**(1938): p. 141-162.
44. Karam, G.N. and L.J. Gibson, *BIOMIMICKING OF ANIMAL QUILLS AND PLANT STEMS - NATURAL CYLINDRICAL-SHELLS WITH FOAM CORES*.

- Materials Science & Engineering C-Biomimetic Materials Sensors and Systems, 1994. **2**(1-2): p. 113-132.
45. Chou, S.F. and R.A. Overfelt, *Tensile deformation and failure of North American porcupine quills*. Materials Science & Engineering C-Materials for Biological Applications, 2011. **31**(8): p. 1729-1736.
46. Torres, F.G., et al., *Failure analysis of porcupine quills under axial compression reveals their mechanical response during buckling*. Journal of the Mechanical Behavior of Biomedical Materials, 2014. **39**: p. 111-118.
47. Lewis, J.A., *Direct ink writing of 3D functional materials*. Advanced Functional Materials, 2006. **16**(17): p. 2193-2204.
48. Compton, B.G., et al., *Direct-write 3D printing of NdFeB bonded magnets*. Materials and Manufacturing Processes, 2018. **33**(1): p. 109-113.
49. Hmeidat, N.S., et al., *Mechanical anisotropy in polymer composites produced by material extrusion additive manufacturing*. Additive Manufacturing, 2020. **34**: p. 101385.
50. Lewicki, J.P., et al., *3D-Printing of Meso-structurally Ordered Carbon Fiber/Polymer Composites with Unprecedented Orthotropic Physical Properties*. Scientific Reports, 2017. **7**: p. 1-14.
51. Mueller, J., et al., *Architected Lattices with High Stiffness and Toughness via Multicore-Shell 3D Printing*. Advanced Materials, 2018. **30**(12): p. 1705001.
52. Wehmeyer, S.C., et al., *Damping in cellular structures made from composite struts and walls with elastic and viscoelastic phases*. Journal of the Mechanics and Physics of Solids, 2020. **In press**.

53. Schneider, C.A., W.S. Rasband, and K.W. Eliceiri, *NIH Image to ImageJ: 25 years of image analysis*. Nature methods, 2012. **9**(7): p. 671-675.
54. Pierson, H., et al., *Mechanical Properties of Printed Epoxy-Carbon Fiber Composites*. Experimental Mechanics, 2019: p. 1-15.
55. Raney, J.R., et al., *Rotational 3D printing of damage-tolerant composites with programmable mechanics*. Proceedings of the National Academy of Sciences, 2018. **115**(6): p. 1198-1203.
56. Nawafleh, N. and E. Celik, *Additive manufacturing of short fiber reinforced thermoset composites with unprecedented mechanical performance*. Additive Manufacturing, 2020. **33**: p. 101109.
57. Han, C.D., *STUDY OF COEXTRUSION IN A CIRCULAR DIE*. Journal of Applied Polymer Science, 1975. **19**(7): p. 1875-1883.
58. Minagawa, N. and J.L. White, *CO-EXTRUSION OF UNFILLED AND TIO2-FILLED POLYETHYLENE - INFLUENCE OF VISCOSITY AND DIE CROSS-SECTION ON INTERFACE SHAPE*. Polymer Engineering and Science, 1975. **15**(12): p. 825-830.
59. Vlachopoulos, J. and D. Strutt. *The role of rheology in polymer extrusion*. in *New Technology for Extrusion Conference*. 2003.
60. Gupta, N. and E. Woldesenbet, *Microballoon Wall Thickness Effects on Properties of Syntactic Foams*. Journal of Cellular Plastics, 2004. **40**(6): p. 461-480.

61. Farkash, M. and D.G. Brandon, *WHISKER ALIGNMENT BY SLIP EXTRUSION*. Materials Science and Engineering a-Structural Materials Properties Microstructure and Processing, 1994. **177**(1-2): p. 269-275.
62. Bell, J.P., *Flow Orientation of Short Fiber Composites*. Journal of Composite Materials, 1969. **3**(2): p. 244-253.
63. Murty, K.N. and G.F. Modlen, *EXPERIMENTAL CHARACTERIZATION OF ALIGNMENT OF SHORT FIBERS DURING FLOW*. Polymer Engineering and Science, 1977. **17**(12): p. 848-853.
64. Ashby, M.F., *Chapter 5 - Materials Selection—The Basics*, in *Materials Selection in Mechanical Design (Fourth Edition)*, M.F. Ashby, Editor. 2011, Butterworth-Heinemann: Oxford. p. 97-124.
65. Parnes, R., *Symmetric bending of beams- basic relations and stresses*, in *Solid Mechanics in Engineering*. 2001, Wiley and Sons.
66. Barbosa, S.E. and J.M. Kenny, *Processing of short-fiber reinforced polypropylene. I. Influence of processing conditions on the morphology of extruded filaments*. Polymer Engineering & Science, 2000. **40**(1): p. 11-22.
67. Duty, C.E., et al., *Structure and mechanical behavior of Big Area Additive Manufacturing (BAAM) materials*. Rapid Prototyping Journal, 2017.
68. Heller, B.P., D.E. Smith, and D.A. Jack, *Planar deposition flow modeling of fiber filled composites in large area additive manufacturing*. Additive Manufacturing, 2019. **25**: p. 227-238.

69. Kang, T., et al., *Structure of 3D-printed Acrylonitrile Butadiene Styrene (ABS)/Carbon Fiber Composite Investigated by Small-Angle Neutron Scattering*. Polymer Composites, 2017. **In Review**.
70. Heller, B.P., D.E. Smith, and D.A. Jack, *Effects of extrudate swell and nozzle geometry on fiber orientation in Fused Filament Fabrication nozzle flow*. Additive Manufacturing, 2016. **12**: p. 252-264.
71. Gupta, N., E. Woldesenbet, and Kishore, *Compressive fracture features of syntactic foams-microscopic examination*. Journal of Materials Science, 2002. **37**(15): p. 3199-3209.
72. Jayavardhan, M.L., et al., *Development of glass microballoon/HDPE syntactic foams by compression molding*. Composites Part B: Engineering, 2017. **130**: p. 119-131.
73. Gladysz, G.M. and K.K. Chawla, *Preface - Syntactic and composite foams: Proceedings of an Engineering Conferences International (ECI) conference*. Journal of Materials Science, 2006. **41**(13): p. 3959-3960.
74. Gupta, N., E. Woldesenbet, and P. Mensah, *Compression properties of syntactic foams: effect of cenosphere radius ratio and specimen aspect ratio*. Composites Part A: Applied Science and Manufacturing, 2004. **35**(1): p. 103-111.
75. H S, B., et al., *Three-Dimensional Printed Lightweight Composite Foams*. ACS Omega, 2020.
76. Singh, A.K., et al., *Additive Manufacturing of Three-Phase Syntactic Foams Containing Glass Microballoons and Air Pores*. JOM, 2019. **71**(4): p. 1520-1527.

77. Patil, B., B.R. Bharath Kumar, and M. Doddamani, *Compressive behavior of fly ash based 3D printed syntactic foam composite*. *Materials Letters*, 2019. **254**: p. 246-249.
78. Singh, A.K., et al., *Additive Manufacturing of Syntactic Foams: Part 1: Development, Properties, and Recycling Potential of Filaments*. *JOM*, 2018. **70**(3): p. 303-309.
79. Singh, A.K., et al., *Additive Manufacturing of Syntactic Foams: Part 2: Specimen Printing and Mechanical Property Characterization*. *JOM*, 2018. **70**(3): p. 310-314.
80. Nawafleh, N., et al., *3D-printed thermoset syntactic foams with tailorable mechanical performance*. *Journal of Materials Science*, 2020. **55**(33): p. 16048-16057.
81. 3M Advanced Materials Division, *3M Glass Bubbles K Series, S Series, and iM Series*. 2013: St. Paul, MN.
82. 3M Advanced Materials Division, *3M Glass Bubbles Brochure*. 2018: St. Paul, MN.
83. 3M Advanced Materials Division, *3M Glass Bubbles S32HS*. 2018: St. Paul, MN.
84. 3M Advanced Materials Division, *3M Glass Bubbles Metering and Mixing Guide*. 2016: St. Paul, MN.
85. 3M Advanced Materials Division, *3M Glass Bubbles Compounding and Injection Molding Guidelines*. 2016: St. Paul, MN.
86. ViscoTec, *Preeflow Microdispensing Brochure*. 2019: Germany.

87. ViscoTec, *Print Heads for Viscous Fluids and Pastes in Additive Manufacturing*. 2019: Germany.
88. Romberg, S.K., et al., *Linking thermoset ink rheology to the stability of 3D-printed structures*. Additive Manufacturing, 2020: p. 101621.
89. Vlachopoulos, J. and N. Polychronopoulos, *Basic Concepts in Polymer Melt Rheology and Their Importance in Processing*, in *Applied Polymer Rheology*. 2011. p. 1-27.
90. Dinkgreve, M., et al., *On different ways of measuring “the” yield stress*. Journal of Non-Newtonian Fluid Mechanics, 2016. **238**.
91. Swanson, P., *The Endless Piston Pump Technology for Precision Dispensing*. 2007.
92. Coogan, T. and D. Kazmer, *In-line rheological monitoring of fused deposition modeling*. Journal of Rheology, 2019. **63**: p. 141-155.
93. Zhang, J. and M. Ashby, *The out-of-plane properties of honeycombs*. International journal of mechanical sciences, 1992. **34**(6): p. 475-489.
94. Gibson, L.J. and M.F. Ashby, *Cellular Solids: Structure and Properties*. 1997: Cambridge University Press.
95. Lewis, J.A. and G.M. Gratson, *Direct writing in three dimensions*. Materials Today, 2004. **7**(7): p. 32-39.
96. Pack, R.C. and B.G. Compton, *Material Extrusion Additive Manufacturing of Metal Powder-Based Inks Enabled by Carrageenan Rheology Modifier*. Advanced Engineering Materials, 2020.

97. Kolesky, D.B., et al., *3D Bioprinting of Vascularized, Heterogeneous Cell-Laden Tissue Constructs*. *Advanced Materials*, 2014. **26**(19): p. 3124-3130.
98. Hardin, J.O., et al., *Microfluidic Printheads for Multimaterial 3D Printing of Viscoelastic Inks*. *Advanced Materials*, 2015. **27**(21): p. 3279-3284.

APPENDIX

Eccentric Sandwich Composite Model

Ideal Flexural Modulus

Effective core-shell flexural modulus ($E_{f,eff}$) predictions are made using the Equation A1.1, which considers a single filament of the printed core-shell architecture.

$$E_{f,eff} = \frac{D_{cs}}{I_0} \quad (A1.1)$$

where D_{cs} is the bending stiffness (or flexural rigidity) of the core-shell architecture and I_0 is the second moment of area of the outer envelope of the C-S geometry. The effective density, ρ_{eff} , is also required to determine the material index.

$$\rho_{eff} = V_f \rho_c + (1 - V_f) \rho_s \quad (A1.2)$$

where V_f is the volume fraction of the core material, ρ_c is the density of the core material, and ρ_s is the density of the shell material. The various geometries and idealizations utilized in the analytical C-S model development are displayed in **Figure A1**. Two geometric idealizations are assumed to quantify D_{cs} , I_0 , and ρ_{eff} and generate two separate predictions. Two deposited shapes bound the potential behavior. First, a perfectly circular filament (denoted by subscript "c") is analyzed. This corresponds to a deposited filament which experiences no compression during deposition. Second, a rectangular bead is analyzed. This corresponds to a bead which is compressed to fill any voids between itself and its neighbors.

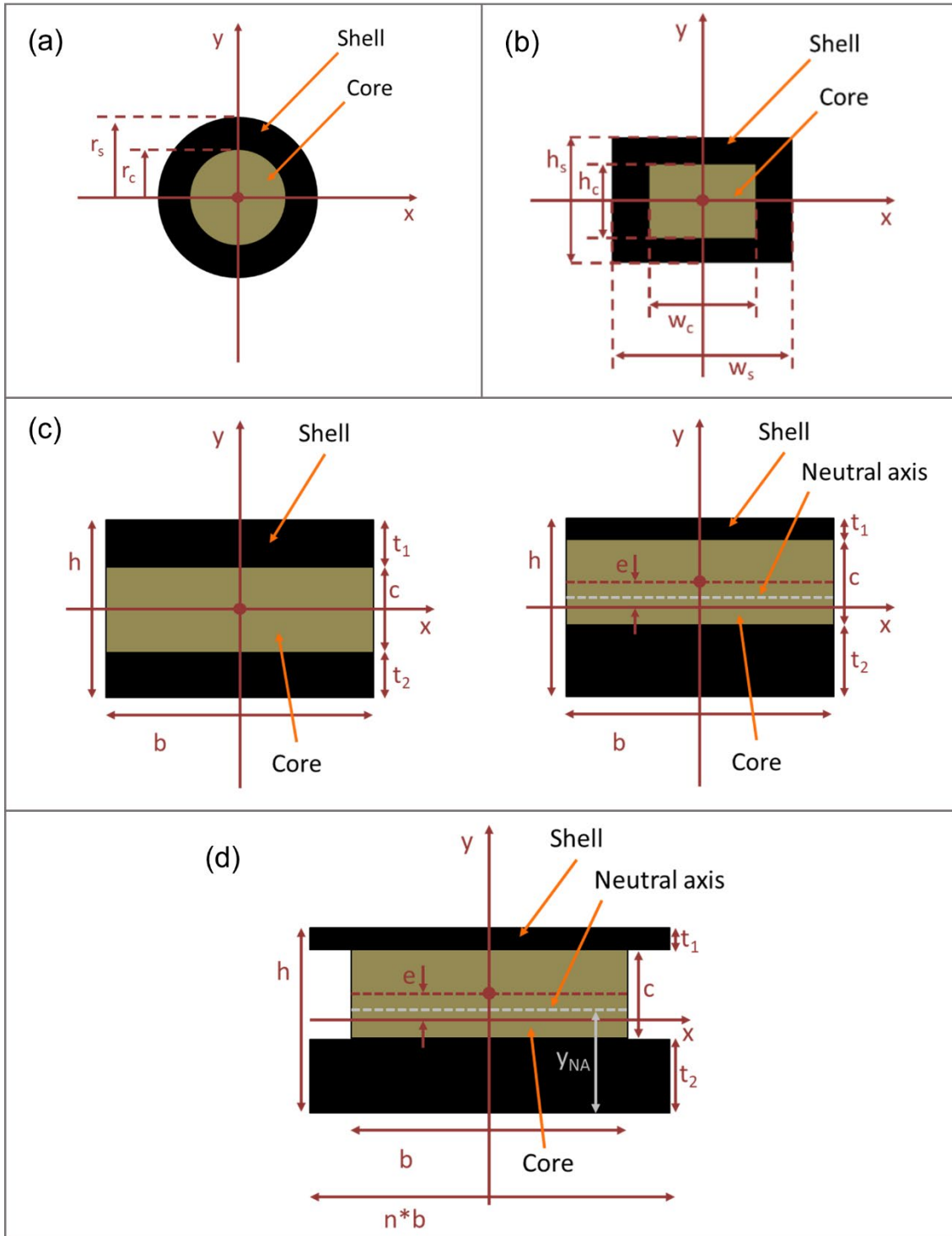


Figure A1. Geometries and idealizations for analytical C-S model development. a) Circular and b) rectangular filament geometry. c) Geometric idealization of the single layer C-S specimens showing concentricity (left) and eccentricity (right). d) Conceptual diagram used to determine the location of the neutral axis

Figure A1a shows the assumed circular geometry. $D_{cs,c}$ is calculated using Equation A1.3, which was presented by Gibson et al. [43].

$$D_{cs,c} = \frac{1}{2} \int_0^{r_s} E(r) 2\pi r^3 dr \quad (\text{A1.3})$$

where r_s is the outer radius of the shell and $E(r)$ is the radially-dependent elastic modulus. Although the X-ray CT micrograph in Figure 3e shows some GMBs migrating into the shell and some CFs drifting into the core, the transition between foam and CF composite material appears fairly distinct. Therefore, throughout the following derivation we assume that the material instantaneously shifts from foam to CF composite at the interface between the core and the shell, and we assume a perfect bond between core and shell regions. Consequently, this equation splits into two simple integrals for the geometry shown in **Figure A1a**.

$$D_{cs,c} = \frac{1}{2} \int_0^{r_c} E_c 2\pi r^3 dr + \frac{1}{2} \int_{r_c}^{r_s} E_s 2\pi r^3 dr \quad (\text{A1.4})$$

where E_c is the elastic modulus of the core, r_c is the outer radius of the core, and E_s is the elastic modulus of the shell. Assuming E_c and E_s are homogenous (i.e. not dependent upon r), the bending stiffness equation simplifies to:

$$\begin{aligned} D_{cs,c} &= E_c \pi \int_0^{r_c} r^3 dr + E_s \pi \int_{r_c}^{r_s} r^3 dr = E_c \pi \frac{r_c^4}{4} + E_s \pi \left(\frac{r_s^4}{4} - \frac{r_c^4}{4} \right) \\ &= E_c I_{c,c} + E_s I_{s,c} \end{aligned} \quad (\text{A1.5})$$

where $I_{c,c}$ is the second moment of area of the circular core and $I_{s,c}$ is the second moment of area of the circular shell. The second moment of area provided by the outer envelope of the C-S geometry is:

$$I_{0,c} = \pi \frac{r_s^4}{4} \quad (\text{A1.6})$$

Dividing $D_{cs,c}$ by $I_{0,c}$ gives

$$E_{f,eff,c} = E_s + (E_c - E_s) \frac{r_c^4}{r_s^4} \quad (\text{A1.7})$$

Volume fraction is calculated by dividing the cross-sectional area of the core by the cross-sectional area of the entire filament.

$$V_{f,c} = \frac{\pi r_c^2}{\pi r_s^2} = \frac{r_c^2}{r_s^2} \quad (\text{A1.8})$$

Substituting using the volume fraction relation, the effective flexural modulus simplifies to:

$$E_{f,eff,c} = E_s + (E_c - E_s) V_{f,c}^2 \quad (\text{A1.9})$$

To calculate the material index over the range of possible volume fractions, only material properties require assignment of values. No geometric values are required. The properties (E_c , ρ_c , E_s , and ρ_s) from the monolithic trials with the 1.2-mm nozzle provide comparison between experimental results and analytical predictions. **Figure A1b** shows the assumed rectangular geometry. As in the case of the circular filament, this model assumes the material instantaneously shifts from foam to CF composite at the interface

between the core and the shell and there is a perfect bond between the two regions. The equation for $D_{cs,r}$ is shown below.

$$D_{cs,r} = E_c I_{c,r} + E_s I_{s,r} = E_c \frac{w_c h_c^3}{12} + E_s \left(\frac{w_s h_s^3}{12} - \frac{w_c h_c^3}{12} \right) \quad (\text{A1.10})$$

where $I_{c,r}$ is the second moment of area of the rectangular core, $I_{s,r}$ is the second moment of area of the rectangular shell, w_c is the width of the core, h_c is the height of the core, w_s is the width of the shell, and h_s is the height of the shell. w_c and w_s are both idealized as functions of h_c and h_s , respectively.

$$w_c = C_1 h_c \quad (\text{A1.11})$$

$$w_s = C_1 h_s \quad (\text{A1.12})$$

where C_1 is a constant describing the ratio of measured width to measured height. This constant is idealized to be identical for the core and the shell, because both regions of the filament are expected to compress in approximately the same proportion upon deposition. The second moment of area provided by the outer envelope of the C-S geometry is

$$I_{0,r} = \frac{w_s h_s^3}{12} \quad (\text{A1.13})$$

Dividing $D_{cs,r}$ by $I_{0,r}$ simplifies to

$$E_{f,eff,r} = E_s + (E_c - E_s) \frac{w_c h_c^3}{w_s h_s^3} = E_s + (E_c - E_s) \left(\frac{h_c}{h_s} \right)^4 \quad (\text{A1.14})$$

The volume fraction is calculated by dividing the cross-sectional area of the core by the cross-sectional area of the entire filament, resulting in

$$V_{f,r} = \frac{w_c h_c}{w_s h_s} = \left(\frac{h_c}{h_s} \right)^2 \quad (\text{A1.15})$$

Substituting using the volume fraction relation, the effective flexural modulus simplifies to:

$$E_{f,eff,r} = E_s + (E_c - E_s)V_{f,r}^2 \quad (\text{A1.16})$$

The equation for the rectangular effective flexural modulus (A1.9) collapses to the same equation as in the circular case (A1.16). Again, to numerically calculate the material index, values must be assigned to several parameters. The material properties are assigned in the same way as the circular case.

Correction for Eccentricity

Cross-sectional micrographs of the three-point bend specimens show notable eccentricity. To predict the effects of off-center foam placement, a simple conceptual model is proposed. Although the shell separates adjacent foam cores, as shown in Figure 2e, this model assumes that the foam cores are not separated and the entire bend specimen acts as a sandwich panel that could exhibit eccentricity as shown in **Figure A1c**. The definition of volume fraction for a sandwich panel differs from that shown before, as described below.

$$V_f = \frac{c}{h} \quad (\text{A1.17})$$

Eccentricity, e , is defined as the distance from the center of the core to the geometric center of the sandwich. The following equation uses the Parallel Axis Theorem to predict the flexural rigidity, D , of eccentric sandwich panels.

$$D = E_s(I_{t_1,local} + I_{t_2,local} + I_{t_1,global} + I_{t_2,global}) + E_c(I_{c,local} + I_{c,global}) \quad (A1.18)$$

where I refers to the second moment of area, the subscript t_1 refers to the top faceplate, the subscript t_2 refers to the bottom faceplate, the subscript c refers to the core, the subscript “*local*” refers to the second moment of area of the given shape with respect to its own center, and the subscript “*global*” refers to the second moment of area with respect to the neutral axis of the entire geometry.

$$I_{local} = \frac{bl_y^3}{12} \quad (A1.19)$$

where b is the width of the constituent geometry and l_y is the thickness of the constituent geometry in the y-direction.

$$I_{global} = bl_y * d_{NA}^2 \quad (A1.20)$$

where d_{NA} is the distance between the neutral axis and the centroid of the constituent geometry. The neutral axis moves away from the geometrical center of the sandwich as the eccentricity increases. To determine the location of the neutral axis for composite beams in bending, Parnes [65] lays out a method to account for differences in material stiffness by changing the dimensions of the constituent materials such that uniform stiffness throughout the beam can be assumed. This approach is applied in the following derivation to define the neutral axis. A ratio, $n = \frac{E_s}{E_c}$, is used to increase the area of the

shell with respect to the core as shown in **Figure A1d**. The following equation determines the location of the neutral axis from the bottom of the panel.

$$y_{NA} = \frac{(nbt_1)\left(h - \frac{t_1}{2}\right) + (bc)\left(t_2 + \frac{c}{2}\right) + (nbt_2)\left(\frac{t_2}{2}\right)}{(nbt_1) + (bc) + (nbt_2)} \quad (\text{A1.21})$$

where

$$t_1 = \frac{h - c}{2} - e \quad (\text{A1.22})$$

$$t_2 = \frac{h - c}{2} + e \quad (\text{A1.23})$$

With this information, d_{NA} for each constituent can be determined.

$$d_{NA,t_1} = h - \frac{t_1}{2} - y_{NA} \quad (\text{A1.24})$$

$$d_{NA,t_2} = y_{NA} - \frac{t_2}{2} \quad (\text{A1.25})$$

$$d_{NA,c} = t_2 + \frac{c}{2} - y_{NA} \quad (\text{A1.26})$$

And finally, all I values can be determined

$$I_{t_1,local} = \frac{bt_1^3}{12} \quad (\text{A1.27})$$

$$I_{t_2,local} = \frac{bt_2^3}{12} \quad (\text{A1.28})$$

$$I_{c,local} = \frac{bc^3}{12} \quad (\text{A1.29})$$

$$I_{t_1,global} = bt_1 d_{NA,t_1}^2 \quad (\text{A1.30})$$

$$I_{t_2,global} = bt_2 d_{NA,t_2}^2 \quad (\text{A1.31})$$

$$I_{c,global} = bcd_{NA,c}^2 \quad (A1.32)$$

Plugging A1.27-A1.32 into A1.18, predictions can be made for the resultant flexural rigidity with any magnitude of eccentricity. Normalizing these equations will help to make this analysis more generally applicable. If D is normalized by $D(e = 0)$, a “knockdown factor,” α , is formed which allows for correction of eccentric cores simply by multiplying the ideal modulus by the corresponding knockdown factor.

$$\alpha \equiv \frac{D}{D(e = 0)} \quad (A1.33)$$

Normalizing e by its maximum value, $e = \frac{(h-c)}{2}$, we can generalize the knockdown factor for different geometries.

$$\bar{e} = \frac{2e}{h - c} \quad (A1.34)$$

This substitution leads to the following expression for the knockdown factor.

$$\alpha = \frac{E_c^2 V_f^4 + E_s^2 (V_f - 1)^2 (V_f^2 + V_f - 3V_f \bar{e}^2 + 1)}{[E_s + V_f(E_c - E_s)][E_s + V_f^3(E_c - E_s)]} - \frac{E_c E_s V_f (V_f - 1) (2V_f^2 + V_f - 3\bar{e}^2 V_f + 3\bar{e}^2 + 1)}{[E_s + V_f(E_c - E_s)][E_s + V_f^3(E_c - E_s)]} \quad (A1.35)$$

Thus, the effective flexural modulus of a core-shell architecture with some level of eccentricity is:

$$E_{f,eff} = \alpha [E_s + (E_c - E_s) V_f^2] \quad (Eq. 2.1)$$

which corresponds to Equation 2.1 in the main text.

Pressure-driven Flow Model for Foam Inks

Table A3.1. Pressure-driven flow model predictions versus experimental SSP values.

Foam	Calculated Model Properties	Flowrate ($\mu\text{L}/\text{min}$)						
		200	400	600	800	1000	1200	1400
S32-45	Shear rate (1/s)	87	173	260	346	433	519	606
	Pressure (MPa)	0.23	0.26	0.27	0.29	0.30	0.31	0.31
S32-50	Shear rate (1/s)	111	221	332	443	553	664	775
	Pressure (MPa)	0.18	0.19	0.20	0.21	0.21	0.22	0.22
S32-58	Shear rate (1/s)	195	389	584	778	973	1168	1362
	Pressure (MPa)	0.10	0.10	0.11	0.11	0.11	0.11	0.11
S32HS-58	Shear rate (1/s)	144	287	431	574	718	861	1005
	Pressure (MPa)	0.31	0.33	0.34	0.35	0.35	0.36	0.36

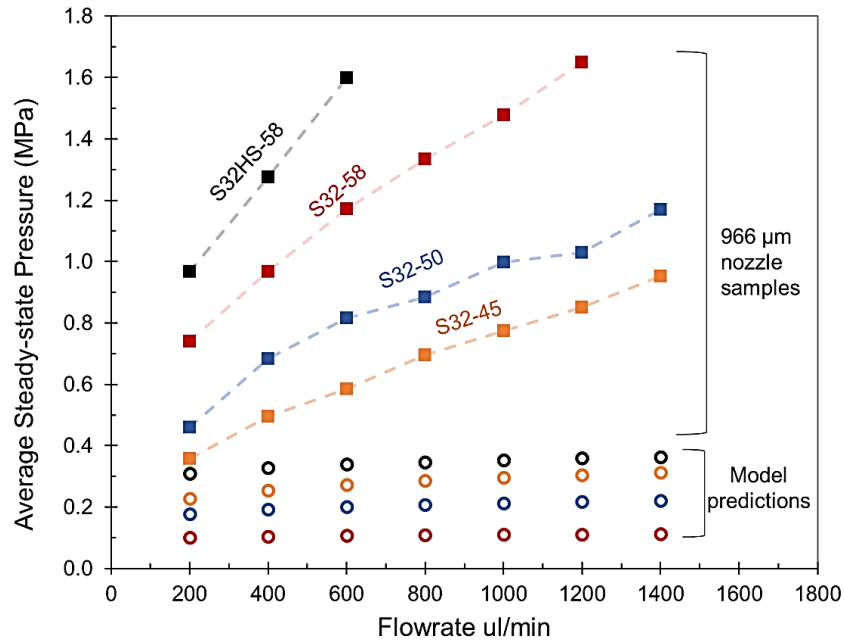


Figure A3.1. Pressure-driven flow model predictions and experimental SSP values.

VITA

Robert Cody Pack is a native of East Tennessee, where he was born and raised. Robert obtained his Bachelor of Science degree in Chemistry from Lincoln Memorial University in 2011. Upon completion of undergraduate studies, he worked at Oak Ridge National Laboratory under Rick Lowden, performing work in the areas of metal matrix composites and critical/strategic materials. To further his education, Robert began his graduate work in 2012, joining Dr. Claudia Rawn's group at the University of Tennessee, Knoxville, in the Materials Science and Engineering Department. Robert earned his Master of Science degree in December 2014, after which he continued with pursuit of a PhD. He joined Dr. Brett Compton's group at UTK in 2016 to conduct research in the area of material extrusion additive manufacturing, specifically direct ink writing. Robert's main research focus has been on the formulation of feedstock inks and development of new printing hardware/routes for DIW.